Assessing the Accuracy of Cosmological Parameters Estimated from Velocity – Density Comparisons

by

Amber Hollinger

A thesis
presented to the University of Waterloo
in fulfillment of the
thesis requirement for the degree of
Doctor of Philosophy
in
Physics

Waterloo, Ontario, Canada, 2023

© Amber Hollinger 2023

Examining Committee Membership

The following served on the Examining Committee for this thesis. The decision of the Examining Committee is by majority vote.

Supervisor: Michael Hudson
Professor, Dept. of Physics and Astronomy,
University of Waterloo

Committee Member: Will Percival
Professor, Dept. of Physics and Astronomy,
University of Waterloo

Committee Member: Niayesh Afshordi
Professor, Dept. of Physics and Astronomy,
University of Waterloo

Internal/External Member: Marek Stastna
Professor, Dept. of Applied Mathematics,
University of Waterloo

External Examiner: Dragan Huterer
Professor, Dept. of Physics,,
University of Michigan

Author's Declaration

This thesis consists of material all of which I authored or co-authored: see Statement of Contributions included in the thesis. This is a true copy of the thesis, including any required final revisions, as accepted by my examiners.

I understand that my thesis may be made electronically available to the public.

Statement of Contributions

This thesis is based on the following articles:

Chapter 3: **Hollinger A. M.** and Hudson M. J., 2021. Assessing the accuracy of cosmological parameters estimated from velocity – density comparisons via simulations. *Monthly Notices of the Royal Astronomical Society*, 502, 3723–3732. doi:10.1093/mnras/staa4039

Chapter 4: **Hollinger A. M.** and Hudson M. J., 2023. Cosmological parameters estimated from velocity – density comparisons: Calibrating 2M++. *Monthly Notices of the Royal Astronomical Society*, submitted (MN-23-4073-MJ)

Chapter 5: Based on work currently in preparation for publication.

The research presented in this thesis was conducted under the guidance of Mike Hudson. The majority of the computational analysis presented in these chapters was performed by me. I was the primary author for all chapters in this work, but Mike Hudson provided valuable input for the manuscripts submitted to MNRAS and Chapter 5 of this thesis. The analysis and interpretation of Section 4.7.1 was primarily performed by Mike Hudson using data I generated, but has been left in this thesis for completeness. He provided direction as well as helpful suggestions with respect to to the analysis and interpretation of our manuscripts.

Abstract

A promising method for measuring the cosmological parameter combination $f\sigma_8$ is to compare observed peculiar velocities with peculiar velocities predicted from a galaxy density field using linear perturbation theory, known as velocity-velocity (velocity-density) comparisons. We use N-body simulations and semi-analytic models of galaxy formation to quantify the accuracy and precision of this method. Specifically, we examine a number of technical aspects, including the optimal smoothing length applied to the density field, the use of dark matter halos or galaxies as tracers of the density field, the effect of noise in the halo mass estimates or in the stellar-to-halo mass relation, and the effect of finite survey volumes. We find that for a Gaussian smoothing of $4h^{-1}$ Mpc, the method has only small systematic biases at the level of 5%. We estimate that cosmic variance affects current measurements at the 5% level due to the volume of current redshift data sets.

Previous work has tested the accuracy of velocity-density comparisons with N-body simulations, but generally on idealised mock galaxy surveys. However, systematic biases may arise solely due to survey selection effects such as flux-limited samples, edge-effects and complications due to the obscuration of the Galactic plane. In this thesis, we explore the impact of each of these effects independently and simultaneously, using the semi-analytic models from numerical simulations to generate mock catalogues that mimic the 2M++ density field. We find the reconstruction and analysis methods used for our 2M++ mocks produce a value of $f\sigma_8$ that is biased high by a factor 1.04 ± 0.01 compared to the true value. Moreover, a cosmic volume matching that of 2M++ has a cosmic variance uncertainty in $f\sigma_8$ of $\sim 5\%$. The systematic bias is a function of distance: it is unbiased close to the origin but is biased slightly high for distances in the range 100–180 h^{-1}Mpc. Correcting for this small bias, we find $f\sigma_8^{\rm lin} = 0.362 \pm 0.023$. The predicted peculiar velocities from 2M++ have an error of 170 km s^{-1} that slowly increases with distance, exceeding 200 km s^{-1} only at distances of 180-200 h^{-1}Mpc. Finally, the residual bulk flow speeds found in previous work are shown to be not in conflict with those expected in the ΛCDM model.

Using these results we investigate the impact reconstructing cosmological redshifts, using peculiar velocities, has on measurements of the Hubble constant (H_0). Recent measurements of H_0 using type Ia supernovae explicitly correct for their estimated peculiar velocities using the 2M++ reconstruction of the local density field. The amount of uncertainty that is generated due to this reconstruction has thus far been unquantified. To rectify this we use our mock Universe realisations of 2M++ catalogues and peculiar velocities, that are generated using the same method as the predictions that are used to correct for the Pantheon+ catalogue. We find that the method is able to reproduce measurements to within ~ 0.3 km s^{-1} Mpc^{-1} and hence is subdominant to the total uncertainty in H_0.

Acknowledgements

I would like to express my sincere gratitude and appreciation to several individuals who have contributed significantly to the completion of this thesis.

First and foremost, I am deeply thankful for the guidance, support, and patience of my supervisor, Mike Hudson. Your expertise in the field has been invaluable throughout this journey. Your insightful feedback and constructive criticism have greatly shaped the direction of this work.

Furthermore, I am grateful for all those who provided assistance during challenging times and for letting me complain endlessly about my coding struggles. Last but certainly not least, I want to acknowledge my friends, old and new, who have supported me throughout my academic journey and helped keep me sane - your encouragement meant more than words can express.

To all those mentioned above: Thank you.

This work was supported financially partially through the Ontario graduate scholarship program and the University of Waterloo, as well as additional funding support through the NSERC Discovery grant of Mike Hudson.

This thesis was dependent on the computing resources of Digital Research Alliance of Canada[1].

The N-Body simulation and semi-analytic model data underlying this thesis are publicly available from the `COSMOSIM` database [2]. The Patheon+ supernovae data used in Chapter 5 is available at https://github.com/PantheonPlusSH0ES/DataRelease.

---

[1] https://ccdb.alliancecan.ca

[2] https://www.cosmosim.org/

Dedication

This thesis is dedicated to my mom. Thank you for your endless support.

Table of Contents

List of Figures

List of Tables

List of Abbreviations

ΛCDM Λ-Cold Dark Matter

2MASS Two Micron All-Sky Survey

2MRS 2MASS Redshift Survey

2MTF 2MASS Tully-Fisher Survey

6dFGRSv 6dFGRS Peculiar Velocity Catalogue

6dFGS 6-degree Field Galaxy Survey

6dFGSz 6dFGS Redshift Catalogue

A1 First Amendment Supernovae Catalogue

A2 Second Amendment Supernovae Catalogue

BAO Baryon Acoustic Oscillation

CF Cosmicflow

CMB Cosmic Microwave Background

DES Dark Energy Survey

DESI Dark Energy Spectroscopic Instrument

DR Data Release

eBOSS Extended Baryon Oscillation Spectroscopic Survey

FLRW Friedmann-Lemaitre-Robertson-Walker

FP Fundamental Plane

GR General Relativity

GW Gravitational Waves

KiDS Kilo-Degree Survey

LSS Large-Scale Structure

MCMC Markov chain Monte Carlo

MDPL2 MultiDark Planck 2

MW Milky-Way.

PSCz Point Source Catalogue Redshift Survey

SAM Semi-Analytic Model

SBF Surface Brightness Fluctuations

SDSS Sloan Digital Sky Survey

SH0ES Supernova H_0 for the Equation of State

SHMR Stellar-to-Halo Mass Relation

SNe Supernovae

SNe Ia Type Ia Supernovae

TF Tulley-Fisher

TRGB Tip of the Red Giant Branch

ZoA Zone of Avoidance

Chapter 1

Introduction

Cosmology is the study of the nature and origin of the Universe, including its structure, matter, energy, and fate. It has been a topic of scientific inquiry for thousands of years, and there have been many significant discoveries and developments in our understanding of the cosmos. Different civilisations worldwide developed myths and stories to explain the origins of the Universe and the workings of the natural world. Ancient astronomers were fascinated by the motions of celestial objects and sought to understand their workings. They observed that stars, planets, and other celestial bodies appeared to move across the sky in predictable patterns and understanding the motions of the Universe continues to fascinate cosmologists to this day. Notable early astronomers include Ptolemy, who lived in Alexandria around 150 AD. Ptolemy developed a geocentric model of the Universe; wherein Earth is stationary while all other celestial bodies revolve around us in complex circular orbits. This classical view was overturned in the 16th century by Renaissance philosopher and astronomer Copernicus who proposed a heliocentric model in which Earth and other planets instead orbit around a stationary Sun. This marked a significant shift from previous geocentric models and the beginning of the scientific revolution and the emergence of modern cosmology. Later advancements came during the 17th century in the form of Kepler's laws of planetary motion and the publication of "Principia Mathematica" by Newton (1687) describing his law of universal gravitation. These breakthroughs provided mathematical descriptions for understanding how objects moved within our Solar System.

Of course these early astronomers did not have access to modern technology or knowledge about galaxies or cosmology beyond our own Solar System. Their observations primarily focused on studying planetary motion within our immediate cosmic neighbourhood. It was only in the early decades of the 20th century that our understanding of the Universe and the motion of objects within drastically shifted.

1.1 Modern Cosmology and Peculiar Velocities

The foundations of modern cosmology were laid out by Einstein (1916) in the form of his theory of General Relativity (GR). This theory provided a mathematical description of gravity and allowed for solutions that described an expanding or contracting universe. Initially, Einstein (1918) introduced an ad-hoc constant called the Cosmological Constant Λ to maintain a static universe. However, the groundbreaking discovery by Hubble (1929) that galaxies are moving away from each other at speeds proportional to their distances, led to the abandonment of this static universe concept. This led to the formulation of Hubble's Law and provided strong evidence for an expanding universe, see Section 1.5 for more details. The Friedmann-Lemaître-Robertson-Walker (FLRW) model, discussed in Section 1.2.1, became prominent as a result. This model is based on solutions of GR that incorporate an expanding universe, following the cosmological principles of homogeneity and isotropy. It quickly gained acceptance as a standard framework for cosmology.

The development of the Big Bang Theory was a collaborative effort by many in the field of cosmology, which proposes that our Universe originated from an extremely hot and dense state about 13.8 billion years ago. Some key contributors to this theory include Lemaître (1931), who first proposed the idea of an expanding universe and suggested a "primeval atom" from which it originated. Hubble (1929), who provided observational evidence for the expansion of the Universe through his observations of galaxies moving away from each other. As well as Alpher et al. (1948), who developed models that explained how elements were formed in the early stages after the Big Bang. The discovery of Cosmic Microwave Background (CMB) radiation by Penzias & Wilson (1965) further supported this theory as it provided strong evidence for an initial hot and dense state in our Universe's history. The discovery of the CMB was a significant milestone in confirming the standard cosmological model.

In the 1980s, the concept of cosmic inflation was introduced by the likes of Guth (1981), Albrecht & Steinhardt (1982) and Linde (1982). Inflation theory suggests that in the first fractions of a second after the Big Bang, a rapid expansion occurred, resulting in a flatness and smoothness to our Universe on large scales. This theory helped explain several observations such as uniformity of CMB temperature across different directions and the scale-invariant primordial density fluctuations required for structure formation. It also helped to explain several issues with the standard Big Bang model such as the horizon problem. Observations of different regions of our observable Universe, which are now far apart, appear to have similar properties. Without inflation, these regions should not have had enough time since the beginning of the Universe for light or information to travel between them and establish a common temperature or density. The exponential growth would have stretched out any initial irregularities in temperature or density across vast distances before slowing down into normal expansion. By smoothing out these irregularities on scales larger than what we can observe today, inflation provides an explanation for why distant parts of the observable Universe share similar properties despite being too far apart according to conventional understanding.

This exponential growth also stretched the tiny quantum fluctuations into larger density variations across different regions. These density variations eventually served as seeds for gravitational collapse that led to formation of structures like galaxies and galaxy clusters over billions of years. In this way, inflation provides an explanation for how small initial perturbations could grow into significant differences in matter distribution on cosmological scales seen today. It helps explain why we observe patterns such as CMB radiation temperature fluctuations or clustering properties among galaxies at such vast distances from each other.

Gravitational perturbations arising from the large-scale structure (LSS) of the Universe have important consequences, including peculiar velocities and the growth rate of structures, which will be discussed in detail in Section 2.1.1. Peculiar velocities refer to the motions of galaxies or other cosmic objects that deviate from their expected motion due to gravitational interactions with surrounding matter. These deviations are caused by density fluctuations in the LSS, which create variations in gravitational forces experienced by nearby objects. By studying these peculiar velocities, we are able to gain insights into how matter is distributed on large scales and its expected evolution over time.

The standard cosmological model has been extensively tested against various observational data sets, such as CMB measurements from satellites like Planck (Planck Collaboration et al., 2020b) and large-scale structure surveys such as the Sloan Digital Sky Survey (SDSS; York et al. (2000)) and the extended Baryon Oscillation Spectroscopic Survey (eBOSS; Dawson et al. (2016)). While it successfully explains many observed phenomena, it also poses several open questions, such as the nature of dark matter and dark energy. These questions continue to drive more advanced research and evidence-based modifications or extensions to the model in order to better understand our vast and complex Universe.

1.2 The Standard Cosmological Model

The standard cosmological model, also known as the ΛCDM model, is the prevailing framework used to describe the evolution and structure of our Universe. It can be derived directly by Einstein's Field Equations, under the assumption of the Cosmological Principal (which states that the Universe is homogeneous and isotropic on large scales), and with the additional contribution of the Cosmological Constant Λ. This theoretical model can be constrained by cosmological parameters that describe the energy content of the Universe, the majority of which is primarily attributed to dark energy (Λ) and cold dark matter (CDM). According to this model, the composition of the Universe can be attributed as follows: approximately 68% of our Universe consists of dark energy, driving the late stage accelerated expansion of the Universe. About 27% is composed of cold dark matter that clusters and drives the formation of large-scale structure and galaxy halos. Only the remaining 5% is then attributed to ordinary matter and radiation (Planck Collaboration et al., 2020b).

However, there are still some questions that remain unresolved in this model, such as the true nature of both of these ‘dark’ components. Additionally while the presence of the Cosmological Constant provides an accurate description of the Universe’s accelerating expansion, it does not provide any details about what is behind the phenomenon. This model also incorporates inflationary theory and provides a predictive framework for understanding various aspects of the Universe’s evolution, such as formation of solar systems, growth of structures, and the distributions of galaxies. In this section, we will discuss the fundamental assumptions needed to describe the current standard model of cosmology.

1.2.1 Friedmann-Lemaître-Robertson-Walker Model

The FLRW model is a commonly used metric in Newtonian cosmology. It describes the expansion of space after the Big Bang and the motion of galaxies, clusters, and other cosmological structures in this expanding space. To describe the Universe’s LSS, we can adopt the Cosmological Principle, that the Universe to be uniform and symmetrical in all directions. More formally these conditions are known as homogeneity and isotropy; the former ensures that observers from different locations throughout the Universe perceive identical properties, while the latter means there are no preferred directions.

Building on this principle, we are now able to consider the case of an expanding universe. The space-time dynamics are captured by the Minkowski metric tensor,

$$ds^2 \equiv g_{\mu\nu} dx^\mu dx^\nu \,, \tag{1.1}$$

where $\mu, \nu = 0, 1, 2, 3$ and the metric tensor ($g_{\mu\nu}$) is used to describe the geometry of space-time. To add a component to account for expansion, we can write the Minkowski metric with an added expansion co-efficient as a function of time

$$ds^2 = c^2 dt^2 - a^2(t) dl^2 \,. \tag{1.2}$$

Table 1.1: Summary of curvature values, K, and their effect on the geometry of the Universe

Curvature	Geometry	Sum of a Triangles Angles	Universe Type
K>0	Spherical	>180	Closed
K=0	Flat / Euclidean	=180	Flat
K<0	Hyperbolic	<180	Open

Here t, l and s are respectively the line-elements of time, space and space-time components, c is the speed of light, and we have introduced the scale factor, $a(t)$, which represents the expansion of the Universe over time. Typically it is defined to be with respect to the scale factor's value at the present-day value (a_0) such that the scale factor is dimensionless $a(t) = a(t)/a_0$. This is the convention that is assumed in this thesis. In this way the scale factor starts at zero at the time of the Big Bang and increases to unity today.

To uphold isotropy, one can enforce spherical symmetry. In the framework of GR, we can also envision a more complex spatial geometry that results in non-flat three-dimensional hypersurfaces (such as hyperspheres or hyperbolae), which once we factor in the curvature slightly modifies the line element:

$$ds^2 = -c^2 dt^2 + a^2(t) \left[\frac{dr^2}{1 - Kr^2} + r^2 (d\theta^2 + \sin^2 \theta d\varphi^2) \right] , \tag{1.3}$$

where the spherical coordinates r, θ, φ are comoving. The specific curvature of space-time is determined by the parameter K, which can be scaled to take on one of three possible values $(0, \pm 1)$, with properties summarised in Table 1.1.

Which corresponds to the spatial hypersurfaces of the Universe exhibiting positive, zero, or negative curvature. In conclusion, we reach the metric that enables a solution with maximum symmetry to the Einstein equations for an expanding universe. This metric is commonly known as the FLRW (Friedmann-Lemaître-Robertson-Walker) metric, named after the scientists who made significant contributions in this area of research.

1.2.2 Dark Matter

The existence of dark matter is one of the most important mysteries in physics and astronomy. While it this mysterious substance is thought to be much more abundant than ordinary matter, its nature and properties are largely unknown. The term was originally coined by Zwicky (1933), to explain the measured velocity dispersion of the Coma cluster, which required much more mass than what was visible to explain observations. The idea of dark matter regained interest in the 1970s, when Rubin and collaborators (Rubin & Ford, 1970; Rubin et al., 1978; Rubin et al., 1980; Rubin, 1983; Rubin et al., 1985) as well as Bosma (1978) determined the mass inside the galaxies was much higher than could be accounted for from its luminous components. They found that the rotation speeds of the outskirts of spiral galaxies were unexpectedly high, again suggesting the need for an invisible component, such as dark matter, to explain the observations. Since then, evidence for the existence of dark matter has continued to accumulate, but remains one of the greatest mysteries in physics and astronomy today.

We now believe dark matter makes up around 85% of the total matter in the Universe, but little is known about its nature. Based on observations and theory, it appears that dark matter is non-baryonic and does not interact via the electromagnetic force. Additionally, it is thought to be cold, which in this case means it moves at relatively low (non-relativistic) speeds. Dark matter is often considered to be collisionless, in that it neither interacts with itself nor other forms of matter. However, the gravitational effects of dark matter on visible matter have provided strong evidence of its existence. The mass of dark matter in galaxies and clusters is enough to warp the path of light and distort the appearance of distant galaxies. A more extensive discussion of the properties and likely particle candidates for dark matter can be found in a comprehensive review by Feng (2010). This review provides a wealth of information and context for understanding one of the most profound mysteries in physics and astronomy.

1.2.3 Dark Energy

The Universe's accelerated expansion is one of modern cosmology's most significant results and was first reported by Perlmutter et al. (1998) and Riess et al. (1998), and evidence supporting this result is still being found to this day (Jones et al., 2019; Brout et al., 2022). To account for this observed acceleration with physical foundations, an unknown hypothetical entity (known as dark energy) responsible for driving this accelerated expansion was proposed, and can be incorporated into cosmological models simply by introducing a positive constant. The specific physical mechanism behind this acceleration is still not fully understood, although there are now numerous theoretical approaches that could potentially explain it. The component of the Universe responsible for this expansion must possess negative pressure, which cannot be achieved with ordinary matter. It is believed to be highly uniform and does not interact through any fundamental forces other than gravity.

However, simply incorporating this cosmological constant into our cosmological models poses challenges, such as explaining the current vacuum energy density (Ω_Λ) deduced from observations. Known as the cosmological constant problem, the vacuum energy density has been measured to be $\sim 10^{-48}$ GeV^4, this value is 60-120 orders of magnitude smaller than what theoretical expectations suggest. Thus implying that if Ω_Λ was even slightly larger, it would cause an excessively fast expansion of the Universe. This rapid expansion would prevent sufficient time for galaxies and other gravitationally bound systems to form. Additionally, there is a puzzling aspect known as the cosmic coincidence problem. It questions why the value of the cosmological constant is finely tuned in such a way that it dominates during a specific period in our present Universe, leading to observed accelerated expansion.

Due to the various problems associated with the cosmological constant (Weinberg, 1989), alternative approaches have been proposed to explain the late-time acceleration driven by dark energy, but lie outside the scope of this thesis. A review of some of the various method that have been proposed can be found in Yoo & Watanabe (2012).

1.3 Evolution of the Universe and the Friedmann Equations

Following the period of inflation, the expansion or contraction rate of the Universe is determined by its constituents, which include radiation, matter (both of dark and baryonic variety), and dark energy. Under the assumption that these components are perfect fluids which hence follow the equation of state parameterised in terms of the density as:

$$P = -w\rho c^2 \,, \tag{1.4}$$

where ρ refers to density, P signifies pressure, c the speed of light and the parameter $w = 0, -1/3, 1$ for CDM and baryonic matter, radiation, and dark energy respectively. The dynamic evolution of a ΛCDM universe is governed by the Friedmann equations: (Friedmann, 1922, 1924).

$$H^2 \equiv \left(\frac{\dot{a}}{a}\right)^2 = \frac{8\pi G}{3c^2}\rho \,, \tag{1.5}$$

$$\frac{\ddot{a}}{a} = -\frac{4\pi G}{3}\left(\rho + \frac{3P}{c^2}\right) \,. \tag{1.6}$$

In these equations, G is gravitational constant, $H(t)$ represents the Hubble parameter and $a(t)$ denotes the scale factor characterising the size of the Universe. Note that we have removed the explicit time dependence on these variables for ease of reading.

Through the definition of the critical density,

$$\rho_c \equiv \frac{3H}{8\pi G}\,, \tag{1.7}$$

the present day normalised density parameters are defined as

$$\Omega_x \equiv \frac{\rho_x}{\rho_c}\,, \tag{1.8}$$

where x represents the radiation (r), matter (m), and dark energy (Λ) components of the Universe. The curvature (K) of the Universe can be defined as

$$\Omega_K = 1 - \sum \Omega_x\,. \tag{1.9}$$

so that the sum of all Ω's is one.

The Hubble parameter introduced in Eqn. 1.5 is often expressed in the dimensionless form

$$E(z) = \frac{H(t)}{H_0} = \sqrt{\frac{\Omega_r}{a^4} + \frac{\Omega_m}{a^3} + \frac{\Omega_K}{a^2} + \Omega_\Lambda}\,, \tag{1.10}$$

where H_0 is the present day value of the Hubble parameter.

The Friedmann equations also allows for the definition of the deceleration parameter,

$$q_0 \equiv -\frac{a}{\dot{a}^2}\ddot{a}\,. \tag{1.11}$$

This can be used to describe the acceleration of the Universe, as it is related to the second derivative of the scale factor. If q_0 is positive, the Universe is undergoing decelerating expansion, while if negative the expansion is accelerating. If this value is 0 the Universe is undergoing uniform expansion. Assuming the Universe is flat, as is the assumption taken in this thesis, Eqn. 1.11 simplifies to:

$$q_0 = 0.5\Omega_m - \Omega_\Lambda\,. \tag{1.12}$$

The Planck Collaboration et al. (2020b) measurements of the density parameters for ΛCDM are: $\Omega_m = 0.315 \pm 0.007$, $\Omega_\Lambda = 0.6889 \pm 0.0056$, and $\Omega_K = 0.001 \pm 0.002$; indicating that the Universe is undergoing accelerating expansion as $\Omega_\Lambda > \Omega_m$, resulting in a negative expression in Eqn. 1.12.

Fundamental Cosmological Parameters

There are a dozen parameters that can be considered fundamental when describing the standard cosmological model. Currently, the determination of cosmological quantities is primarily driven by experiments measuring CMB anisotropies. The Planck satellite, supported by various other data sources, has played a significant role in providing results on CMB power spectra (Planck Collaboration et al., 2020b).

The basic parameter set used is defined in terms of quantities that are directly measured by CMB experiments, which results in six free parameters that describes a flat ΛCDM cosmology. This parameter set includes:

- $\Omega_b h^2$ and $\Omega_c h^2$: Respectively representing the baryonic and cold dark matter density, as they have distinct effects on CMB power spectra. A scaling factor involving physical density and Hubble parameter represented as $h \equiv H_0/100$ km s^{-1} Mpc^{-1}, see Section 1.5 for more details.
- Θ_*: Corresponding to the sound horizon scale divided by angular diameter distance at last scattering; which quantifies the degree to which the CMB power spectra is shifted left or right.
- A_s: The amplitude of the power spectrum for density perturbations at a particular scale (often given logarithmically).
- n_s: The slope of the power spectrum as a function of wavenumber.
- τ: The optical depth at reionization, which is a measure of the scattering/absorption of photons by free electrons during the process of cosmic reionization. This quantifies the degree to which CMB radiation is affected by interactions with ionized gas at low redshifts.

These parameters form an essential part within current discussions related to observational constraints but fall outside the scope of this thesis. A more in-depth discussion can be found in Scott (2006).

1.4 Distances in Cosmology

1.4.1 Redshifts

The relative movement of luminous objects in the Universe with respect to the Earth results in a compression or stretching of observed wavelengths, dependent on whether the object is moving towards or away from the observer. As the Universe is expanding the observed wavelength λ_o, observed at time t_o, is generally larger than that emitted (λ_e) at t_e, the fractional difference is the objects redshift can be defined as:

$$z \equiv \frac{\lambda_o - \lambda_e}{\lambda_e} = \frac{1}{a(t_e)} - 1\,, \tag{1.13}$$

where we have assumed that $a(t_o) = 1$. This quantity is known as the cosmological redshift $z_{\rm cosmo}$, which will be used in later chapters of this thesis.

1.4.2 Proper and Comoving Distances

Here we return briefly to the FLRW model of the Universe described in Section 1.2.1. If we consider that emitted photons travel along null geodesics (i.e. $ds = 0$), under the assumption of isotropy ($d\theta = d\varphi = 0$) the metric of Eqn. 1.3 simplifies to:

$$c^2 dt^2 = \frac{a^2(t) dr^2}{1 - Kr^2}\,. \tag{1.14}$$

By integrating the right hand-side of the equation, we can define the distance a photon could travel accounting for the Universe's expansion as the proper distance (D), thus providing a measure from the origin to a comoving particle at radial coordinate r at time t. These are the coordinates which are carried along with the expansion of the Universe, i.e.:

$$D = \int dD = a(t) \int_0^r \frac{dr'}{\sqrt{1 - Kr'^2}} = a(t)\chi(r)\,. \tag{1.15}$$

Where for simplicity, we have introduced the coordinate χ, which is the comoving distance between two observers. This is defined as:

$$\chi(r) = \begin{cases} \frac{1}{\sqrt{K}} \sin^{-1}\left(r\sqrt{K}\right) & \text{if } K > 0 \\ r & \text{if } K = 0 \\ \frac{1}{\sqrt{K}} \sinh^{-1}\left(r\sqrt{|K|}\right) & \text{if } K < 0 \end{cases}\,. \tag{1.16}$$

Typically, as one is unable to observe χ directly, it is far more convenient to use the redshift instead. Recalling that $1 + z = 1/a$ and hence $dz = -(da/a^2)$ as well as $H \equiv \dot{a}/a$, the comoving distance can be calculated as follows:

$$d\chi = \frac{cdt}{a} = \frac{cda}{a^2 H(a)} = \frac{cdz}{H(z)}\,. \tag{1.17}$$

Using the convention defined in Eqn. 1.10 yields:

$$\chi = \frac{c}{H_0} \int_0^z \frac{dz'}{E(z')}\,. \tag{1.18}$$

1.4.3 Luminosity Distance

One of the methods used to determine an object's distance in astrophysics is through the comparison of how bright the observed object is compared to the brightness it is expected to have. The brightness an object has, as observed on Earth, is known as the apparent magnitude (m). We define the brightness that object would have if it were to be observed at a distance of 10 parsecs from Earth as the absolute magnitude (M). The difference between these two magnitude is the distance modulus $\mu = m - M$. This can be converted to a physical distance, assuming that we are working in units of mega-parsecs (Mpc) via the following:

$$\mu = 5 \log_{10} D_L + 25\,, \tag{1.19}$$

where D_L is the luminosity distance of the observed objects. More generally the luminosity distance can be calculated from an object's observed intrinsic luminosity (L) and measured flux (F) via:

$$F = \frac{L}{4\pi D_L^2}\,. \tag{1.20}$$

Additionally for a flat Universe it is related to the comoving distance as:

$$D_L = (1 + z)\chi\,. \tag{1.21}$$

The accuracy of distance calculations using this method is highly dependent on the accuracy of luminosity information from objects like supernovae, see Section 2.2.4. This, in turn, affects the values of cosmological parameters that are determined using this data.

1.5 Hubble's Law

Hubble's law is a fundamental principle in cosmology that describes the relationship between the distance to a galaxy and its observed redshift. The history of which dates back the early 20th century when Slipher (1915) first measured the redshifts of several spiral nebulae (now known as galaxies) and found that they were all moving away from us . However, it was not until Edwin Hubble's work in the 1920s using larger telescopes and improved methods for measuring distances that this phenomenon was fully understood.

In 1929, Hubble published his landmark paper showing how he had used Cepheid variable stars as "standard candles" to measure distances to many nearby galaxies. This was done using line-spectra and the redshifts of galaxies. He then compared these distances with their observed redshifts (which he interpreted as Doppler shifts due to motion) and found a linear relationship between them. Now known as Hubble's Law this relationship dictates that galaxies are moving away from us at speeds proportional to their distance, with more distant galaxies receding faster than nearby ones,

$$v_r = cz = H_0 D\,. \tag{1.22}$$

In this analysis, we have utilised the small-speed approximation ($v/c << 1$) for the relationship between redshift and velocity in the first equation. Where v_r is the radial (recessional) velocity, z is the redshift and H_0 is Hubble's constant, with the sub-scripted "0" refers to the current epoch, with a numerical value of

$$H_0 = 100h\,\mathrm{kms^{-1}Mpc^{-1}}\,. \tag{1.23}$$

The little h in the formula is a dimensionless number measured to an precision of $h = 0.674 \pm 0.005$ (Planck Collaboration et al., 2020b). The exact value of this h is a sensitive topic to many cosmologists who have been frustrated by its measurement for a decade, a more in depth discussion can be found in Section 2.3.2.

1.5.1 Deviations due to Peculiar Velocities

By utilising photometry, we can directly measure the two transverse angular coordinates of galaxies perpendicular to the line-of-sight. Additionally, their radial coordinate can be indirectly determined by converting the measured redshift obtained from spectroscopy into distance using Eqn. 1.13. However, it was soon realised that not all galaxies followed this simple pattern.

In some cases, individual galaxies or groups of galaxies appeared to have additional motions beyond what could be explained by cosmic expansion alone. These deviations from expected motion were termed “peculiar velocities”, and are the additional velocity components that arise due to gravitational interactions between nearby objects. This is an effect that can be seen within our Local Group, without this additional velocity component the Milky Way would not be heading towards a collision course with Andromeda. The relation for close objects (in a cosmological sense) can be approximated by

$$v_r = v_{H,r} + v_{\mathrm{pec},r} \, . \tag{1.24}$$

The observed velocity (v_r) of a galaxy represents a combination of its cosmic Hubble expansion velocity ($v_{H,r}$=H_0D) and its line-of-sight peculiar velocity.

In practice, this also means that the observed redshift has a peculiar component as well, with a relationship following:

$$z_{\mathrm{pec}} = \sqrt{\frac{1 + v_{\mathrm{pec}}/c}{1 - v_{\mathrm{pec}}/c}} - 1 \approx \frac{v_{\mathrm{pec}}}{c} \, . \tag{1.25}$$

In effectively all practical situations involving the study of peculiar velocities, the non-relativistic approximation ($v = cz$) is adequate. Thus a galaxy will have an observed redshift of

$$1 + z_{\mathrm{obs}} = (1 + z_{\mathrm{cosmo}})(1 + z_{\mathrm{pec}}) \, . \tag{1.26}$$

As a result Eqn. 1.26 introduces a change in the observed clustering patterns compared to what would be measured if their true distances were known. This phenomenon, described first by Kaiser (1987), is referred to as Redshift Space Distortions (RSD).

Chapter 2

Cosmology with Peculiar Velocities

This thesis is primarily focused on understanding how well linear perturbation theory is able to recover peculiar velocities using the underlying distribution of galaxies and understanding the potential biases in nearby low-redshift reconstructions, specifically within a range of less than 200 h^{-1}Mpc.

An advantage of studying low-redshift data is that we not only have access to accurate galaxy distribution maps but also measurements of peculiar velocities. While the galaxy distribution may not perfectly represent the underlying mass density, due to galaxy bias, according to the equivalence principle galaxies share the same gravitational acceleration field as this underlying mass. Numerous methods have been proposed for the reconstruction of density and peculiar velocity fields, including studies by Bertschinger & Dekel (1989); Nusser & Davis (1994); Fisher et al. (1995); Bistolas & Hoffman (1998); Zaroubi et al. (1999); Erdogdu et al. (2006); Kitaura et al. (2010); Jasche et al. (2010); Courtois et al. (2012); Ma et al. (2012); Kitaura (2013); Jasche & Wandelt (2013); Wang et al. (2013); Springob et al. (2014); Carrick et al. (2015); Lavaux (2016); Nusser (2017); Jasche & Lavaux (2019); Graziani et al. (2019); Zhu et al. (2020); Boruah et al. (2020); Nusser et al. (2020); Kitaura et al. (2021); Qin et al. (2023). Some of these will be expanded upon in Section 2.4.

However, accurately and precisely recovering the velocity field from galaxy redshift surveys is difficult due to several limitations:

1. The density field is sampled by a finite number of discrete tracers, such as galaxies. This results in “shot noise” which prevents an accurate derivation of the density field itself.

2. Any adopted dynamical relation for velocity reconstruction introduces systematic and random uncertainties. Particularly in regions with significant density contrasts it is not possible to capture all dynamical effects even with knowledge of the full density field.

3. Galaxy redshift surveys measure redshifts rather than proper distances. There are two types velocities that are labelled as peculiar which represents coherent and incoherent motion. The latter generates artificial smearing effects such as the "Fingers-of-God" effect, distorting observed structures along the line-of-sight on scales of a few megaparsecs. The former, which can be described using perturbation theory, results in what is known as the "Kaiser effect", wherein the coherent motions of galaxies towards the centre of a supercluster during its assembly cause an apparent flattening of observed structure in redshift space.

4. Flux limits in these surveys results in only finite volumes being probed. However galaxies observed are still being influenced by gravitational interactions from large-scale structures outside survey boundaries, which affects the measured velocity fields within these volumes.

To mitigate the effects of nonlinear evolution, incoherent motions, and shot noise, it is necessary to apply a smoothing procedure to the galaxy distribution. However, this smoothing process results in the loss of small-scale density fluctuations that are present in observed velocities from distance indicator catalogues. This becomes particularly relevant when comparing reconstructed velocities with observed galaxy velocities since mismatched scales can introduce systematic uncertainties into inferred parameters (Davis et al., 1996; Berlind et al., 2000; Nusser et al., 2020).

The reconstruction process relies on a relationship implied by gravitational instability theory, see Section 2.1, which relates the velocity field to the underlying density field.

2.1 Peculiar Velocities from Gravitational Instabilities

The current cosmic web of large-scale structure that we observe originated from tiny density fluctuations following the period of inflation. Over time, these small fluctuations grew into the significant over-densities that are observable today due to the influence of gravity in an expanding universe. LSS theory provides a link between cosmological observables, such as the number density of objects with a specific mass or the likelihood for two objects to be separated by a particular distance scale, and cosmological parameters like dark matter and dark energy properties. While this section briefly outlines the process of structure formation, a more detailed description can be found in Mo et al. (2010).

The density field $\rho(x)$ can be represented as a combination of a homogeneous mean density and a perturbation ($\delta(x)$):

$$\rho(\mathbf{x}, t) = \bar{\rho}(\delta(\mathbf{x}, t) + 1)\,. \tag{2.1}$$

2.1.1 Relating the Density and Velocity Fields

To describe how matter (specifically pressure-less and non-relativistic matter) evolves over time, three equations come into play. These are the continuity, Euler, and Poisson equations:

$$\frac{\partial \rho}{\partial t} + \nabla \cdot (\rho \mathbf{v}) = 0\,, \tag{2.2}$$

$$\frac{\partial \mathbf{v}}{\partial t} + (\mathbf{v} \cdot \nabla)\mathbf{v} + \frac{1}{\rho}\nabla P + \nabla \phi = 0\,, \tag{2.3}$$

$$\nabla^2 \phi = 4\pi G \rho\,. \tag{2.4}$$

If we consider the density field as a pressure-less fluid, in these equations, $\mathbf{v}$ represents the velocity, while ϕ denotes the gravitational potential. Converting to co-moving coordinates the peculiar motion of the density field on linear scales follows the hydrodynamic equations, and one can rewrite Eqn. 2.2 as:

$$\frac{\partial \delta}{\partial t} + \frac{1}{a}\nabla \cdot \mathbf{v} = 0\,, \tag{2.5}$$

while Eqn. 2.3 becomes:

$$\frac{\partial \mathbf{v}}{\partial t} + \frac{\dot{a}}{a}\mathbf{v} + \frac{1}{a}\nabla \phi = 0\,. \tag{2.6}$$

If we then proceed to take the time derivative of Eqn. 2.5 and substitute it into the divergence of Eqn. 2.6 in conjunction with Eqn. 2.4, assuming an expanding universe and considering the first-order terms in δ and $\mathbf{v}$; the small density perturbations can be described by a second-order differential equation (Peebles, 1980; Strauss & Willick, 1995):

$$\frac{\partial^2 \delta}{\partial t^2} + \frac{2\dot{a}}{a}\frac{\partial \delta}{\partial t} = 4\pi G \rho\,. \tag{2.7}$$

This wave equation has two solutions : a growing mode and a decaying mode:

$$\delta = A(x)D_+(x) + B(x)D_-(t)\,. \tag{2.8}$$

The time dependence in the wave equation is determined solely by the functions D_+ and D_-, while $A(x)$ and $B(x)$ are dependent solely on the initial conditions. The growing mode, represented by D_+, is referred to as the growth factor. As long as density perturbations remain small compared to the background density (ie. $|\delta| < 1$), the growth of structure at all scales can be described using this growth factor.

As time progresses, the density fluctuations continue to increase in magnitude. Once δ becomes comparable to or larger than unity, the independence of Fourier modes is lost, rendering linear theory inadequate for describing the evolution of structure. This transition initially occurs at smaller scales, such as those associated with individual halos, where δ can greatly exceed unity and indicates a highly nonlinear regime.

For the simplest case, which assumes a flat universe with $\Omega_m = 1$ and no cosmological constant, Eqn. 2.7 can be expressed as:

$$\frac{\partial^2\delta}{\partial t^2} + \frac{4}{3t}\frac{\partial\delta}{\partial t} = \frac{2}{3t^2}\delta\,. \tag{2.9}$$

which has the analytic solution of:

$$\delta(x,t) = A(x)t^{2/3} + B(x)t^{-1}\,. \tag{2.10}$$

If we start from initial conditions where A and B are small, then one mode will grow while the other shrinks and so the growing mode will dominate at late times. Setting the decaying mode of Eqn. 2.8 to zero, and combining it with Eqn. 2.5 yields:

$$\nabla\cdot\mathbf{v} = -a\delta\frac{\dot{D}_+}{D_+} = -aHf\delta\,, \tag{2.11}$$

where,

$$f \equiv \frac{\mathrm{d}\ln D_+}{\mathrm{d}\ln a}\,. \tag{2.12}$$

The linear growth rate of the structure (f), is related to how quickly density fluctuations are evolving. By measuring this growth rate, we can gain insights into the evolution of these fluctuations. Over the years, various approximations have been developed by researchers to model the growth rate (Peebles, 1984; Lightman & Schechter, 1990; Carroll et al., 1992;

Lahav et al., 1991; Wang & Steinhardt, 1998; Hamilton, 2001; Linder, 2005). It is well approximated by

$$f(z) = \Omega_m(z)^\gamma \,, \tag{2.13}$$

and notably, Wang & Steinhardt (1998) were the first to suggest that

$$\gamma = \frac{6}{11} \approx 0.55 \,, \tag{2.14}$$

corresponding to a universe governed by GR and ΛCDM. This is the value assumed in this thesis.

The solution of Eqn. 2.11, provides a measure of the expected peculiar velocity $\mathbf{v}$, derived directly from the density field (Peebles, 1980; Strauss & Willick, 1995):

$$\boldsymbol{v}(\boldsymbol{r}) = \frac{Haf(\Omega_m)}{4\pi} \int \delta(\boldsymbol{r'}) \frac{(\boldsymbol{r'} - \boldsymbol{r})}{|\boldsymbol{r'} - \boldsymbol{r}|^3} d^3\boldsymbol{r'} \,. \tag{2.15}$$

2.1.2 Linear Biasing

While we are aware that the Universe is composed of both luminous baryonic matter and non-baryonic dark matter, only the luminous matter can be directly observed. Consequently, in order to understand the distribution of dark matter, it is necessary to establish a connection between the two.

To address this phenomenon, Kaiser (1984) proposed that galaxies only form in regions with high-density peaks within the mass density field. In the context of structure formation,"biasing" refers to how different types or populations of objects (such as galaxies) trace or relate to underlying matter density fluctuations. It quantifies how these objects are spatially distributed relative to regions with higher or lower densities.

The peak-background split model provides a theoretical framework for understanding this biasing effect. According to this model, there is a statistical connection between peaks in an initial density field (representing potential sites for structure formation) and their subsequent collapse into gravitationally bound structures like galaxies. Linear biasing is a specific form of this statistical connection that assumes a linear relationship between fluctuations in galaxy number counts (or other tracers) and those in underlying matter density on large scales. This assumption implies that galaxy over-densities follow similar patterns as the dark matter over-densities and on large scales, we expect linear biasing to hold such that:

$$\delta_g(\mathbf{r}) = b\delta_{DM}(\mathbf{r}) \,. \tag{2.16}$$

In this model, the relationship between the galaxy and dark matter distribution is described by a linear biasing parameter, denoted as b (often denoted with a subscript g). This is the classical approach to linear biasing, and the method we adopt for this thesis.

For a comprehensive understanding of different biasing schemes and their implications regarding scale dependence with respect to redshifts, refer to works such as Basilakos & Plionis (2001) and related references.

Assuming that we are operating within large enough distances such that the linear biasing model remains scale-independent, we can define the following expression:

$$\beta \equiv \frac{f}{b} \,, \tag{2.17}$$

where β is a proportionality factor between gravitational acceleration and peculiar velocity that can be measured from the observable density contrast of galaxies in the nearby Universe. By substituting the values from Eqn. 2.13, we obtain:

$$\beta = \frac{\Omega_m^{0.55}}{b} \,. \tag{2.18}$$

The solution for the peculiar velocity field can hence be rewritten to indicate its linear dependence on the redshift distortion parameter, β.

In this study, we have chosen to analyse the parameter β in order to explore alternative methods for estimating it. By doing so, we aim to gain a deeper understanding of the peculiar velocity field and consequently improve the measurement accuracy of cosmological parameters such as $f\sigma_8$ described in Section 4.7.1.

2.1.3 Large-Scale Structure

Galaxy bias is typically defined as the ratio between the density of galaxies and dark matter. In terms of the power spectra of galaxy and matter fluctuations,

$$b^2(k) \equiv \frac{P_g(k)}{P_{DM}(k)} \,, \tag{2.19}$$

where P_g and P_{DM} correspond to the power spectrum of galaxies and dark matter respectively and

$$P(k) \equiv \left\langle |\delta_k|^2 \right\rangle \,. \tag{2.20}$$

In this work, we will assume that b is independent of wavelength: $b(k) = b$.

In galaxy surveys, we often consider normalised versions of these cosmological parameters: $f\sigma_8$ and $b\sigma_8$. The constant σ_8 represents the root mean square (rms) value which characterises the mass fluctuation within spheres of radius of 8 h^{-1}Mpc. More generally, within a sphere of radius R the standard deviation of the amplitude of mass fluctuations, can be calculated from the power spectrum using

$$\sigma^2(R, z) = \frac{1}{2\pi^2} \int_0^{\infty} k^2 P_{\rm lin}(K, z) |W(k; R)|^2 dk \,, \tag{2.21}$$

where $W(k; R)$ is the window function. Commonly used forms include spherical top-hat

$$W(k; R) = \frac{3}{(kR)^3} [\sin(kR) - kR\cos(kR)] \,, \tag{2.22}$$

and Gaussian

$$W(k; R) = \exp(-k^2 R^2/2) \,. \tag{2.23}$$

For the linear value, $\sigma_8^{\rm lin}$, one would use the linear power spectrum, the top-hat window and $R = 8$ h^{-1}Mpc. But it is also possible to calculate the non-linear σ_8 using a non-linear power spectrum, or that of the galaxies, $\sigma_{8,g}$, using P_g.

2.2 The Cosmic Distance Ladder

At low redshifts ($z \ll 1$) the observed redshift is given by

$$cz = H_0 D + v_{\rm pec} \,. \tag{2.24}$$

In order to determine H_0 one must know the value of the proper distance, D, in physical units and account for the peculiar velocity of the observed redshift.

For nearby galaxies, peculiar velocities significantly impact the observed redshifts of individual galaxies, affecting them at the level of hundreds of kilometres per second. It is possible to obtain accurate Hubble expansion velocities by calibrating the relative distance of a nearby galaxy by comparing them to a set of distant galaxies or clusters, where for the latter peculiar velocities introduce a much smaller fractional error. Alternatively it is possible to measure accurate redshifts by “correcting” those observed by the predicted peculiar velocities, as will be explored in Chapter 5. Hence secondary distance indicators such as the Fundamental Plane relation (for elliptical galaxies), the Tully-Fisher relation (for spiral galaxies), or Type Ia supernova can be used.

The cosmological distance ladder provides a way to measure distances to celestial objects at various scales, from nearby objects within our own galaxy to distant galaxies and beyond. It relies on a series of techniques that build upon each other, like rungs on a ladder.

2.2.1 Parallax

The first rung of the ladder, is calculated by performing a geometric distance calculation, known as parallax measurements to determine distances to nearby stars. Parallax involves observing how an object appears to shift its position against more distant background stars as Earth orbits around the Sun. This was the primary technique used by the Hipparcos satellite to survey distant bodies (Feast & Catchpole, 1997). While parallax is a valuable tool for measuring relatively close astronomical objects within our galaxy and nearby stellar systems, be it clusters or individual stars; it becomes significantly less practical when dealing with much larger cosmic scales.

The maximum distance at which parallax is useful is dependent on the precision of the measurements and the capabilities of the instruments used. Generally, parallax can be reliably measured for objects within a few thousand light-years from Earth. The most accurate parallax measurements are currently obtained using the space-based telescope Gaia (Gaia Collaboration et al., 2023), which has been able to measure distances up to tens of thousands of light-years with high precision. However, at larger distances, the parallax angle subtended by even nearby stars becomes extremely small and difficult to measure accurately. Accurate parallaxes serve as crucial calibration points for various indirect methods used to estimate astronomical distances such as standard candles (objects with known luminosities).

2.2.2 Cepheids

Once accurate distances are known for nearby stars, they can be used as reference points for further steps in the distance ladder. The next step involves using a specific type of variable stars, known as Cepheid variables, as standard candles for extra-galactic objects. Cepheids are named after the prototype star, δ Cephei, which was discovered to exhibit periodic variations in its brightness. These variable stars are generally found in younger stellar populations such as open clusters and spiral galaxies. They pulsate rhythmically, expanding and contracting at regular intervals, with periods ranging from 2-150 days. This pulsation causes their brightness to vary over time. The period of these variations is directly related to the intrinsic luminosity or absolute magnitude of the star (Leavitt, 1908; Leavitt & Pickering, 1912), such that

$$M = -a - b \log \mathrm{P} \,. \tag{2.25}$$

Here P is the light variation period in days, while a and b are constants determined using local Cepheids with direct distance measurements (see Mo et al. (2010) § 2.1.3 and references therein for examples).

As the period-luminosity relationship for Cepheids is well-established, it allows for accurate absolute magnitudes to be determined based on their pulsation period. By observing the apparent brightness (or magnitude) of a Cepheid variable from Earth, combined with knowledge about its true or absolute magnitude derived from its period-luminosity relation, it is possible to calculate how far away it is located using an inverse square law approach. This makes them excellent standard candles for distance measurements in the universe over relatively large distances up to 10 Mpc. With some minor complications in the uncertainty in whether there is a strong metallicity dependence of the period-luminosity relation (e.g., Ripepi et al., 2020), as well as the effects of dust (e.g., Mörtsell et al., 2022).

2.2.3 Galaxy Scaling Relations

Tully-Fisher relation

The Tully-Fisher (TF) relation, developed by Fisher & Tully (1977), establishes a connection between two observables: the luminosity (or absolute magnitude) of a spiral galaxy in some bandpass (e.g., B-band), and its maximum rotation velocity as measured from 21-cm emission line spectroscopy.

Observations are made using spectroscopy techniques to determine accurate rotational velocities (usually measured at specific radii) within target galaxies. A calibration sample consisting of nearby galaxies with known distances through other methods such as Cepheid variables or surface brightness fluctuations is used. By comparing observed rotation velocities with known distances in this calibration sample, an empirical relationship between luminosity/mass and rotational velocity can be established. Once this correlation is known, it can be applied more broadly across other similar types/properties spirals where only their observable properties like line-of-sight speeds need measuring.

To illustrate this, consider an almost edge-on rotating spiral galaxy observed from Earth in a non-expanding Universe. As the galaxy rotates, we would observe one half of the spiral disk as blueshifted (spinning towards us) while the other half would be redshifted (spinning away from us). By using Eqn. 1.13, we can determine the velocities for both halves of the galaxy and compute their average to obtain an overall rotational velocity. A rotating spiral moving further away from an observer due to universal expansion will have one side of its disk appearing to recede more slowly (with smaller redshift), indicating rotation towards us; whereas the other will seem to be receding faster (with higher redshift), indicating rotation away from us.

This information helps in gaining a deeper understanding of galactic structure on a broader scale within the Universe. In particular, the surface brightness distribution of a typical spiral galaxy can be accurately modelled using an exponential law,

$$I(R) = I(0) \exp\left[\frac{-R}{R_D}\right] , \tag{2.26}$$

where $I(0)$ represents the central surface brightness and R_D denotes the disk scale length. By integrating over the area of the disk, the luminosity of the galaxy can be obtained, $L_D = 2\pi I(0) R_D^2$. The exponential law models the galaxy out to an infinite radius, however the luminosity of the galaxy eventually tends to converge after a few scale lengths (α). At this point, which represents maximum rotation, the rotational velocity of the galaxy should reach its peak value denoted as V_{max}. In order for a spiral galaxy to maintain stability, its total rotational velocity calculated through Doppler shift must be equal to its gravitational acceleration according to Newtonian mechanics, i.e.

$$v^2 = \frac{GM(r)}{r} , \tag{2.27}$$

where $M(r)$ represents the mass of the galaxy and up to and including radius r, and G denotes the gravitational constant. By substituting the maximum rotational velocity out to radius αR_D, squaring Eqn. 2.27, substituting in L_D and assuming both $I(0)$ and the mass to light ratio are constant, gives the Tully-Fisher relation:

$$L_D = AV_{max}^4 , \tag{2.28}$$

where A is a constant that depends on the galaxy's mass and its type. The exponent in the TF relation also varies due to factors like stellar population age, metallicity gradients, the observation band and most importantly dark matter as makes up a significant portion the galaxy's mass (e.g., Tully et al., 1998; Courteau et al., 2007; Masters et al., 2008; McGaugh, 2012). It has been found that using microwave-to-infrared (K-band) radiation as a proxy for stellar mass yields a tighter relationship with an exponential slope closer to our theoretical approximation of $\alpha = 4$ in Eqn. 2.28 (eg. Tully & Pierce, 2000). Furthermore, considering baryonic mass instead of luminosity leads to a stronger correlation known as the Baryonic Tully-Fisher Relation (BTFR) (Freeman, 1999; McGaugh et al., 2000).

Fundamental Plane Relation

The analogue to the TF relation for elliptical galaxies is known as the Faber-Jackson relation (Faber & Jackson, 1976), relating a galaxy's luminosity to it's central velocity dispersion, σ:

$$L \propto \sigma_e^4 \,. \tag{2.29}$$

However it was noted by Dressler et al. (1987) and Djorgovski & Davis (1987) that a tighter relationship could be developed with the introduction of a third parameter, surface brightness. As ellipticals exhibit significant correlations with both luminosity and galaxy size, relating the luminous diameter D_n and the velocity dispersion gives:

$$D_n \propto \sigma_e^{\gamma} \,, \tag{2.30}$$

which has been utilized in many studies involving peculiar velocities (such as Lynden-Bell et al., 1988, which found $\gamma = 1.2 \pm 0.1$).

The $D_n - \sigma$ relation and variants can be considered manifestations of elliptical galaxies' Fundamental Plane (FP). FP relations represent the correlation between the effective radius R_e (radius which encloses half the galaxy's light), the mean effective surface area, $\langle\mu\rangle_e$, and the central velocity dispersion, σ. The FP can be expressed mathematically as:

$$\log(R_e) = a\log(\sigma) + b\langle\mu\rangle_e + c \,, \tag{2.31}$$

where a, b, and c are coefficients representing the slope and zero-point of the plane, which determined empirically from observations.

This relation has important implications for our understanding of galaxy formation and evolution processes, as it suggests that there exists some underlying physical mechanism(s) governing how these galaxies form and/or maintain their structure over time. Ellipticals are virialised systems. If the mass-to-light ratio is known exactly then the viral theorem can predict the coefficients of Eqn. 2.31. However the measured values do not exactly agree with the theory. This difference is called the "tilt" of the FP. The degree to which measurements deviate is heavily dependent on their mass-to light ratios, which in turn is dependent on the galaxy's star formation histories and other processes. Additionally environmental effects such, galaxy mergers or feedback mechanisms could alter the relation (see D'Onofrio & Chiosi, 2022; Mould, 2020, and references therein).

2.2.4 Type Ia Supernovae

White dwarfs are the remnants of stars that did not have enough mass to collapse into a neutron star or black hole at the end of their evolutionary cycle. Instead, they undergo

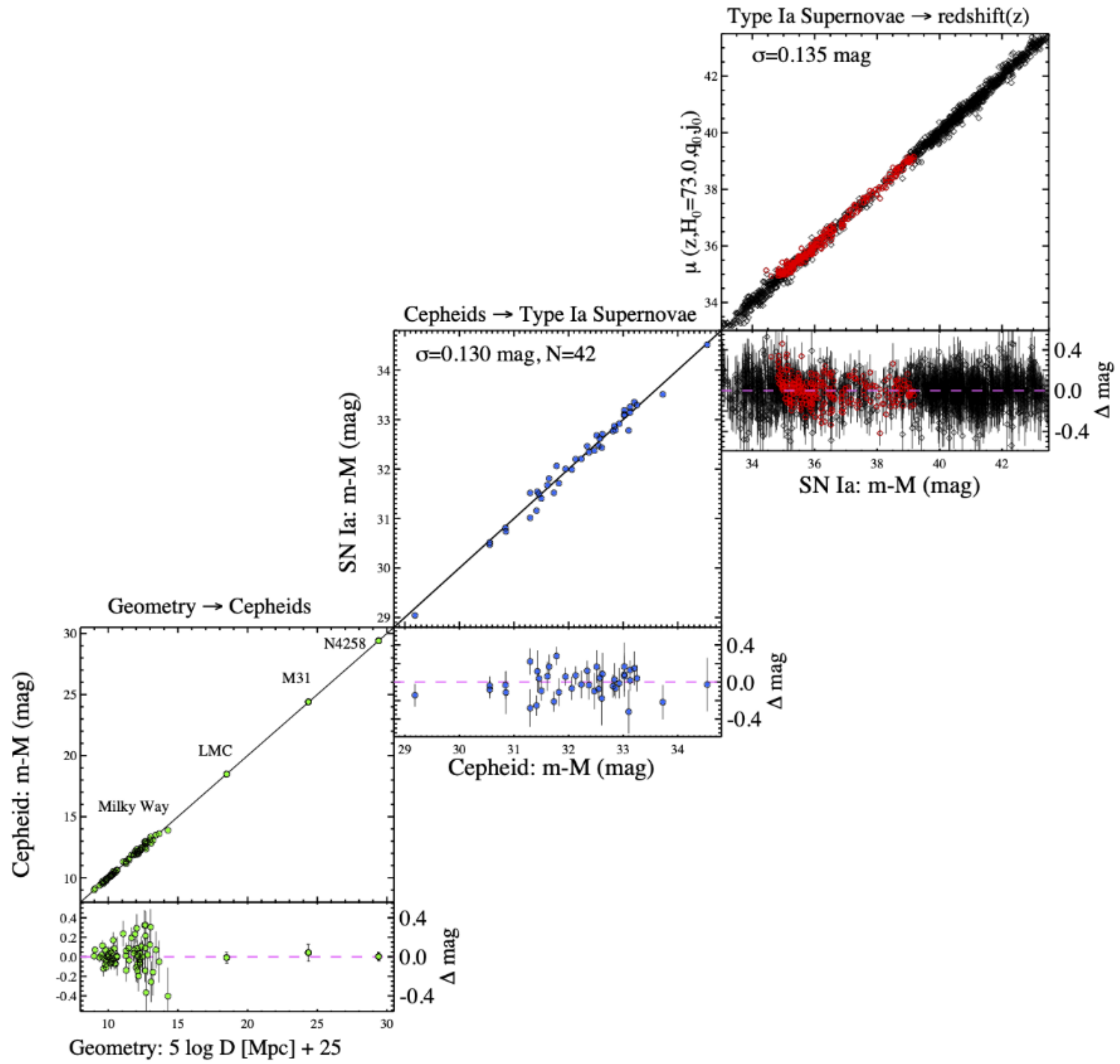

Figure 2.1: The complete distance ladder, which is determined by the agreement of different pairs of distances. These include (lower left) geometric and Cepheid-based measurements, (middle) Cepheid and SNe based measurements, and (top-right) SNe and redshift-based measurements. The measurement of H_0 is obtained through the simultaneous agreement of these distance pairs. Each rung on the ladder involves using geometric or calibrated distances on rung to calibrate a relative distance indicator the next rung. Shown here are the results for an approximate global fit. The red data points represent SNe at $0.0233 < z < 0.15$. Taken from Riess et al. (2022).

a collapse and form an extremely dense stellar remnant composed mainly of electron-degenerate matter (high-energy electron plasma). Typically, these white dwarfs do not exceed 1.44 times the mass of our Sun (known as the Chandrasekhar limit), but this mass is packed into a volume equivalent to that of Earth.

Type Ia supernovae (SNe Ia) specifically require a white dwarf star to be part of a binary system. The high density of the white dwarf leads to its strong gravitational force, causing it to accrete mass from its companion star over time. Once the critical limit is exceeded, a nuclear chain reaction is initiated within the core of the white dwarf, leading to an explosive event. Since all SNe Ia trigger similar nuclear reactions in their progenitor stars' cores, they exhibit consistent levels of brightness during their explosions. They have high intrinsic luminosity and follow well-defined patterns and thus serve as excellent indicators for measuring astronomical distances accurately, as this provides a measurement of the distance modulus (Eqn. 1.19).

These SNe have long been recognised as standard candles in cosmology, providing valuable insights into the acceleration of the Universe's expansion. It worth noting that SNe Ia are not perfectly consistent in their brightness. For instance in the near-UV band, they exhibit scatter in their absolute magnitudes of ~ 0.3 (Brown et al., 2010), which corresponds to overall uncertainty in distance estimates of $\sim 14\%$. However, there are empirical correlations between the peak apparent magnitude and other properties of the light curve, and corrections must be made to account for its stretch (s: broadness and decline time (Perlmutter et al., 1997)) and colour measure (c: difference in magnitude between two bands (Wang et al., 2003)). This results in additional nuisance factors into the simple distance modulus relation:

$$\mu = m - M + \alpha(s-1) - \beta c\,, \tag{2.32}$$

where α and β are, respectively, the stretch and linear response factors. These correlations allow for the standardization of SNe Ia by reducing the intrinsic scatter.

In addition to their role in measuring cosmic acceleration, nearby Type Ia supernovae can also be utilised to estimate peculiar velocities for their host galaxies. This is due to the fact that the peculiar velocity of a SNe causes a discrepancy between the observed redshift and the redshift resulting from the overall expansion of the Universe. As the observed brightness of a SNe can be used to determine the latter, one can effectively use the observed redshift to constrain and understand the relative peculiar velocity along the line-of-sight, using Eqn. 2.24. Compared to galaxy scaling relations, SNe Ia offer a much higher level of precision with distance estimates typically falling within a range of $\sim 5-15\%$. The calibration of absolute magnitudes can be achieved through two independent methods:

empirical calibration using Cepheid-based distances to parent galaxies of SNe Ia, and physical calibration based on light curve and spectrum fitting.

Peculiar velocity predictions also play a significant role in correcting SNe Ia measurements to obtain cosmological redshifts to be used for measurements of the Hubble constant (e.g., Scolnic et al., 2018; Riess et al., 2022). In Chapter 5 of our work we will provide further details about our own research where we focus on well our method is able to correct for peculiar velocities of low redshift SNe Ia and how this propagates into measurements of the Hubble parameter.

Supernova Catalogues

Over the past 15 years, numerous high-quality data-sets of supernovae have been made available. Notable data-sets include that of the "Union" compilation (Kowalski et al., 2008; Amanullah et al., 2010; Suzuki et al., 2012), the Constitution set (Hicken et al., 2009), SDSS (Kessler et al., 2009; Betoule et al., 2014), the Supernova Legacy Survey (Conley et al., 2011; Betoule et al., 2014), Pan-STARRS (Tonry et al., 2012; Scolnic et al., 2014) along with the Pantheon sample (Scolnic et al., 2018). In addition to these, there is the a data-set used in thesis : "Pantheon+SH0ES" (Scolnic et al., 2022), which is comprised of 1701 observations of 1550 spectroscopically confirmed Type Ia supernovae within a redshift range of $z = 0$ to $z = 2.3$.

However, as the number of discovered SNe Ia has rapidly increased, there has been a growing focus on studying their associated systematic uncertainties. It has been demonstrated by Weinberg et al. (2013) that the traditional magnitude statistical method for analysing SNe Ia data, is susceptible to various systematic uncertainties. These include calibration errors (Conley et al., 2011), host-galaxy extinction effects (Kelly et al., 2010; Lampeitl et al., 2010; Sullivan et al., 2010), gravitational lensing influences (Frieman, 1996; Wang, 1999), variations in light-curve fitting methods (Hu et al., 2016), and redshift-dependent changes in the colour-luminosity parameter of SNe, β (Wang & Wang, 2013; Mohlabeng & Ralston, 2014; Wang et al., 2014a,b,c; Li et al., 2016). Consequently, the mitigation of these systematic uncertainties associated with SN cosmology poses significant challenges for researchers in this field.

2.3 Peculiar Velocity Surveys

Measuring distances to galaxies is a challenging task in observational astronomy. One commonly used method for obtaining peculiar velocity data relies on empirical galaxy scaling relations, see Section 2.2.3. Typically, these galaxy-scaling relations provide distance estimates with an accuracy of around 15-25% (Masters et al., 2006; Springob et al., 2007; Tully et al., 2013, 2016, 2023). Hence rather than obtaining peculiar velocities for individual galaxies, it is generally preferable to obtain peculiar velocity data for groups of galaxies. Averaging over redshifts within a group of galaxies while considering multiple distance measurements from its member objects can lead us towards a more accurate estimation of their collective distance properties.

Several surveys have been conducted to measure the peculiar velocities of galaxies. Notably, the SFI++ catalogue (Masters et al., 2006; Springob et al., 2007) and 2MASS Tully-Fisher (2MTF; Masters et al. (2008); Hong et al. (2019)) surveys have successfully determined distances for thousands of galaxies using the TF relation. The 2MTF employs three infrared bands for distance measurements and demonstrates an intrinsic scatter of approximately $\sigma_{int} \sim 0.3$ mag in the TF relation, while the SFI++ survey, using the I-band TF relation, exhibits a higher precision of $\sigma_{int} \sim 0.4$ mag. However, it is worth noting that infrared bands are less susceptible to certain systematic effects such as dust extinction. Previously, one of the most extensive peculiar velocity surveys is based on data from the 6-degree Field Galaxy Survey which is a dual redshift (6dFGSz) and peculiar velocity survey (6dFGSv) (Springob et al., 2014). This particular study uses a different approach by employing the FP relation to estimate distances and initially compiled distance and peculiar velocity estimates for a substantial 11287 galaxies, but after removing galaxies with large recessional velocities is reduced to sample size consisting of 8885 galaxies.

However, the availability of peculiar velocity samples has been rapidly increasing. Notably, the *Cosmicflows-IV* (CF4) dataset (Kourkchi et al., 2022; Tully et al., 2023) now includes over 55,000 distances, while the SDSS Peculiar Velocity Catalogue (Howlett et al., 2022) contains approximately 34,000 distances. Furthermore, upcoming surveys conducted with instruments like the Dark Energy Spectroscopic Instrument (DESI; DESI Collaboration et al. (2016)) and the Four-Metre Multi-Object Spectroscopic Telescope (4MOST; de Jong et al. (2019)) will have even greater capabilities and are expected to provide redshifts for millions of galaxies and peculiar velocity measurements for several hundreds of thousands. We present these in more detail in Section 6.2.

2.3.1 Malmquist Bias

The term “Malmquist bias” is commonly used to describe biases that arise from the spatial distribution of objects. It was first noted in Eddington (1914) and a more general formula was later derived by Malmquist (1920, 1924). This bias occurs due to the interplay between random distance errors and density variations along the line of sight. The presence of these density fluctuations complicates modelling the probability distribution for distances, as it cannot be simply represented by a Gaussian centred on the measured distance along the line of sight.

There are two types of Malmquist bias that need to be considered. The first type arises from the probability of including a galaxy with a given apparent magnitude in a sample, which varies depending on the distance to that galaxy. This variation is influenced by factors such as: 1) the shape of the luminosity function, which is not perfectly flat; 2) there being more galaxies at larger distances within a given solid angle compared to smaller distances; and 3) potential variations in the selection function for galaxies based on distance or redshift. The consequence of this bias is that the observed sample will over-represent bright objects compared to their true distribution in the universe. Due to the limitations of our observations being confined to a sphere centred on us, the number of observable galaxies increases as we look further into space due to the homogeneity of the Universe. As a result, when considering an *estimated* distance (r_e) there is a greater probability that it lies at a higher true distance (r) and was scattered down than the reverse, given that volume increases as a function of distance. Consequently, there is an increased probability that galaxies with distance estimates closer to r have actually been located even closer than estimated. As a result distances are more likely to be underestimated. The average distance of a galaxy with an estimated distance r_e is given by:

$$\langle r \rangle = r_e[1 + (1/2 + \alpha)\Delta^2]\,, \tag{2.33}$$

where Δ is the scatter in the distance and $\alpha = 3$ for a uniform distribution [for further details regarding this derivation refer to Lynden-Bell et al. (1988)]. In practice, this becomes even more complex due to the presence of small-scale structures in space. This can lead to incorrect conclusions about various properties such as luminosity or distance measurements when analysing data from these surveys. To account for this, as was originally proposed in Malmquist (1920) one can correct the average absolute magnitude from the sample ($\bar{M}$) by the true intrinsic absolute magnitude (M_0), i.e.

$$\langle M \rangle = \bar{M} - M_0\,. \tag{2.34}$$

While this bias is consistent across different regions of the sky, there exists another form known as inhomogeneous Malmquist bias (Dressler & Faber, 1990). This second type emerges due to variations in large-scale structure along lines of sight. Failing to account for this particular bias can lead to misleading infall signatures towards high-density regions.

Various correction schemes have been developed for addressing Malmquist biases in peculiar velocity samples, for instance for the SFI catalogue data this has been done by using: numerical Monte Carlo techniques (e.g., Freudling et al., 1995; da Costa et al., 1996; Branchini et al., 2001), a semi-analytic approach (Freudling et al., 1999), or selection functions (Park & Park, 2006). Correcting for both the inhomogeneous Malmquist bias arising from large-scale structure and the homogeneous Malmquist bias resulting from volume effects and the luminosity function can be relatively straightforward, especially if a reconstruction of the local density field is available. This correction has been performed on density fields such as 2MASS (Pike & Hudson, 2005) and 2M++ (Boruah et al., 2020). However, an additional challenge arises when accounting for the selection criteria used to define a sample. This becomes particularly problematic when dealing with data-sets that have highly heterogeneous selection criteria. As this thesis primarily deals with N-Body simulations we do not explore this topic in much detail.

2.3.2 Hubble Tension

The phrase “Hubble tension” refers to a discrepancy between measurements of the current expansion rate of the Universe, known as the Hubble constant. There are two main methods used to measure this constant: one based on observations of nearby objects (using techniques such as supernovae, Cepheid variables, or gravitational lensing), and another based on studying fluctuations in CMB radiation from shortly after the Big Bang. The tension arises because these two different methods yield slightly, but significantly, different values for the Hubble parameter. Figure 2.2 shows a variety of recent H_0 measurements using a multitude of techniques, and visually demonstrates the discrepancy that exists to various degrees dependent on the method. It highlights two of the most precise current measurements, the late time observations calculate $H_0 = 73.04 \pm 1.04$ km s^{-1} Mpc^{-1}(Riess et al., 2022), which exhibits a tension of 5.0σ with the CMB measurement of 67.36 ± 0.54 km s^{-1} Mpc^{-1}(Planck Collaboration et al., 2020b). This has led to ongoing debates and investigations into potential sources of systematic errors or new physics that could explain this discrepancy.

The combination of data from various sources including SNe observations, CMB radiation analysis, and weak lensing studies among others, allow for additional tests to be performed on the background expansion and determine whether GR is capable of describing the rate of structure growth. Over the past decade, studies have obtained more accurate estimates for cosmological parameters like the Hubble constant, but have not come to a unanimous conclusion on why discrepancies exist between early and late time measurements. For a comprehensive review see Abdalla et al. (2022).

Several reviews, including those by Knox & Millea (2020),Beenakker & Venhoek (2021) and Di Valentino et al. (2021), have discussed potential modifications to the base ΛCDM

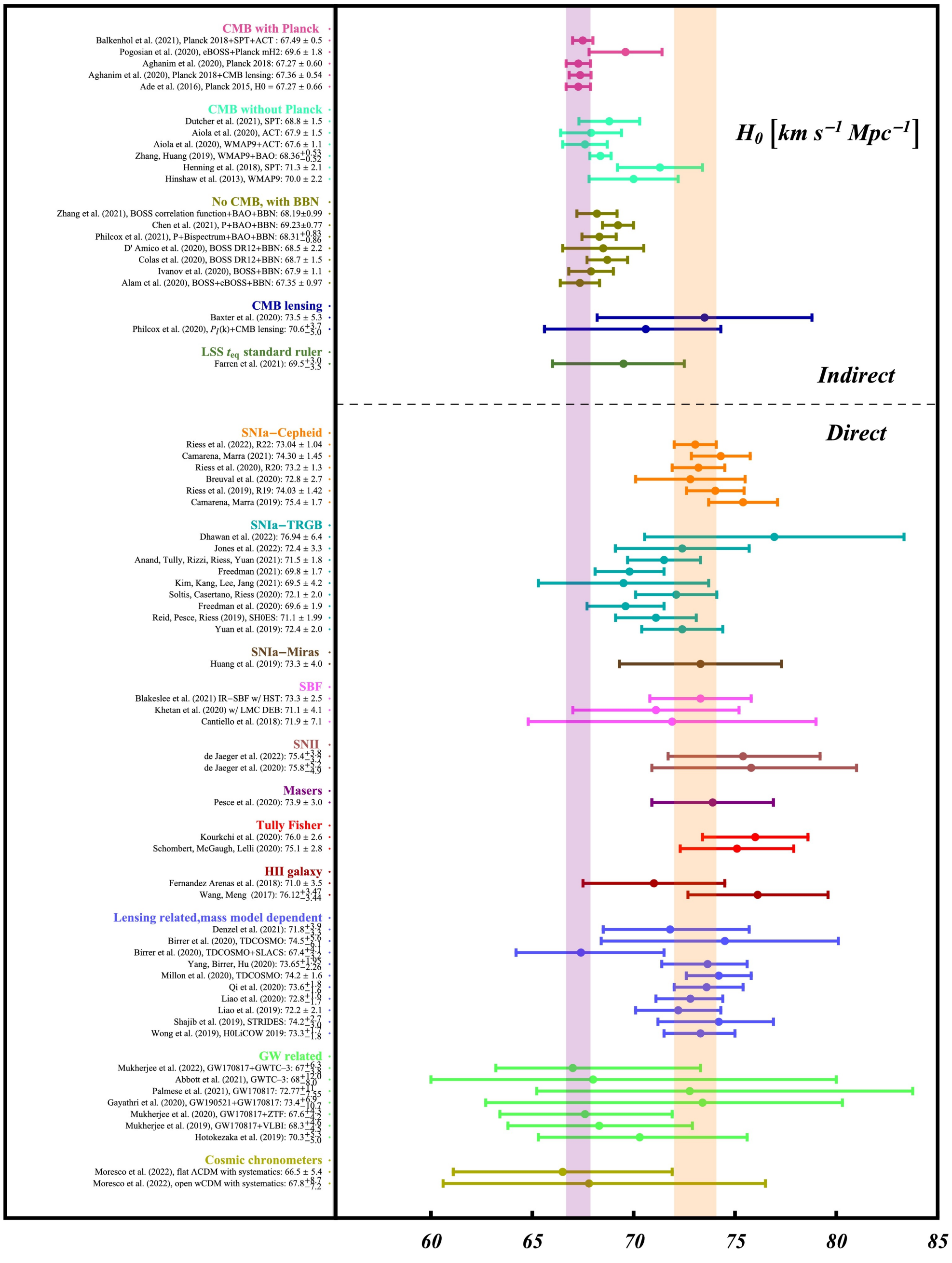

Figure 2.2: H_0 Measurements from a variety of probes demonstrating the tension between direct (late-type) and indirect (early-type) measurements under the assumption of a given cosmological model of the Hubble parameter. The Planck Collaboration et al. (2020b) measurement is shown by the purple band, while the orange shows the Riess et al. (2022) measurement. Taken from Abdalla et al. (2022).

model that could address this tension. These proposed solutions can be broadly categorised via the following:

1. Extreme departures from conventional cosmology, which may involve deviations from General Relativity.
2. Changes to early Universe physics, such as the introduction of additional relativistic species or neutrino interactions.
3. Introduction of new physics at the matter-radiation equality or recombination that could impact the value of the sound horizon.

2.3.3 S_8 Tension

The tension between the value of the matter energy density (Ω_m) and the amplitude of growth rate of structure (σ_8, $f\sigma_8$) as probed by weak lensing, is often quantified in terms of $S_8 \equiv \sigma_8\sqrt{\Omega_m/0.3}$. Here again there exists a discrepancy between measurements obtained using the CMB versus weak lensing surveys and other probes of the Universe at late times, with a higher value of $S_8 = 0.834 \pm 0.016$ as measured by (Planck Collaboration et al., 2020b), and a lower value of $0.759^{+0.024}_{-0.014}$ from cosmic shear measurements (Asgari et al., 2021). Figure 2.3 demonstrates the constraints placed by these measurements on cosmological parameters.

Although less statistically significant than the H_0 tension, it still raises concerns as it appears consistently in various weak lensing measurements that agree with other cosmological probes related to the growth history of the Universe (see a comprehensive review by Abdalla et al., 2022, for more details). Resolving both tensions simultaneously becomes challenging since many theoretical methods that increase H_0 for CMB measurements also lead to an increase in S_8. As a result, resolving this S_8 tension remains an unsolved problem within modern cosmology and will be an important area for future research.

A similar tension can be found in closely related parameter combination known as $f\sigma_8 = \Omega_m^{0.55}\sigma_8$. The inferred measurement of $f\sigma_8$ using the Planck Collaboration et al. (2020b) values implies a value of $f\sigma_8(z=0) = 0.430 \pm 0.007$. This parameter is probed via peculiar velocities whether through Redshift Space Distortions (RSD) or through direct peculiar velocity measurements, as is performed in this thesis.

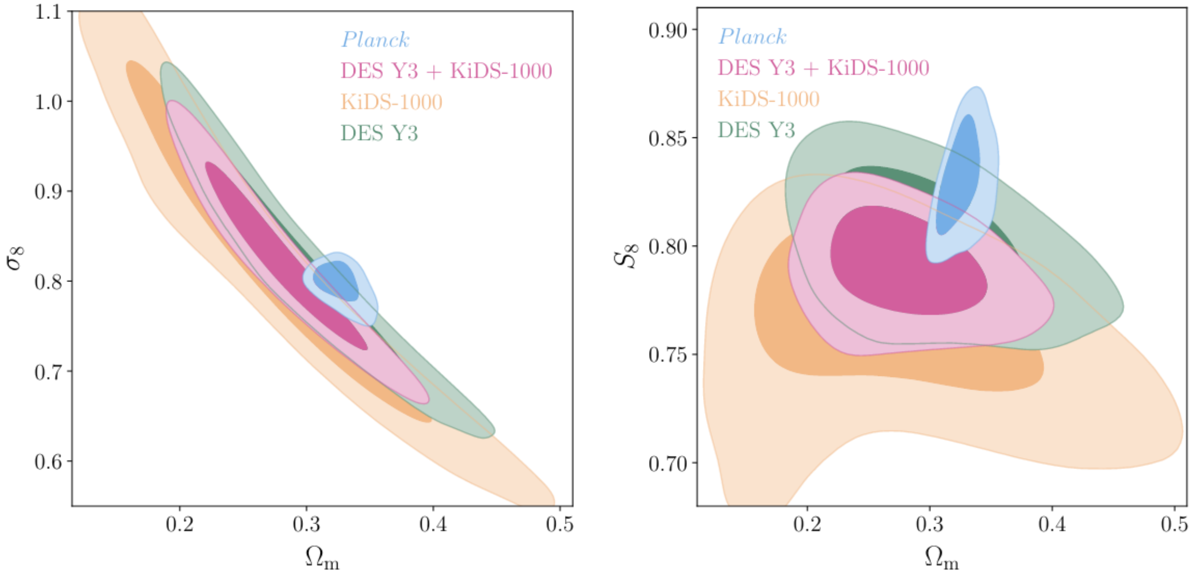

Figure 2.3: The cosmological constraints on the parameters σ_8 (left) and S_8 (right), against matter density (Ω_m) in a flat-ΛCDM cosmology. Shown here are the Planck Collaboration et al. (2020b) (blue) measurements, and the cosmic shear measurements from KiDS-1000 (orange) Asgari et al. (2021), DES Year 3 (green) Secco et al. (2022) and their joint constraint (pink) DES Collaboration et al. (2023). The marginalised posterior contours represent 68% (95%) credible intervals for inner (outer) contours. Taken from DES Collaboration et al. (2023).

2.4 Peculiar Velocities and the Growth Rate

For surveys that solely consist of galaxy redshifts, a common approach to extract cosmological information is converting these redshifts into distances and examining the spatial correlations between pairs of galaxies. This analysis provides measurements of the power spectrum (in Fourier space) or correlation function (in configuration space) for the density field represented by the galaxy sample. One can use the correlation function as a measure of the degree of clustering in cosmology, this can be represented by spherical harmonics. Among these harmonics, the quadrupole term (ξ_2) specifically describes the anisotropic clustering resulting from RSD. On large scales, there exists a linear relationship between the growth rate of structure and ξ_2. This property makes RSD a valuable tool for testing cosmological parameters at intermediate redshifts ($0.2 \lesssim z \lesssim 1$). Some recent measurements include studies by Yuan et al. (2022) using DESI finding $f\sigma_8(z_{eff} = 0.52) = 0.444 \pm 0.016$, Gil-Marín et al. (2016) found $f\sigma_8(z_{eff} = 0.38) = 0.489 \pm 0.038$ and $f\sigma_8(z_{eff} = 0.61) = 0.455 \pm 0.028$ from SDSS-III BOSS DR12 data and Chapman et al. (2023) find $f\sigma_8(z_{eff} = 0.737) = 0.368 \pm 0.041$ using the luminous red galaxy sample of eBOSS.

In peculiar velocity surveys, however, each galaxy has both a measured peculiar velocity and a corresponding redshift or distance. As peculiar velocities are a result of the gravitational interactions between galaxies and the underlying density field, techniques using peculiar velocity surveys to measure the growth rate (at very low-redshifts $z < 0.07$) and galaxy bias has been extensively studied in previous research (for a comprehensive review refer to Strauss & Willick (1995)).

Therefore, in addition to studying correlations between galaxy pairs, it is possible to examine correlations between their velocities. This enables measurements of the velocity power spectrum as well as cross-correlations between a galaxy's velocity and another galaxy's position, which yields insights into the velocity-density cross-power spectrum. This approach offers advantages such as partially mitigating sample variance issues arising from differences in both density and velocity fields while overcoming certain limitations associated with cosmic variance. In this section, we review some of the recent methods performed on with peculiar velocities to constrain the growth rate ($f\sigma_8$).

When two galaxies are randomly selected, the peculiar velocity of one galaxy with respect to the other is directed towards each other due to gravitational attraction. This phenomenon occurs as these galaxies trace over-dense regions. Simulating and analysing the pairwise velocities of galaxies, enabling constraints on cosmological parameters. Recently, Dupuy et al. (2019) utilised this method on the CF3 dataset and obtained a constraint

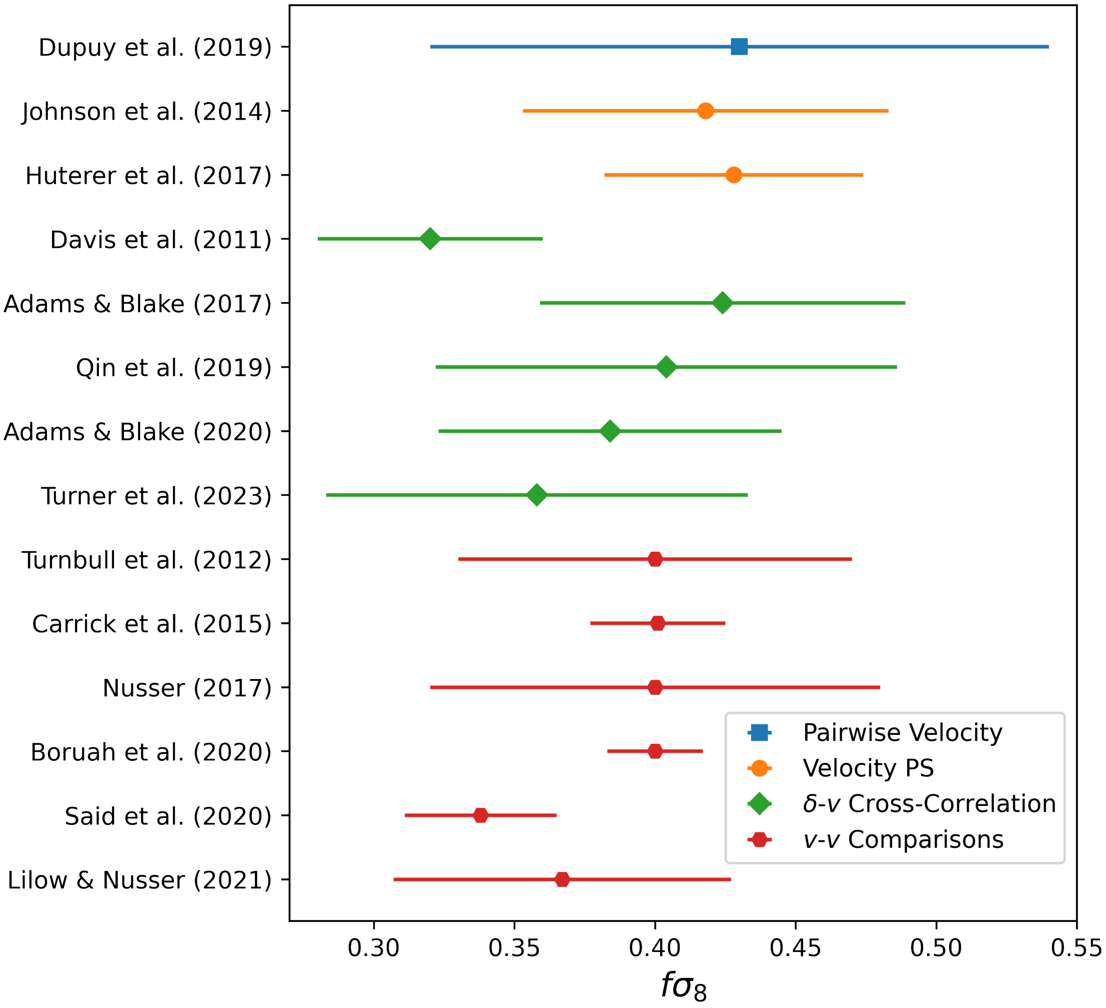

Figure 2.4: Constraints on $f\sigma_8$ from recent peculiar velocity analyses. Shown here are the values for the methods described in the text of pairwise velocities (blue), peculiar velocity covariance (orange), velocity-density cross-correlations (green), and velocity-velocity comparisons (red).

of $f\sigma_8 = 0.43 \pm 0.03$ (stat) ± 0.11 (sys). The covariance of galaxies peculiar velocities at various separations can be modelled using ΛCDM. By comparing the observed correlation with predictions, it becomes possible to constrain cosmological parameters. This approach has been employed in studies such as Johnson et al. (2014) and Huterer et al. (2017), who found $f\sigma_8(z = 0) = 0.418 \pm 0.065$ and $f\sigma_8(z = 0.02) = 0.428^{+0.048}_{-0.045}$ using the 6DFGSz and CF2 catalogues respectively. Additionally, this method allows for the measurement of a scale-dependent growth rate as demonstrated by Johnson et al. (2016). This can serve as a test for certain modified gravity theories, as GR predicts a scale-independent growth and specific patterns of redshift distortions in the linear regime, and deviations from predictions allow for the constraint of the cosmological model. Furthermore, cross-correlating these velocity measurements with galaxy distributions provides complementary insights into this field of study, recent measurements of $f\sigma_8$ (and relevant data-sets) using this method include: Davis et al. 0.32 ± 0.4 (SFI++ + 2MASS; 2011), Adams & Blake $0.424^{+0.067}_{-0.064}$ (6dFGSz + 6dFGSv;2017), Qin et al. $0.404^{+0.082}_{-0.081}$ (2MTF + 6dFGSv;2019), Adams & Blake 0.384 ± 0.052 (stat) ± 0.061 (sys) (6dFGSz + 6dFGSv; 2020) and Turner et al. 0.358 ± 0.075 (6dFGSz + 6dFGSv; 2023).

The method that we use in thesis is the comparison of measured peculiar velocities to those predicted from the underlying density field using linear perturbation theory. This method referred to as "velocity-velocity" or "velocity-density" comparisons. Understanding the systematics in this method is the focus of this thesis. This approach involves constructing a model velocity field based on the density field and comparing it with peculiar velocity measurements at the locations of galaxies. By doing so, we can directly estimate the parameter $\beta = f/b$, described in Section 2.1.2. The value obtained for β depends on the tracer used for the density field. The predicted velocities are dependent on cosmological parameters, allowing for constraints on the combination of $f\sigma_8$ by comparing them with observed velocities. This method has a rich history in constraining cosmological parameters, as demonstrated in studies such as Kaiser et al. (1991); Hudson (1994); Branchini et al. (1999); Pike & Hudson (2005). Recent results showcasing $f\sigma_8$ constraints (and data used to set them) obtained through this technique are Turnbull et al. 0.40 ± 0.07 (PSCz + A1; 2012) , Carrick et al. 0.401 ± 0.024 (2M++ + SFI++/A1; 2015), Nusser 0.40 ± 0.08 (2MRS + CF3; 2017) , Boruah et al. 0.400 ± 0.017 (2MTF/2M++ + SFI++/A2; 2020) , Said et al. 0.338 ± 0.027 (2M++ + 6dFGSv/SDSS; 2020) , Lilow & Nusser 0.367 ± 0.060 (2MRS + CF3; 2021). Figure 2.4 shows a summary of the values presented in this section.

2.5 Organisation of This Thesis

Chapters 1 and 2 have provided an introduction to the key ideas and concepts that will be explored in later chapters. I have provided an overview of ΛCDM and the cosmological parameters that can be constrained using peculiar velocities. In particular, I have focused on the methodology and observables necessary to predict peculiar velocities from an underlying density field.

Understanding the systematics introduced into peculiar velocities due to survey limitations is crucial for several reasons. Firstly, peculiar velocities play a significant role in distinguishing and testing different cosmological models, particularly when it comes to fluctuations on large scales where the effects of modified gravity become apparent. Secondly, peculiar velocity measurements provide valuable insights into matter distributions at low redshifts where other observational techniques may be limited or less accurate. And most importantly for assessing the errors on $f\sigma_8$ which can provide valuable insights into the S_8 tension with Planck measurements.

By accurately quantifying and accounting for survey limitations that may introduce biases or uncertainties into cosmological measurements, we can ensure that our interpretations of data are reliable. The systematic biases explored are investigated in Chapters 3–4 to infer the recovered cosmological parameters and the overall impact.

Chapter 3 presents the first work of my Ph.D., which explores the accuracy to which velocity-density comparisons are able to recover cosmological parameters, using large cosmological N-Body simulations. We examine various technical aspects individually rather than simultaneously allowing for an understanding of how each systematic contributes to the overall uncertainty. In this chapter, we investigate how the smoothing length, choice of density field tracers, noise in halo mass estimates or stellar-to-halo mass relation, and finite survey volumes impact our predictions.

Chapter 4 presents the second work of my Ph.D., which studied in greater detail some of the effects in Chapter 3, by investigating the extent to which our predictions are affected when using realistic mock galaxy surveys mimicking the 2M++ compilation. Here we explore the impact of survey selection effects, such as flux-limited samples and obscuration due to the Galactic plane, on estimating cosmological parameters through velocity-density comparisons. We present how the measured biases propagate into previous measurements of $f\sigma_8$

In Chapter 5 we use the mock catalogues generated in Chapter 4 to quantify the amount of uncertainty that propagates into the Hubble parameter. We solely analyse the impact due to the imperfect reconstruction of the cosmological redshift by peculiar velocities, and place a lower bound on the uncertainty in the local Hubble parameter due to redshift reconstruction.

Finally Chapter 6 provides a summary of these projects, as well as a discussion of areas for future work and the outlook of several upcoming surveys.

Chapter 3

Quantifying Biases in Estimated Cosmological Parameters from Velocity-Density Comparisons Using Simulations

The goal of this chapter is to assess the accuracy and precision of the velocity-density comparison method in the measurement of the cosmological parameters β *and* σ_8*. And the degree to which this method is biased using a combination of these parameters we define as* ζ^**, which is unbiased if equal to unity. We perform this analysis using N-Body simulations and SAMs as a proxy for real galaxies. In this chapter we examine several technical aspects that can affect the accuracy of this method in real surveys, such as choice of smoothing kernel, choice of tracers, noise in mass estimates, and survey volume effects. We aim to quantify any systematic biases, as previous studies have not taken into account the additional scatter caused by the combined effects of randomness in the galaxy-mass relation and the cosmic variance effect resulting from limited survey volumes.*

3.1 Introduction

Peculiar velocities are the only practical way of measuring the underlying distribution of dark matter (DM) on large scales (Willick et al., 1997) in the nearby (low redshift) Universe. Specifically, they can be used to measure the cosmological parameter combination $f(\Omega_m)\sigma_8$, where the first term is the logarithmic growth rate of fluctuations, with $f(\Omega_m) = \Omega_m^{0.55}$ in the Lambda Cold Dark Matter (ΛCDM) model, and σ_8 is the root mean square matter density fluctuation in a sphere of radius 8 h^{-1} Mpc. Although peculiar velocities have been used for similar purposes since the early 90s (see reviews by Dekel (1994) and Strauss & Willick (1995)), there has been a recent revival of interest in measuring $f\sigma_8$ Pike & Hudson (2005); Davis et al. (2011); Turnbull et al. (2012); Hudson & Turnbull (2012); Carrick et al. (2015); Huterer et al. (2017); Dupuy et al. (2019); Qin et al. (2019); Adams & Blake (2020); Said et al. (2020); Boruah et al. (2020).

The use of peculiar velocities as a probe of $f\sigma_8$ has taken on renewed importance in light of the 3.2σ conflict between Cosmic Microwave Background (Planck Collaboration et al., 2020b) and weak lensing measurements (Asgari et al., 2020) of the parameter combination $S_8 \equiv \Omega_m^{0.5}\sigma_8$, with the latter giving lower values. This combination is very similar to $f\sigma_8$, differing by only 0.05 in the exponent of Ω_m. As shown by Boruah et al. (2020), some recent peculiar velocity measurements also yield lower values of S_8 than Planck (as do most other probes of this parameter combination).

One method for measuring $f\sigma_8$ involves regressing the observed peculiar velocities (from e.g. supernovae, Tully-Fisher or Fundamental Plane standard candles/rulers) on their predicted peculiar velocities from the density field of galaxies, obtained from a redshift survey. Specifically, the slope of this regression, β_g, is then combined with a measurement of the fluctuations of galaxies, $\sigma_{8,g}$ to yield an estimate of

$$f\sigma_8 = \beta_g \sigma_{8,g}\,, \tag{3.1}$$

as first suggested by Pike & Hudson (2005). The background theory and assumptions implicit in this method are discussed in more detail in Section 3.2 below.

The goal of this chapter is to test the accuracy and precision of this method using large cosmological N-Body simulations at a redshift of zero of DM halos as a proxy for galaxies, as well as semi-analytical models of galaxy formation. Our approach is not to simulate all the observational properties of the surveys simultaneously (as in, for example, Nusser et al. (2014)), but rather to consider one by one the different physical effects which may bias or add uncertainty to our results. In this sense the chapter is similar in spirit to Berlind et al. (2000).

This chapter is organised as follows. Section 3.2 describes the theoretical framework of the relationship between peculiar velocities and the density fluctuation field from linear perturbation theory, and the relevant cosmological parameters. Section 3.3 presents the simulation data and semi-analytic models that are used for the analyses performed in this chapter. Section 3.4 describes the prescription for how we predict peculiar velocities. In section 3.5 we investigate how the choice of smoothing kernel impacts our estimates of β/f and the amount of scatter generated in velocity – density cross-correlations. Section 3.6 investigates how uncertainties corresponding to 0.1 and 0.2 dex in halo mass measurements influence the predictions of β/f and $\sigma_{8,\mathrm{h}}$. In section 3.7 we instead explore how using either the stellar to halo mass relation or galaxy observables to weight the density field impacts these cosmological estimates. Section 3.8 focuses on how these estimates are affected by volume limited surveys. Finally, Section 3.9 presents our conclusions.

3.2 Peculiar Velocities from Linear Perturbation Theory

In linear perturbation theory, it is possible to relate the density field to the peculiar velocities of the galaxies at low redshift using Eqn. 2.15. This calculation is only valid in the linear regime, where $\delta \lesssim 1$, allowing higher order terms to be ignored (Peebles, 1993). For example, it does not predict the transverse components of a galaxy within a galaxy group. In ΛCDM, the rms matter density in spheres increases with decreasing sphere radius, so we expect linear theory to break down on small scales. In practice then, to apply Eqn. 3.2 one needs to smooth $\delta(r)$.

In the linear regime, the density modes in Fourier space grow independently of one another. As a result it is easier to write Eqn. 2.15 in Fourier space as follows

$$\boldsymbol{v}_{\boldsymbol{k}} = iH_0 f \frac{\boldsymbol{k}}{|\boldsymbol{k}|^2}\delta_k\,, \tag{3.2}$$

where H is the Hubble constant ($H = 100\,h\,\mathrm{km\,s^{-1}Mpc^{-1}}$). The smoothing is also simpler in Fourier space, because a convolution is a multiplication in Fourier space.

The density fluctuation field used in the previous equations is that of the underlying matter density field. Because it is dominated by dark matter, this cannot be measured empirically. Instead, an assumption must be made as to how the observed galaxies trace the underlying total matter. If one assumes linear biasing, the relation is

$$\delta_g = b_g\delta, \tag{3.3}$$

where b_g is the linear bias and δ_g is the density fluctuation field of the *galaxies*. Under this assumption, at $z = 0$, Eqn. 4.1 can be written as

$$v(\boldsymbol{r}) = \frac{H_0 f(\Omega_m)}{4\pi b_g}\int \delta_g(\boldsymbol{r}')\frac{(\boldsymbol{r}'-\boldsymbol{r})}{|\boldsymbol{r}'-\boldsymbol{r}|^3}d^3\boldsymbol{r}'. \tag{3.4}$$

Note that if we express distances $\boldsymbol{r}$ in units of h^{-1} Mpc (or km/s), as are naturally obtained from redshift surveys, then one must set $H = 100\,\mathrm{km\,s^{-1}Mpc^{-1}}$ (or 1, respectively) in the above expression. Thus when applying this equation to density fields derived from redshift surveys, the predictions are independent of the true value of H. The other two values outside the integral can be compacted into the parameter combination

$$\beta_g \equiv \frac{f}{b_g}\,. \tag{3.5}$$

If linear biasing holds, then $\sigma_{8,g} = b_g\sigma_8$. Putting this into Eqn. 3.5, we find that the product of the observables to be $\beta_g\sigma_{8,g}$, as in Eqn. 3.1, and so we can set constraints on cosmological parameters.

In reality, the assumptions of linearity, both in the context of perturbation theory and in the context of biasing, will not hold exactly. Fortunately, peculiar velocities are primarily generated by large scale waves, where linearity will be a good approximation. Nevertheless, they also have a contribution from smaller, less linear scales. For these reasons, simulations are needed to calibrate any biases arising from non-linearities.

3.3 Simulation Data

We use two publicly available simulations: Bolshoi and MultiDark Planck 2 (MDPL2) (Klypin et al., 2011, 2016), along with two simulated semi-analytic catalogues, SAG (Cora et al., 2018) and SAGE (Croton et al., 2016) which populate the DM haloes of MDPL2. We use the snapshots at $z = 0$. The halo and galaxy catalogues were obtained from the COSMOSIM database [1].

The high-resolution Bolshoi simulation (Klypin et al., 2011) follows 2048^3 particles in a comoving, periodic cube of length 250 h^{-1} Mpc from $z = 80$ to today. It has a mass and force resolution of $1.35 \times 10^8 h^{-1} M_\odot$ and 1 h^{-1} kpc respectively, and the DM haloes range from the masses of Milky Way satellites ($10^{10}M$) to the largest of clusters ($10^{15}M$). It was run as a collisionless DM simulation with the Adaptive Refinement Tree Code (ART; Kravtsov et al. (1997)) and assumes a flat, WMAP5 cosmology with parameters $\Omega_m = 0.27$, $\Omega_\Lambda = 0.73$, $h = 0.7$, (linear) $\sigma_8 = 0.82$ and $n_s = 0.95$. Haloes in Bolshoi were identified using Rockstar (Behroozi et al., 2012). The (non-linear) $\sigma_{8,m}$, measured from the particles is 0.897.

---

[1] `www.cosmosim.org`

The MultiDark project consists of a suite of cosmological hydrodynamical simulations (Klypin et al., 2016), all assume a flat ΛCDM cosmology with cosmological parameters: $\Omega_M = 0.307115$, $\Omega_\Lambda = 0.692885$, $h = 0.6777$, linear $\sigma_8 = 0.8228$, and $n_s = 0.96$, which is consistent with Planck results (Planck Collaboration et al., 2020b). We focus on the MDPL2 simulation which has a periodic box of length 1000 h^{-1} Mpc evolved from a redshift of 120 to 0 with a varying physical force resolution level from 13-5 h^{-1} kpc and various implemented physics. The simulation uses 3840^3 dark matter particles of mass $1.51 \times 10^9\ h^{-1}\mathrm{M}_\odot$, and has identified more that 10^8 haloes using Rockstar (Behroozi et al., 2012), with merger trees that were generated using ConsistentTrees (Behroozi et al., 2013). The (non-linear) $\sigma_{8,m}$, measured from the particles is 0.925[2].

The SAG (Cora et al., 2018) and SAGE (Croton et al., 2016) semi-analytic models include the most relevant physical processes in galaxy formation and evolution, such as radiative cooling, star formation, chemical enrichment, supernova feedback and winds, disc instabilities, starbursts, and galaxy mergers. These model were calibrated to generate galaxy catalogues using the MDPL2 simulation. A comprehensive review of the models can be found in Knebe et al. (2018).

3.4 Testing Methods with N-Body Simulations

Our goal is to test Eqn. 3.4 using data from N-body simulations. Specifically, we will calculate the predicted peculiar velocities by integrating over a smoothed density tracer field, denoted by the subscript "t", used in place of $\delta_g(\boldsymbol{r})$ in the integral,

$$\boldsymbol{v}_{\mathrm{pred}}(\boldsymbol{r}) = \frac{H_0}{4\pi} \int \delta_t(\boldsymbol{r}') \frac{(\boldsymbol{r}' - \boldsymbol{r})}{|\boldsymbol{r}' - \boldsymbol{r}|^3} d^3\boldsymbol{r}' \,, \tag{3.6}$$

and compare this to the "observed" (unsmoothed) velocity tracers, which are used in place of $\boldsymbol{v}(\boldsymbol{r})$ on the left hand side of Eqn. 3.4. Note that Eqn. 3.6 omits the β_t term, which we fit to the N-body data by performing a linear regression

$$\boldsymbol{v}_t = \beta_t \boldsymbol{v}_{\mathrm{pred}} \,, \tag{3.7}$$

---

[2] For reasons of computational efficiency, the value of $\sigma_{8,\mathrm{m}} = 0.95$ used in the published version of this chapter, was calculated using particle counts in small (~ 1 Mpc) voxels that were themselves within an 8 h^{-1}Mpc radius sphere. A careful calculation shows that the actual volume of the voxels corresponds to that of a sphere of radius 7.77 h^{-1}Mpc. This generates no impact on our results as our measurements of ζ^* are with regard to the ratio of $\sigma_{8,g}/\sigma_8, m$, which have the same volume.

where $\boldsymbol{v}_t$ is the measured N-body velocity of a tracer of the velocity field which, in principle, need not be the tracer as used for the density field). This is a cross-correlation between two samples, and we will refer to it generically as a velocity – density cross-correlation, although the actual comparison is made between observed and predicted peculiar velocities.

The procedure used to obtain the density tracer field is the same regardless of whether the tracer data are particles, DM haloes or galaxies, as each simulation provides Cartesian positions and velocities for all tracers. The latter two also provide additional information such as halo mass, stellar mass and luminosity measurements in different filter bands. In this chapter, we will construct the density fluctuation field using all of the aforementioned tracers. In the following section however, we will focus solely on using the particles for the density field.

Likewise, one also has a choice of which velocity tracers to use in the comparison. Using the particles as the velocity tracers is the most straightforward, so we will begin with this case in Section 3.5.1 below. Generally, however observers usually combine the peculiar velocities from multiple galaxies in the same group or cluster to obtain the mean peculiar velocity of the group. The N-body analogue for the group-averaged peculiar velocity is the peculiar velocity of the host (or central) halo.

In order to calculate the density field, the density tracers are placed on a 3D cubic grid at the nearest grid point and the contribution of all tracers at the same grid point is summed.

In the case where grid spacing is non-negligible, the gridding acts like smoothing, and it adds in quadrature with the applied to yield a total effective smoothing (Boruah et al., 2020),

$$\sigma^2_{\text{total}} = \sigma^2_{\text{grid}} + \sigma^2_{\text{smooth}}, \tag{3.8}$$

where $\sigma^2_{\text{grid}} = \frac{\Delta^2_{\text{grid}}}{12}$ where Δ_{grid} is the grid spacing in h^{-1}Mpc.

Using a fine grid allows us to preserve some of the detail and ignore the effects of grid size smoothing. All comparisons in this chapter are done assuming a grid spacing of 0.36 and 0.98 h^{-1}Mpc for Bolshoi and MDPL2 respectively, which produces a negligible effect on the effective smoothing scales that will be used in this chapter.

We choose to smooth the density fluctuation field using a Gaussian smoothing kernel, which, in configuration and Fourier space, are given by

$$W(r) = \frac{1}{\sqrt{2\pi}R_G} \exp\left(\frac{-r^2}{2R_G^2}\right) \tag{3.9}$$

$$W(k) = \exp\left(\frac{-k^2 R_G^2}{2}\right), \tag{3.10}$$

respectively. We then calculate the peculiar velocities on the 3D grid using Eqn. 3.2. To predict the peculiar velocity of a given velocity tracer, we linearly interpolate from the velocity grid to the tracer's location.

As discussed above, we then regress the tracer velocity against its predicted velocity, with the intercept fixed to zero, and where the fitted slope gives an estimate for β_t. The fits also yield the rms (1D) velocity scatter, σ_v, of the difference between the N-body velocities and the linear theory predictions at the best fit β_t.

3.5 The Effect of Smoothing Length on the Estimated Cosmological Parameters

As discussed above, the density tracer field must be smoothed in order to predict the peculiar velocities in linear perturbation theory. In this section, we assess the impact of different Gaussian smoothing lengths on the recovered value of β_t, and the 1D σ_v around the linear theory predictions. We focus on smoothing scales between 1-6 h^{-1} Mpc.

Specifically, we aim to confirm at what smoothing length the slope of linear regression is unbiased, which previous work has suggested lies in the range $4 - 5$ h^{-1} Mpc (Carrick et al., 2015). We first consider particles as tracers of the density field, and then consider haloes.

3.5.1 Particle-Weighted Density Fluctuation Field

We now consider the case in which we predict the peculiar velocities of particles using the particle density fluctuation field. The values of the best-fit slope divided by the value of f in the simulation, i.e. β/f, as a function of smoothing scale, are shown in Figure 3.1. This quantity should be unity if the method is unbiased. We find that predictions are unbiased for a Gaussian smoothing kernel R_G between 4 and 5 h^{-1}Mpc. Of the two simulations, MDPL2 should be more accurate since its minimum wavenumber k is $2\pi \times 10^{-3} h/\mathrm{Mpc}$, and whereas that of Bolshoi is a factor 4 larger due to its smaller box length. Thus Bolshoi fails to capture the long-wavelength modes that generate a significant fraction of the rms peculiar velocity. The 1D σ_v around the best fit slope, however, is minimized at a smoothing length that is 1-1.5 h^{-1} Mpc smaller. The σ_v of particle peculiar velocities is high: between 225 and 275 km/s. This is because the particle's peculiar velocity includes its motion within the halo as well as the peculiar velocity of the halo itself. Only the latter is well-predicted by linear perturbation theory.

If we predict the peculiar velocities of host (or central) haloes (i.e. excluding subhaloes) using the particle density field, we find similar results, with unbiased results and minimum σ_v occurring for Gaussian smoothing lengths that are $\sim 0.5h^{-1}$Mpc smaller than when using particles as velocity tracers. The σ_v as a function of smoothing length is quite flat; it is not much higher at the fiducial 4 h^{-1} Mpc. However the amplitude of σ_v for host haloes is significantly lower (~ 150 km/s) than for particles (~ 250 km/s), as expected given that the velocities of the particles include their motion with respect to the host halo.

Finally, it is interesting to explore the question of whether haloes of different masses have different velocities relative to the predictions of linear theory, one scenario of "velocity bias." We find that imposing a minimum mass threshold on the haloes used to sample the velocity field of 10^{12} $\mathrm{M}_\odot$ has little effect on the measured β/f for smoothing lengths greater that 1.5 h^{-1}Mpc for MDPL2 and 3 h^{-1}Mpc for Bolshoi, as shown in Figure 3.2. This is also true for a minimum mass of $10^{13}\mathrm{M}_\odot$. A small velocity bias appears only when considering cluster mass haloes ($> 10^{14}\mathrm{M}_\odot$) as peculiar velocity tracers. For clusters, there is also an increase in the 1D σ_v with respect to the linear theory predictions.

3.5.2 Halo Mass-Weighted Density field

We now consider a scenario that is closer to the observational one, where the density field is provided by DM haloes, weighted by their mass. Whereas the particle density field is unbiased, this field will be biased. Therefore, we no longer expect $\beta_\mathrm{h}/f = 1$. As discussed above, in the linear regime, this bias can be calculated by measuring the rms density fluctuations of the halo-weighted density field in 8 h^{-1} Mpc spheres. The halo and particle σ_8 measurements are related by

$$b_\mathrm{h} = \frac{\sigma_{8,\mathrm{h}}}{\sigma_{8,\mathrm{m}}} \tag{3.11}$$

which is the same b in the β term defined previously. We measure β/f from the slope of linear regression as before, but multiplying this by the correction factor b_h. This should return a value of unity if the method unbiased. This parameter combination will be referred to as

$$\zeta^* = \frac{\beta}{f}\frac{\sigma_{8,\mathrm{h}}}{\sigma_{8,\mathrm{m}}}. \tag{3.12}$$

To measure σ_8 we placing non-overlapping spheres of 8 h^{-1}Mpc covering the entire the density field, and measure the standard deviation in the values. Doing this, we find values of $\sigma_{8\mathrm{h}} = 1.45 \pm 0.04$ and 1.57 ± 0.02 for the halo masses for Bolshoi and MDPL2

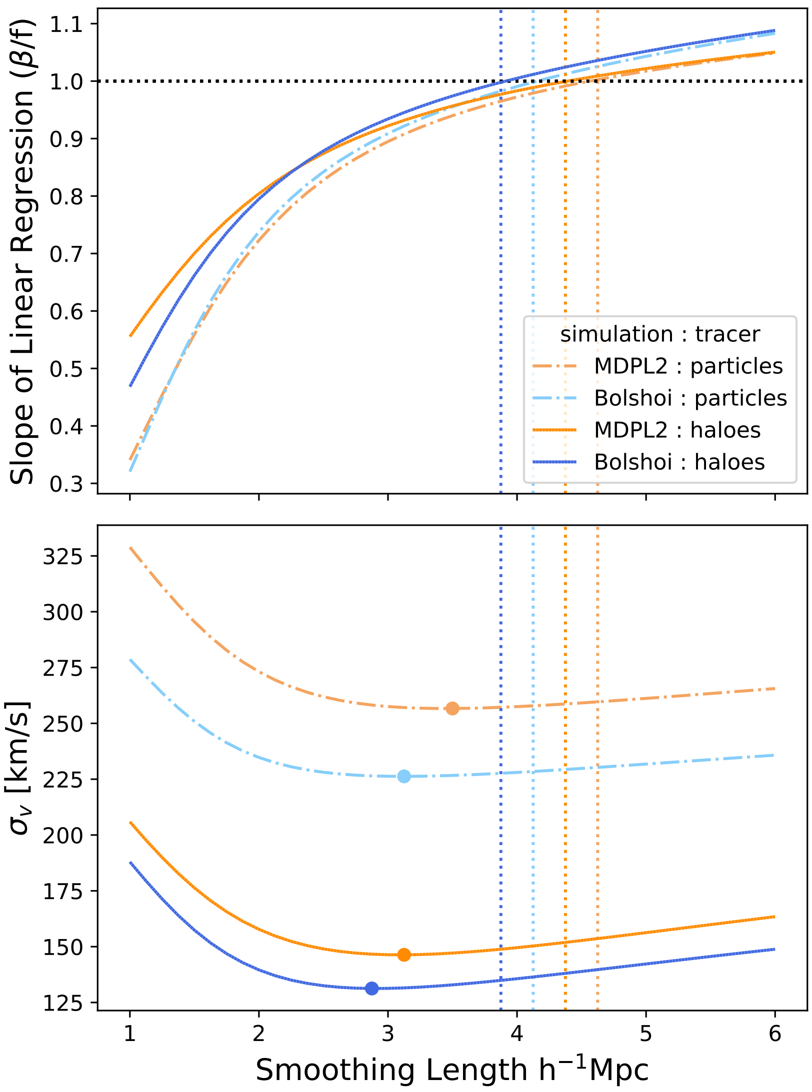

Figure 3.1: Top Panel: Slope of linear regression for the predicted and N-Body particle and central halo velocities (excluding subhaloes) for MDPL2 and Bolshoi simulations. Because we correct for the f parameter, a value of β/f of unity indicates for the smoothing length for which the velocity–density cross-correlation is unbiased. The predicted velocities were calculated assuming an underlying *particle* density field and linear theory for the Gaussian smoothing radius shown on the horizontal axis. Bottom Panel: The scatter between the measured N-body and predicted peculiar velocity associated with each of the linear regression slopes. A circle has been placed at the smoothing length where the standard deviation was minimized.

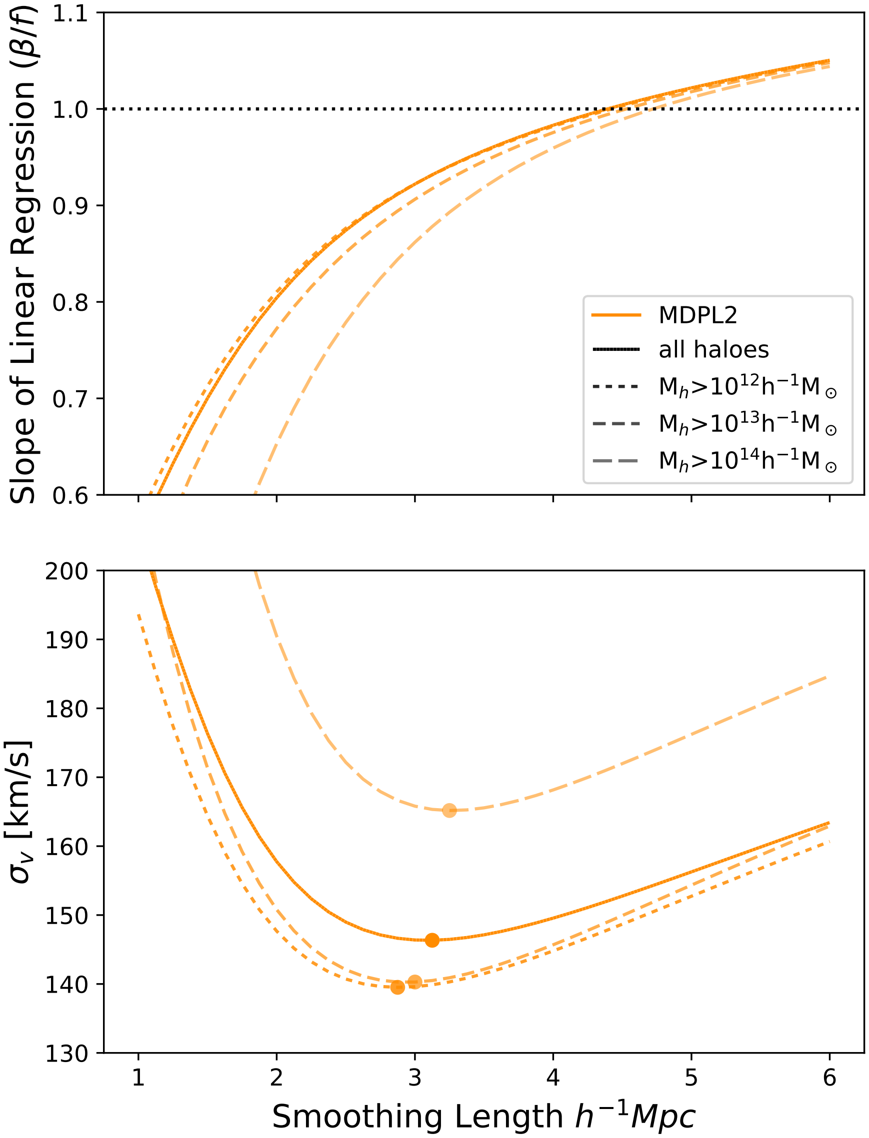

Figure 3.2: As in Figure 3.1 where again the predicted peculiar velocities are based on the particle density field, but here these are compared to the N-body peculiar velocities of *haloes* (but excluding subhaloes). For clarity the solid line labelled 'all halos' represents all simulation objects classified as centrals, while the dashed lines represent centrals with masses greater than various minimum masses as indicated in the legend.

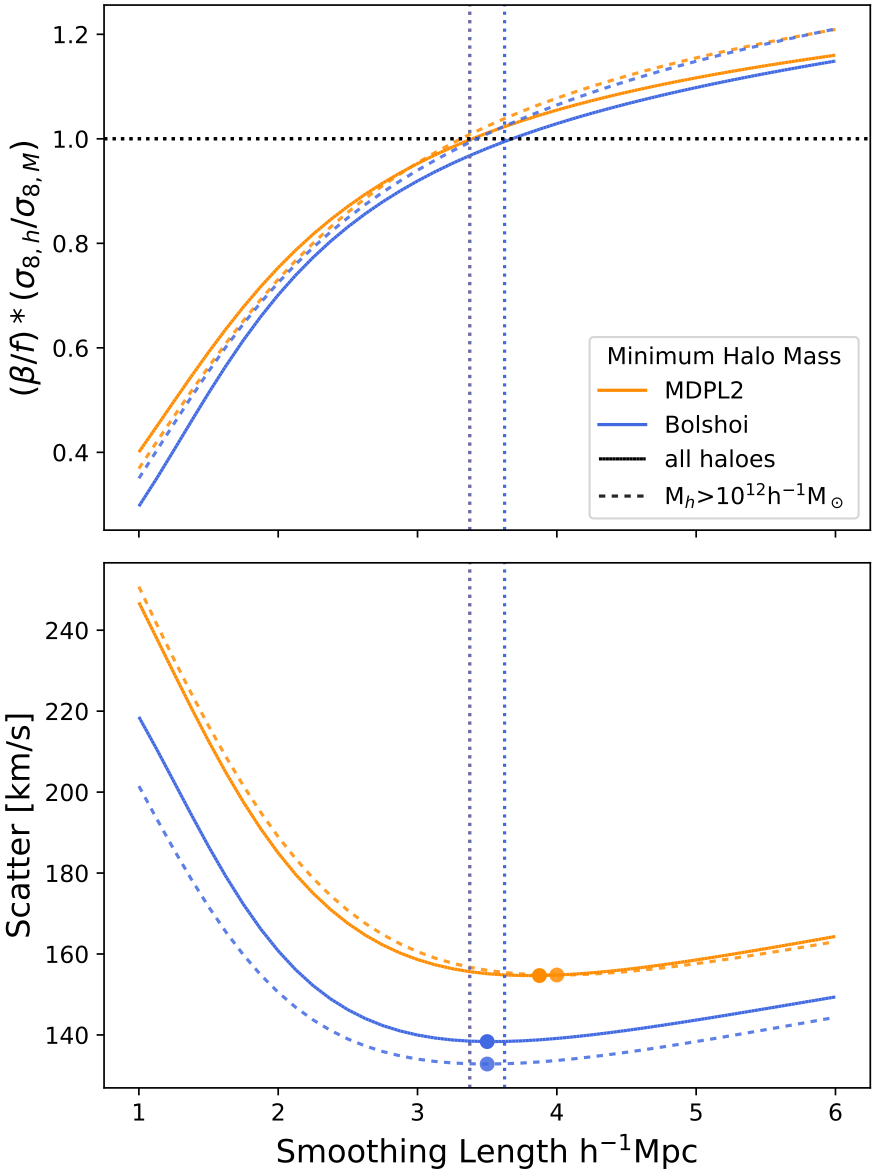

Figure 3.3: Similar to Figure 3.2, except here the mass-weighted halo density field is used to predict peculiar velocities of haloes. The vertical axis in the top panel is now $\beta/f(\sigma_{8,h}/\sigma_{8,m})$.

respectively, much larger than $\sigma_{8,\mathrm{m}}$, which is the measured (non-linear) σ_8 of the particle density field.

The fitted values of β_h/f, however, are lower than unity, as expected. The results for ζ^* are plotted in Figure 3.3, showing that the mass-weighted determination is nearly unbiased: at the fiducial $R_G = 4h^{-1}$ Mpc, the MDPL2 field has $\zeta^* = 1.05$, whereas for Bolshoi $\zeta^* = 1.02$. This suggests that linear biasing correction works well, even for fields with $b_\mathrm{h} \sim 1.7$. The 1D σ_v (~ 160 km/s) is only marginally higher than when particles were used for the density field.

3.5.3 Discussion: Cross-Correlation and Optimal Smoothing

It is not obvious why a Gaussian smoothing, with $R_G \sim 3 - 4\ h^{-1}$ Mpc, should be the "correct" smoothing length. We can gain some insight by considering the problem in Fourier space, specifically Eqn. 3.2 which relates the velocity modes to the density modes in linear perturbation theory. This should be exact on large scales, but we expect it to break down at high k.

For simplicity, first assume that all Fourier modes are Gaussian and independent and that at a given k the joint distribution of velocity and density mode amplitudes is given by a bivariate Gaussian. We expect the correlation coefficient, ρ, to approach 1 on large scales and zero at high k. Generally if one has a bivariate normal distribution of two variables x and y, and one regresses y on x the slope of the relation is $\rho\frac{\sigma_y}{\sigma_x}$, or since the covariance $C_{xy} = \rho\sigma_x\sigma_y$, the slope can also be written C_{xy}/σ_x^2. Therefore, the predicted velocity mode amplitude is given by the density mode amplitude times the slope $C_{v\delta}/\sigma_\delta^2$.

The quantities $C_{v\delta}$ and σ_δ^2 can be measured in N-body simulations as a function of wavenumber k. The latter is just the power spectrum of matter density fluctuations, $P_{\delta\delta}$, but the covariance is less well studied. Zheng et al. (2013) have measured the cross-spectrum of the closely related quantity $\theta = \nabla \cdot v$ with the density δ, and its ratio with the density power spectrum. They define the normalised window function

$$\widetilde{W}_k = \frac{1}{f}\frac{P_{\theta\delta}}{P_{\delta\delta}}\,, \tag{3.13}$$

which has the property that it asymptotes to 1 at low k and goes to zero at higher k. This function is plotted in Figure 3.4. Also over-plotted for comparison are two Gaussian smoothing filters with $R_G = 2.88$ and $4.0h^{-1}$ Mpc. The estimated β/f from the particle weighted density field smoothed using either $\widetilde{W}_k$ as a k-space smoothing function or with a Gaussian kernel of $R_G = 2.88\ h^{-1}$Mpc both produce values of 0.88. There is also no significant difference in σ_v.

The Gaussian smoothing with $R_G = 4.0h^{-1}$ Mpc is a better match to $\widetilde{W}_k$ at low k.

In reality, particularly at high k, the assumption of bivariate Gaussianity will no longer be correct, so the above simple argument will break down. In principle, with detailed knowledge of the correlations, it should be possible to design the optimal k-space filter. For our purposes in this chapter, we retain the simplicity of Gaussian smoothing, and adopt a Gaussian smoothing filter with $R_G = 4\ h^{-1}$Mpc for consistency with previous work.

3.6 The Effect of Halo Mass Uncertainties

In the previous sections, the masses of the haloes were assumed to be known exactly, with no uncertainty in the measurements. However in real survey data there is a some uncertainty in the true mass of any given halo, depending on the method used to estimate it, and this may be in the range 0.1 – 0.2 dex (see Section 3.7). In this section, we explore how scattering the halo mass impacts the predictions of β/f and $\sigma_{8,h}$. This is accomplished by varying the halo masses by a lognormal Gaussian random variable with standard deviations corresponding to 0.1 and 0.2 dex, and calculating σ_8 and β for each realisation. A total of 500 realisations were performed on both the Bolshoi and MDPL2 halo catalogues.

We find that, from realisation to realisation, both the measured β and σ_8 deviate from the no-scatter values, and these deviations are anti-correlated. This can be understood as follows. In Section 3.5.3, we discussed how the slope (β) could be expressed as the ratio of the covariance between density and velocity, and the density power spectrum, $C_{v\delta}/\sigma^2_{\delta\delta}$. If noise is added to the density field, then the denominator increases, but the covariance is unaffected. Consequently, the fitted β drops. On the other hand, σ_8 increases because of the additional noise. This anti-correlation leads to some cancellation of the additional noise from realisation to realisation in the product $\zeta^* = \beta_\mathrm{h}\sigma_{8,\mathrm{h}}$.

The net result of increasing the halo mass scatter and its impact on ζ^* are shown in the top panel of Figure 3.5, with a scatter of zero dex corresponding to the case where the halo masses are precisely measured. We find that when introducing a lognormal scatter, the value of ζ^* increases only slightly with increasing scatter for both Bolshoi and MDPL2. We note however that the standard deviation of ζ^* is higher for Bolshoi due to the smaller volume of the simulation, which leads to greater variation from realisation to realisation in β_h, σ_h and their product ζ^*. For MDPL2, the net effect of scatter in the N independent

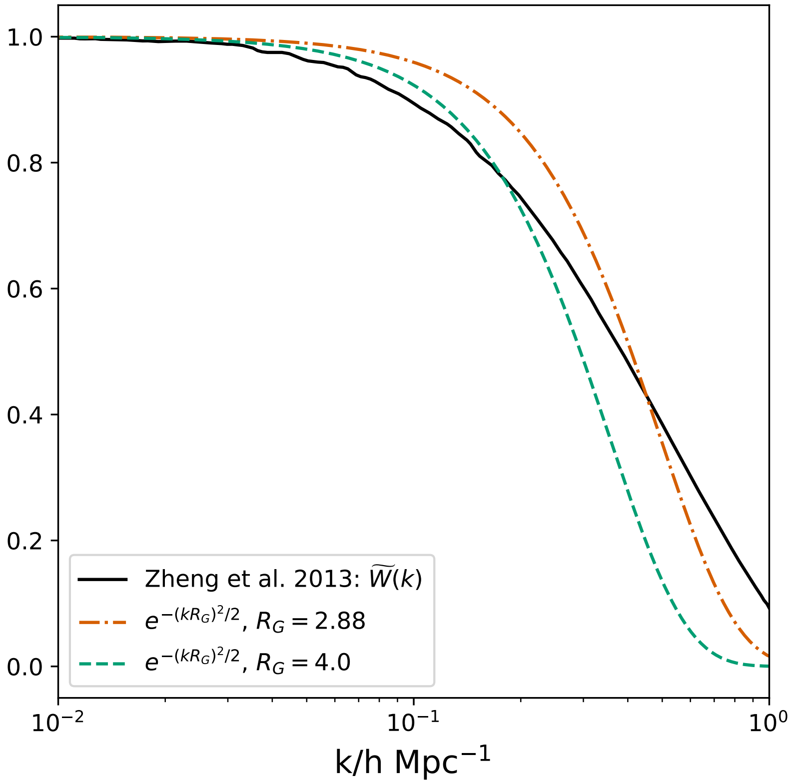

Figure 3.4: The normalised window function from Zheng et al. (2013), calculated from the J1200 simulation, based on the correlation of the velocity and density fields (see text for details) is shown, with Window functions for Gaussian smoothing kernels with scales of 2.85 and 4.0 h^{-1} Mpc. Both functions exhibit the expected characteristics of being unity as $k \to 0$ and zero as $k \to \infty$. $\widetilde{W}_k$ and the Gaussian kernel of $R_G = 2.88\ h^{-1}$ Mpc cross 0.5 near $k = 0.39$ and $0.41 h/\mathrm{Mpc}$, respectively.

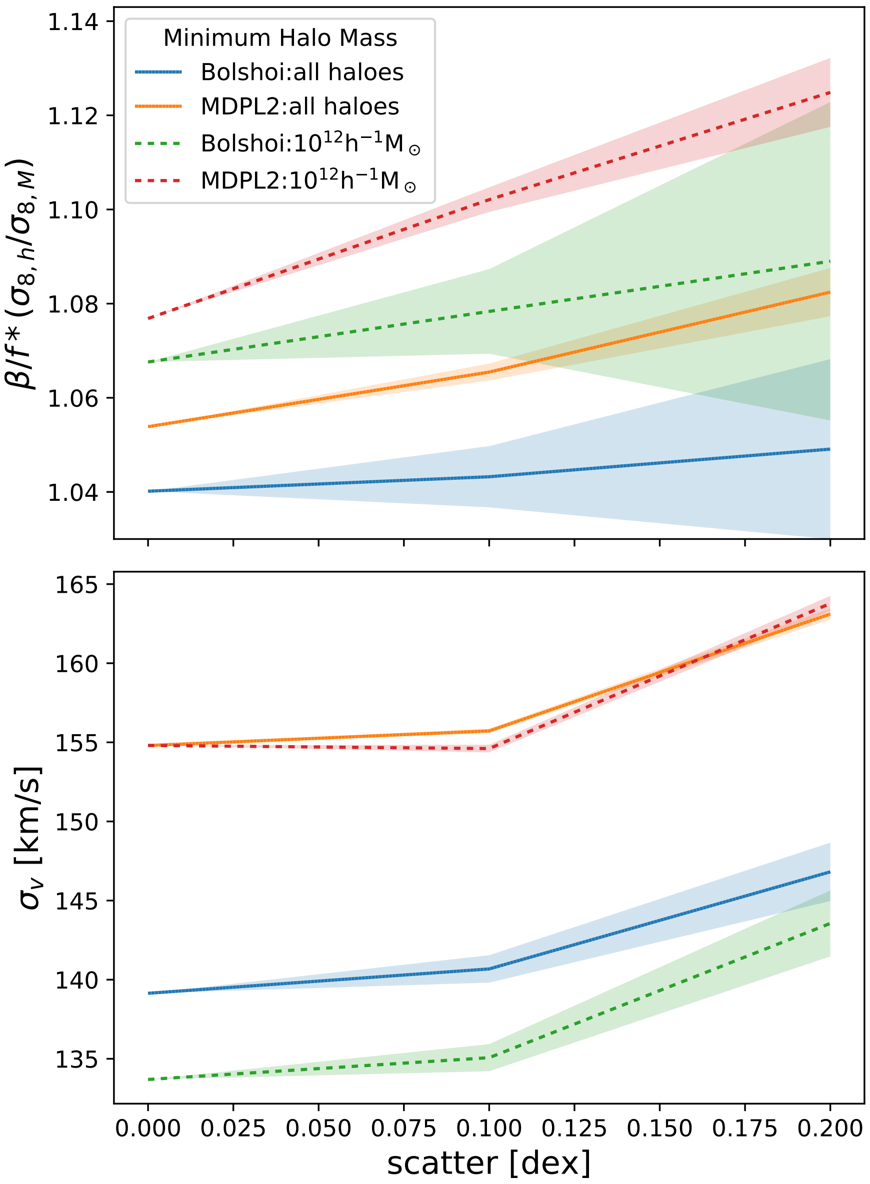

Figure 3.5: Effect of additional scatter to the mass of haloes as a function of the logarithmic scatter (0, 0.1 and 0.2 dex). For 0 dex this is the measured value of the simulation, for 0.1 and 0.2 dex a random value corresponding to a lognormal Gaussian with a σ of ~ 0.23 and 0.5 respectively, has been applied to each halo in the catalogue. Top panel: The mean (dark line) and $\pm 1\sigma$ range (shaded band) of these measurements are shown for $\beta/f(\sigma_{8,h}/\sigma_{8,m})$ at a smoothing radius of 4 h^{-1}Mpc. Bottom panel : scatter around the best fit of σ_v for the same smoothing.

halo masses is reduced by a factor $1/\sqrt{N}$ due to the larger volume containing a larger number N of haloes. This highlights the importance of the volume of the sample, a topic we shall discuss in greater detail in Section 3.8.

The bottom panel shows how the 1D σ_v is impacted by introducing stochasticity in the halo masses. We find that the 0.1 dex case generates a negligible change in the measured σ_v when compared to the original value. For halo mass uncertainties of 0.2 dex, σ_v increases, but the effect is still small, corresponding to $\sim$ 8 km/s.

3.7 Galaxies as Tracers of the Density Field

Galaxies trace the underlying dark matter distribution on large scales, but observable quantities, such as a galaxy's luminosity and stellar mass, do not necessarily have an exact relationship with the mass of the halo in which a galaxy lies. To explore how using these quantities as a proxy for mass density impact β/f and σ_8, we use two galaxy semi-analytic galaxy formation models available for the MDPL2 simulation SAG (Cora et al., 2018) and SAGE (Croton et al., 2016).

Many DM haloes host more than one galaxy, which are typically divided into centrals (the galaxy identified with the main or host DM halo) and satellites (associated with DM subhaloes). When predicting host halo mass, one can use only the stellar mass or luminosity of the central galaxy, or one can use the total stellar mass (or total luminosity) of all galaxies. We adopt the latter approach here when calculating the density fields. As before, velocity comparisons will be done solely on galaxies classified as centrals. For consistency with the previous work done in this chapter, any cuts imposed on the data will be done using the mass of the host halo.

The stellar to halo mass relation (SHMR) is different for both the SAG and SAGE semi-analytic models in MDPL2, see 3.6. SAG has a tighter SHMR with less scatter in stellar mass at a given halo mass: for haloes with masses between 10^{11} and 10^{13} $h^{-1}\mathrm{M}_{\odot}$, it has an average scatter of 0.15 dex compared to 0.39 dex in SAGE. The average SHMR is comparable for both SAG and SAGE for halo masses greater than the characteristic pivot point at $\sim 10^{12}$ $h^{-1}\mathrm{M}_{\odot}$.

3.7.1 Predictions Using Stellar-to-Halo Mass Relations

To construct a proxy mass density field, we can obtain proxy halo masses using the SHMR. The K-band luminosity is a good proxy for stellar mass, however the galaxy luminosities

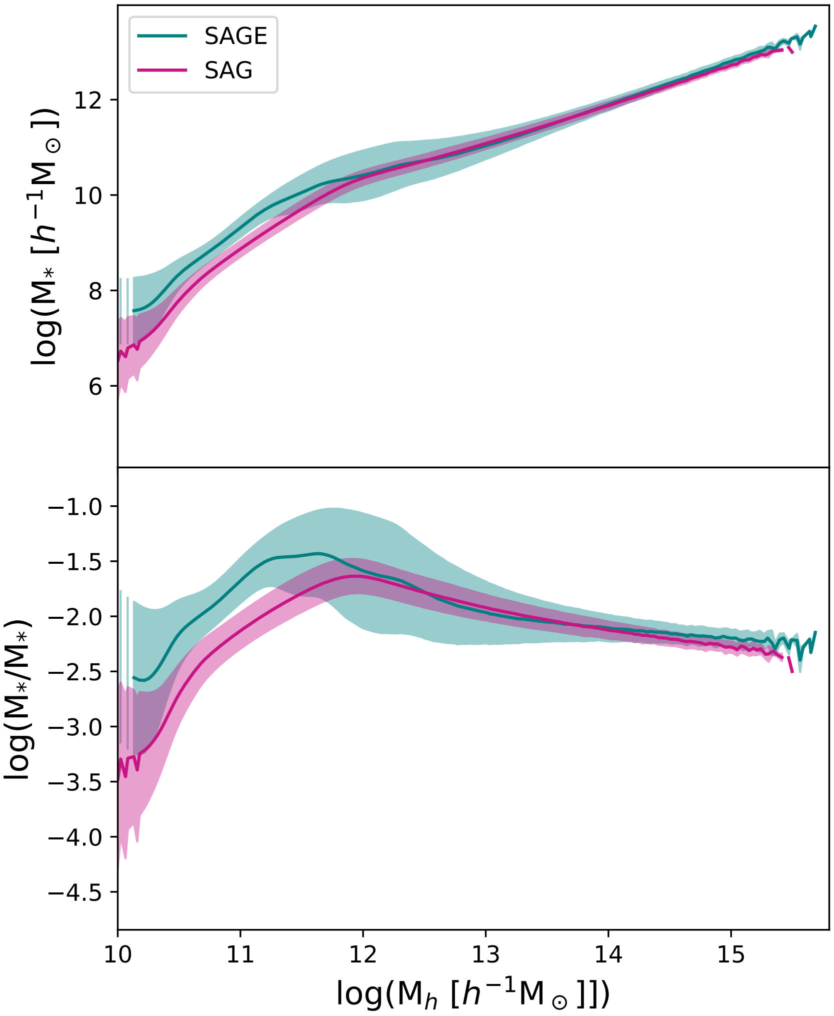

Figure 3.6: Top Panel: The stellar-to-halo mass relation (SHMR) for the total stellar mass of a halo (including stellar mass in subhaloes) as a function of total halo mass. The dark curves show the means of the SHMR and the lighter bands indicate their measured standard deviation. Both SAG and SAGE semi-analytic models are shown. Bottom Panel: the stellar to halo mass ratio as a function of halo mass.

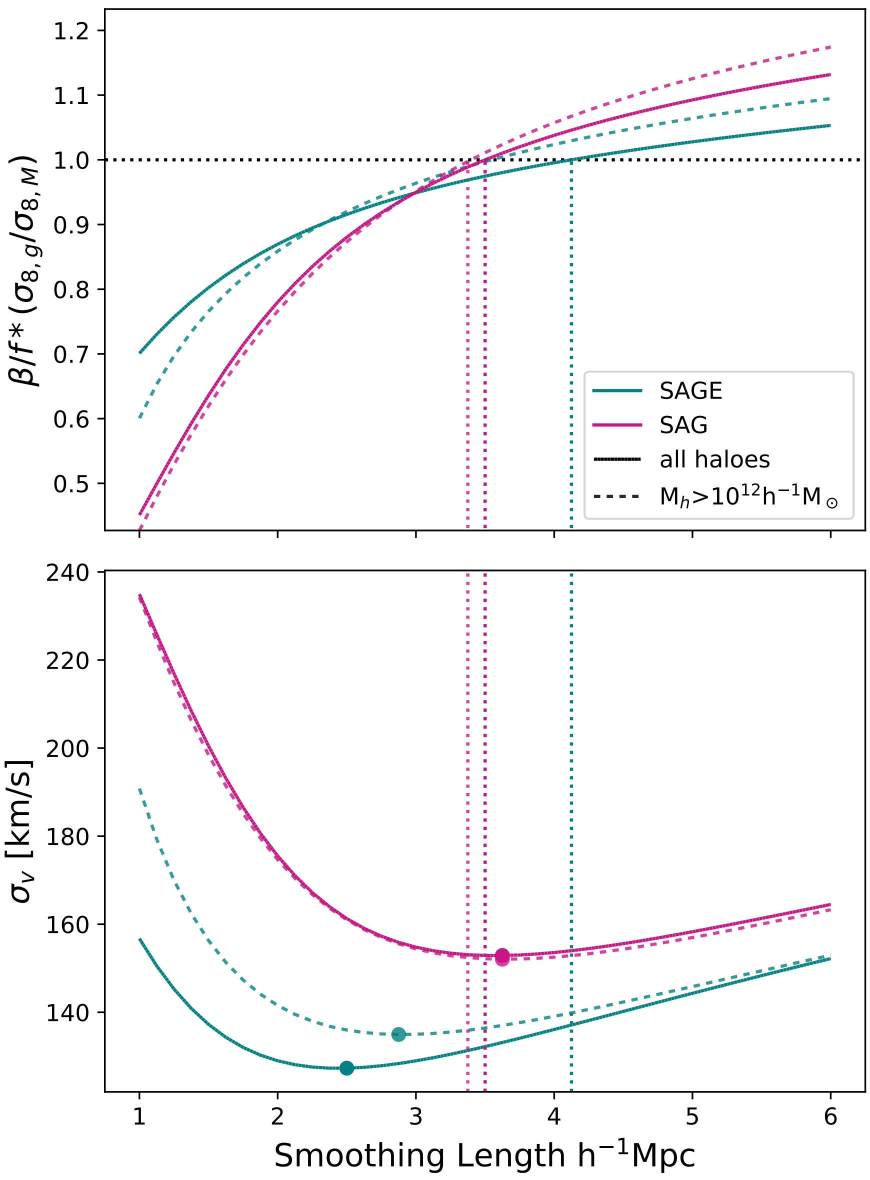

Figure 3.7: Similar to Figure 3.3, except here a fitted SHMR is used to predict the halo masses from stellar masses, and then constructing a mass-weighted halo density field to predict the peculiar velocities of central galaxies.

in SAG are limited to the u, g, r, i, z-bands. So in this section, we use the stellar masses provided for both SAG and SAGE. We fit the SHMR profiles of both SAG and SAGE semi-analytic models with a broken power law, and use these to convert the stellar masses into halo masses. Then the same analysis described in a previous section is performed. This procedure will remove the nonlinearity of the SHMR relation, but cannot remove the scatter in it, since the mean SHMR is used for each halo.

From Figure 3.7, we find for the SAGE galaxies, ζ^* is unbiased for a Gaussian smoothing of 4.1 h^{-1}Mpc but generates the lowest σ_v at $R_G = 2.6\ h^{-1}$ Mpc. For SAG these are at smoothing lengths of 3.6 and 3.5 h^{-1}Mpc, respectively. Comparing these results to Figure 3.3, we find that at $R_G = 4\ h^{-1}$Mpc, SAG produces results that are quite similar (within a few percent) to what was found using MDPL2's halo masses directly. SAGE, however, generates values of ζ^* that are 5% smaller at the same smoothing length than the haloes. We find that the generated SAG haloes produce similar estimates for the 1D scatter in velocity predictions, contrarily the SAGE haloes generate $\sim$ 20 km/s less scatter.

Comparing these results to those in the next section we note that while the halo mass does tend to be unbiased at smaller R_G the conversion of stellar to halo mass introduces 10-20 km/s of additional scatter than using galaxy observables to predicted velocities.

We attribute the results to the differences in the models' stellar to halo mass ratios as a function of halo mass. SAG has a flatter stellar to halo mass ratio than SAGE, and therefore it is close to the simple halo mass weighted case. SAGE has a steeper ratio at high halo masses, hence SAGE puts less weight on massive clusters leading to estimates of ζ^* slightly less than unity.

3.7.2 Predictions Using Galaxy Observables

A density field can also be constructed without approximating the mass of individual haloes via the SHMR. In this section, we investigate how weighting directly by the galaxy observables impacts the cosmological estimates. Such a procedure is closer to what was done by Carrick et al. (2015), who used the K-band luminosity-weighted density field from the 2M++ catalogue. Figure 3.8 shows the summary of results discussed below.

We find that, for the SAG model, weighting the density field by stellar mass produces results that yield a higher ζ^* than luminosity weighting. We can weight the density field using luminosities in any of the five bands provided by SAG. In the remainder of this chapter we focus on the r-band luminosity. We note however that the longest wavelength z-band produces the highest values of β/f however after applying the correction factor

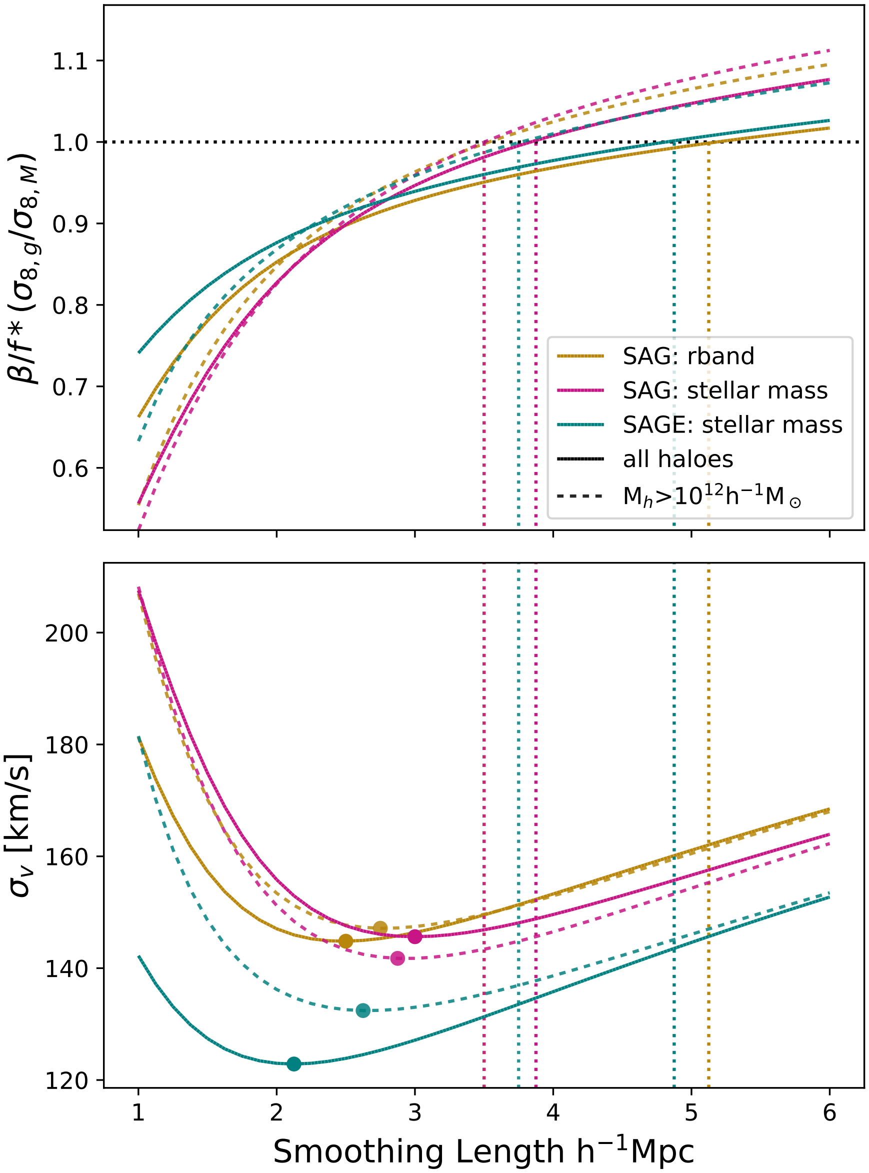

Figure 3.8: Similar to Figure 3.7 except now the density field is constructed using galaxy observables (i.e. weighted by stellar mass or luminosity) to predict and measure centrals' peculiar velocities.

Table 3.1: Summary of ζ^* values taken for $R_G = 4\ h^{-1}$Mpc for the various MDPL2 tracers which weight the density field and from which the peculiar velocities are compared.

Density Tracer	all M_t	$M_t > 10^{12} h^{-1} \mathrm{M}_\odot$	
Particles	0.97	–	Figure 3.1
Haloes	1.05	1.08	Figure 3.3
SAGE: SHMR	1.00	1.02	Figure 3.7
SAG: SHMR	1.04	1.06	Figure 3.7
SAGE: stellar mass	0.98	1.01	Figure 3.8
SAG: stellar mass	1.01	1.03	Figure 3.8
SAG: r-band luminosity	0.97	1.02	Figure 3.8

($\sigma_{8,\mathrm{g}}/\sigma_{8,\mathrm{m}}$) there is virtually no difference between bands for ζ^*, provided a low minimum mass threshold.

If the minimum mass threshold of the haloes is low, we find that weighting using the stellar masses provided by SAG closely resembles the case where the density field is halo-mass weighted and is unbiased at an $R_G \sim 3.8\ h^{-1}$ Mpc. The SAGE stellar mass and SAG r-band predict ζ^* values that are comparable at $R_G > 3\ h^{-1}$ Mpc, but only produce unbiased estimated of ζ^* for a Gaussian smoothing radius of $\sim 5\ h^{-1}$ Mpc.

In the case where a minimum mass threshold of $10^{12} h^{-1}\ \mathrm{M}_\odot$ is applied to the data, we find that ζ^* for the three cases are comparable for $3h^{-1}\mathrm{Mpc} \lesssim R_G \lesssim 4h^{-1}\mathrm{Mpc}$. With all the cases estimating unbiased ζ^* values at 3.5-3.7 h^{-1}Mpc. The σ_v is also comparable for these cases with the SAGE stellar mass producing only ∼ 10 km/s less scatter than the SAG r-band.

3.8 Finite Volume and Cosmic Variance Effects

In real data sets both the data used to obtain the density field, based on redshift surveys, and the peculiar velocity samples, cover limited volumes. This has multiple consequences. Some of these are related to sample variance: the local volume will have local values of the mean density and of σ_8 that are different from the global values. Moreover, the predicted peculiar velocities will be less accurate for galaxies close to the edge of the density field than for those far from the edges, say at the center of the volume.

In this section, we investigate these finite volume and edge effects by limiting the data, to spheres of radii with $R_{\max} = 50$, 100, 150, 200 and 300 h^{-1}Mpc, and its impact on

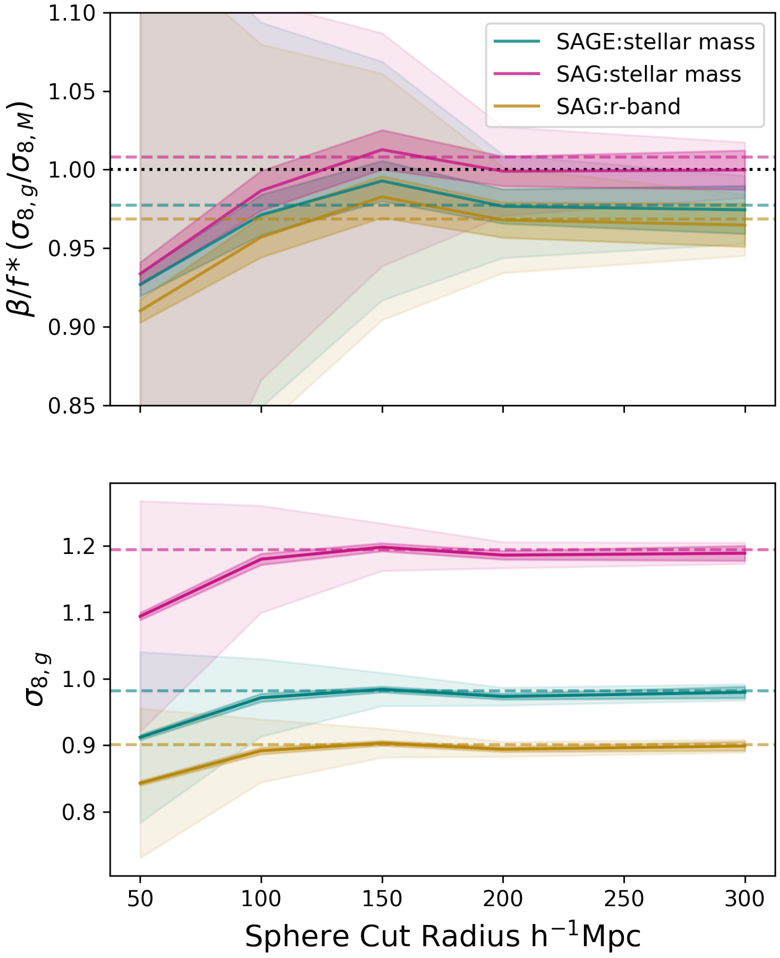

Figure 3.9: To demonstrate the dependence of our calculated parameters on the survey volume, we restrict simulation data to (non-overlapping) spheres of radius ranging from 50 to 300 h^{-1}Mpc. The components of ζ^* are calculated for each test sample assuming a Gaussian smoothing kernel of 4 h^{-1}Mpc. The upper panel and lower panel show the results for ζ^* and in σ_8 measurements, respectively, as a function of sphere radius. In both panels, the light and dark coloured bands represent the $\pm 1\sigma$ standard deviation from sphere to sphere and the standard error in the mean of the test cases (respectively) for a given sample spherical radius, with the mean being shown by the solid colour lines. The colour horizontal dashed lines show the values from the full simulation box.

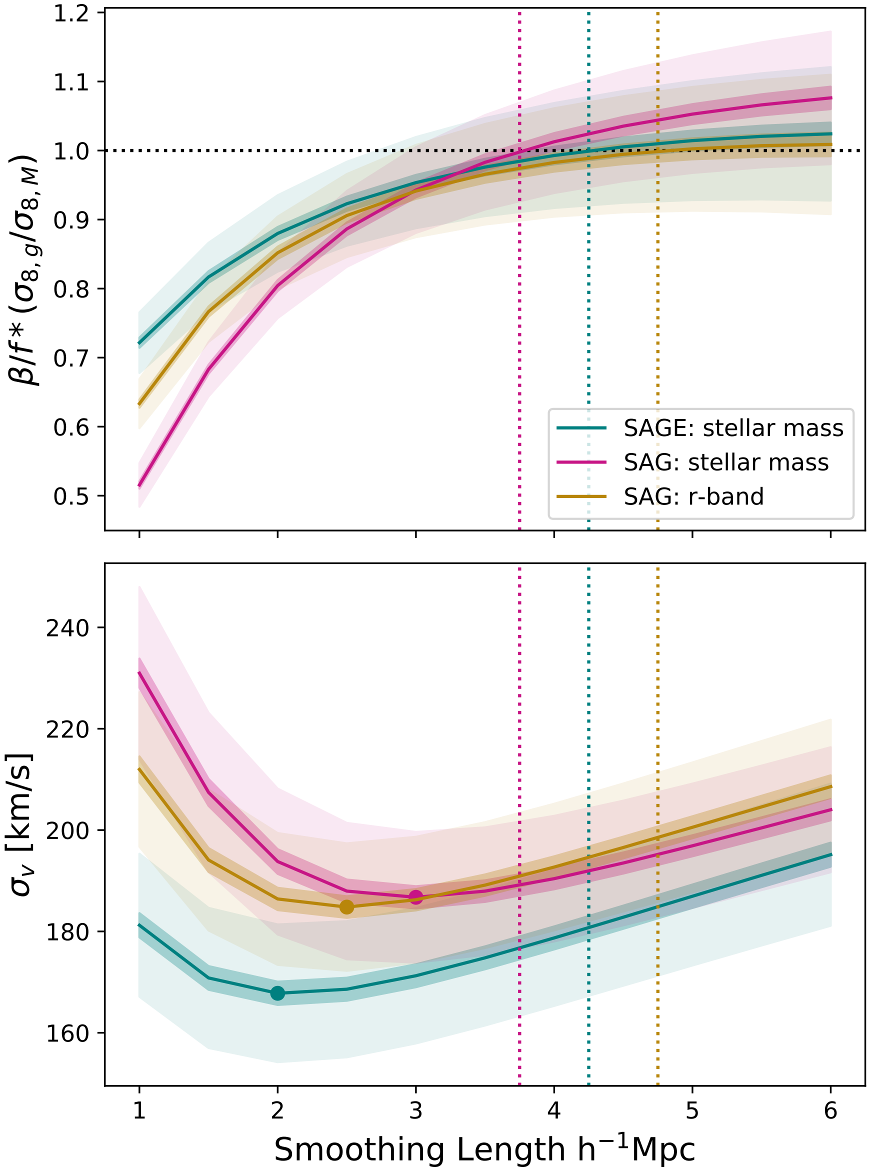

Figure 3.10: Similar to Figure 3.8 expect we now use non-overlapping sphere cuts of radius 150 h^{-1}Mpc and the components of ζ^* are calculated for a range of Gaussian kernel lengths between 1-6 h^{-1}Mpc. The bands have the same meaning as in Figure 3.9.

cosmological estimates. In particular, we are interested in simulations of data sets with $R_{\rm max} \sim 150h^{-1}$ Mpc, which is comparable to the survey size of 2M++, the depth of which varies from 125 h^{-1} Mpc to 200 h^{-1} Mpc, with an effective spherically-averaged radius of 175 h^{-1} Mpc. Given the size of the MDPL2 simulation, it is possible to generate multiple independent (non-overlapping) finite volume realisations. For each sphere, we ignore any galaxy that exists outside of the sphere, and assign $\delta = 0$ for points outside the sphere. Hence each sphere represents a local universe realisation: it can be over- or underdense, so we renormalize δ using the mean density within the sphere instead of the simulation box average. For each sphere, we then calculate β/f and $\sigma_{8,{\rm g}}$ using only that sphere's galaxies, although $\sigma_{8,m}$, which appears in the denominator of ζ^*, continues to be calculated from the full simulation. As in real analyses, to account for the missing contribution from structures beyond the sphere's edge, in addition to fitting the β/f, we also fit a residual bulk flow term.

Figure 3.9 demonstrates how ζ^* and $\sigma_{8,{\rm g}}$ depend on $R_{\rm max}$ for the case with no mass cut on the galaxy catalogue. As expected, as the size of the sphere increases, results converge to the values found for the full simulation for $R_{\rm max} \geq 200h^{-1}$ Mpc.

There is a significant amount of scatter in the measured σ_8 values for small $R_{\rm max}$, varying by as much as 10% of the mean value, and with a mean value that tends to be between 4-8 % lower than that of the full simulation. The bias in the mean may be due to renormalizing the density fluctuation, $\delta = (\rho - \bar{\rho})/\bar{\rho}$ with the *local* $\bar{\rho}$ measured on the scale of the sphere, $R_{\rm max}$, thus effectively filtering out the contribution to σ_8 from large-scale waves. The scatter arises from sample variance effects, which is a combination of cosmic variance in the underlying DM structures and stochasticity in the SHMR. This decreases as $R_{\rm max}$ increases.

Likewise, the locally-measured value of β/f also varies from sphere to sphere. Again, there are several reasons for this. First, the local $\bar{\rho}$ averaged over the sphere will differ from the true average. This is important because, as noted above, it leads to a renormalization of δ. Second, there is also stochasticity in the SHMR which may affect the locally-measured β/f. Of these two, the first effect is the dominant one: we find that the total scatter in β/f for $R_{\rm max} = 150h^{-1}$ Mpc at $R_G = 4h^{-1}$ Mpc is typically 7.0% and is mostly due to cosmic variance in $\bar{\rho}$. The scatter in β/f dominates the scatter in $\sigma_{8,{\rm g}}$ (2.5%) when they are combined in ζ^*.

Figure 3.10 demonstrates how the cut samples ($R_{\rm max} = 150h^{-1}$ Mpc) depend on the Gaussian smoothing radius R_G. In particular, when compared to Figure 3.8 we find that the average ζ^* for these volume-limited realisations are unbiased between 3.75-4.75 h^{-1} Mpc. The value of ζ^* at $R_G = 4h^{-1}$ Mpc ranges between 0.98-1.01. More importantly, the standard deviation in ζ^* from sphere to sphere is 0.077 at $R_{\rm max} = 150h^{-1}$ Mpc, although this declines significantly to 0.032 at 200 h^{-1} Mpc and 0.020 at 300 h^{-1} Mpc. This suggests that sample variance effects are the dominant uncertainty in $f\sigma_8$ for current data sets.

The 1D velocity scatter as a function of R_G has a similar shape as found previously, but is 40-50 km/s larger than for the full simulation box. This increase in the scatter is primarily due to the degradation of the predicted velocities as one approaches $R_{\rm max}$. When we compare the 1D σ_v for the subsample of galaxies located within the inner half of the sphere's volume with those in the outer half at an $R_G = 4h^{-1}$ Mpc, we find scatters of $\sim$ 165 km/s and $\sim$ 210 km/s, respectively. This increase is attributed to the fact that the velocity tracers near the outer edge have poorer predicted peculiar velocities because of unaccounted-for structures outside of the survey limits.

3.9 Summary and Discussion

The key results of this chapter are as follows:

- The velocities of DM haloes are well predicted by linear theory from the true density field with a Gaussian smoothing $R_G = 4h^{-1}$ Mpc with a velocity scatter of 154 km/s. This is in agreement with Appendix A of Carrick et al. (2015).
- This can be understood because, in Fourier space, a Gaussian filter with $R_G = 3 - 4$ h^{-1} Mpc is a good match to the cross-correlation function of the density and velocity fields.
- The accuracy and precision of the linear theory predictions do not depend on the mass of the velocity tracer; there is no "velocity bias", except for clusters with $M_{\rm h} > 10^{14}h^{-1}{\rm M}_{\odot}$.
- If DM haloes are used as tracers of the density field, and one calculates $\sigma_{8,\rm h}$ of the halo-mass-weighted density field, then $\beta_{\rm h}\sigma_{8,\rm h}$ is a good estimator of $f\sigma_8$.
- If noise is added to the DM halo masses, then $\zeta^* = \frac{\beta}{f}\frac{\sigma_{8,\rm h}}{\sigma_{8,\rm m}}$ is biased high by only a percent, for a 0.1 dex noise level.
- When galaxy luminosity or stellar mass are used for the density field, the values of ζ^* indicate that the method is unbiased to within 5%, depending on the semi-analytic galaxy formation model.

- When the density field is restricted to a finite volume, there is additional uncertainty due to cosmic variance, at the level of 7% for a 150 h^{-1}Mpc sphere.

The results for ζ^* calculated using the same tracers for the velocity and density field, are summarised in Table 3.1. Overall we find that the method has $\sim$ 5% systematic uncertainties. This can be improved with semi-analytic galaxy formation models that more carefully match the real SHMR and its scatter. There is also uncertainty due to finite volumes and cosmic variance.

Previous work has neglected the additional scatter due to the coupled effects of stochasticity in the galaxy-mass relation and the cosmic variance effect of finite volumes. For example, the 2M++ catalogue (Lavaux & Hudson, 2011) has an effective volume of 175 h^{-1} Mpc. The SAGE model, weighted by stellar mass, shows that, for 150 h^{-1} Mpc spheres, the uncertainty on $\beta_{\rm g}\sigma_{8,g} = f\sigma_8$ is 7.7%, while the expected (interpolated) value for a survey of 2M++'s size is 5.2%. This is slightly higher than the uncertainty estimated by Carrick et al. (2015), Boruah et al. (2020) and Said et al. (2020) who adopted a 4% sampling variance uncertainty, plus observational errors in β due to uncertainties in peculiar velocity measurements, which are subdominant. For precise quantification of the biases and systematic uncertainties in $f\sigma_8$ derived from a specific survey, e.g. 2M++, the best approach to minimising the systematic errors will be to create mock catalogues that mimic the geometry and selection of that particular survey.

The cosmic variance uncertainty can be reduced in the future with deeper, all-sky redshift surveys. For example, a survey extending to a redshift of 0.2 (600 h^{-1}Mpc) would have an uncertainty of only 0.4% in the mean mass density and hence 0.5 – 0.6% in the luminosity (or stellar mass) density. In the North, the DESI Bright Galaxy Survey (DESI Collaboration et al., 2016), will observe 10 million nearby galaxies. In the South, 4MOST (de Jong et al., 2019) has the capability to survey large volumes in the nearby Universe. The future looks bright.

Chapter 4

Cosmological Parameters Estimated From Velocity – Density Comparisons: Calibrating 2M++

The objective of this chapter is to investigate survey selection effects in more realistic detail, specifically those inherent in the 2M++ survey compilation. The peculiar velocities generated using this survey have been used by numerous other works, so here we determine the extent to which previous calculations may be affected by these selection biases. In particular, we focus on effects due to flux-limited samples and obscuration as a result of the Galactic plane. We do this by generating mock catalogues of 2M++ using the MDPL2 simulation and SAMs to recreate the conditions that would be introduced because of these effects. In brief, we 1) cut the simulation down to the maximum survey depth, 2) use the stellar masses in each one of these local universes to generate K-band luminosities for each of the galaxies, 3) determine if each galaxy could be observed from the centre of the mock universe, 4) apply Galactic latitude cuts so that they match the observational constraints of the 2M++ survey. We then use our mock catalogues to understand these survey effect biases to correct previous measurements of $f\sigma_8$ *which use the true 2M++ density field.*

4.1 Introduction

Over the past few decades, cosmology has evolved into a precision science. The vast amount of data across a wide range of redshifts has enabled the precise measurements of cosmological parameters (Planck Collaboration et al., 2020a; Alam et al., 2021; Abbott et al., 2022; Brout et al., 2022). The standard cosmological model assumes that on all scales gravity is described by general relativity with two additional assumptions; that there is a positive cosmological constant ($\Lambda > 0$) resulting in the Universe's accelerated expansion, and the presence of cold dark matter (CDM). While ΛCDM has been incredibly successful in explaining observations, both at high and low-redshifts, some tensions do exist between measured results. As the uncertainty in these measurements decreases, we are entering an era where even slight deviations from ΛCDM could potentially show up as a meaningful anomaly in the data.

There are two fundamental ways to test the standard cosmological model: by studying the Universe's cosmic expansion history over a wide range of redshifts and by measuring the growth rate of cosmic structure. In linear theory, peculiar velocities, which are the deviations in the motions of galaxies from the overall expansion of the universe, constrain the degenerate parameter combination of the logarithmic growth rate f and the amplitude of matter density fluctuations on scales of $8h^{-1}$ Mpc, σ_8. ΛCDM predicts that the growth rate should be scale independent and related to matter density by $f(z) \approx \Omega_m(z)^{0.55}$ (Linder, 2005). However, in modified gravity models, it not uncommon for theories to predict growth rates that are scale dependent (as discussed in Baker et al., 2014). Peculiar velocities play a crucial role in distinguishing and testing cosmological models, particularly when it comes to fluctuations on the largest scales where the effects of modified gravity become apparent. This makes peculiar velocities an essential tool for disentangling different cosmological scenarios and evaluating the validity of the standard cosmological model (Koda et al., 2014; Howlett et al., 2017a).

One key aspect that makes peculiar velocity measurements particularly important is their ability to map out matter distributions at low redshifts where other observational techniques are limited or less accurate. In particular, there are still tensions related to $S_8 \equiv (\Omega_\mathrm{m}/0.3)^{0.5}$ and $f\sigma_8$ that typically arise when comparing measurements obtained from different observational probes[1]. Specifically, measurements of cosmic microwave background (CMB) anisotropies by Planck Collaboration et al. (2020a) show a tension at the level of $2-3\sigma$ when compared to lower redshift probes such as weak gravitational lensing and galaxy clustering (eg; Asgari et al., 2021; Abbott et al., 2022; Li et al., 2023)

The use of peculiar velocity surveys to measure the growth rate and galaxy bias has an extended history (eg. see Strauss & Willick, 1995), and has been done in many different

---

[1] Note that the two parameters are closely related in ΛCDM: $S_8 = 1.94\, f\sigma_8\, (\Omega_\mathrm{m}/0.3)^{-0.05}$. The last term is negligible for plausible values of the cosmological parameters, varying from 1.0034 to 0.9968 as Ω_m is varied from 0.28 to 0.32.

fashions: by modelling the density and peculiar velocities fields using a maximum-likelihood approach under the assumption both fields are drawn from multivariate Gaussian distributions (Johnson et al., 2014; Huterer et al., 2017; Howlett et al., 2017c; Adams & Blake, 2017, 2020), deriving it from the two-point statistics of direct peculiar velocity estimates for individual galaxies (Gorski et al., 1989; Strauss & Willick, 1995), via measurements of the galaxy-velocity correlation function (Nusser, 2017; Dupuy et al., 2019; Turner et al., 2021), and measuring the momentum power spectrum (Park, 2000; Park & Park, 2006; Howlett, 2019; Qin et al., 2019).

The earliest methods focused on reconstructing and predicting the peculiar velocity field using the underlying galaxy density field (Pike & Hudson, 2005; Davis et al., 2011; Turnbull et al., 2012; Carrick et al., 2015; Boruah et al., 2020; Said et al., 2020; Lilow & Nusser, 2021). This is the method that we use in this thesis. Linear perturbation theory states that the relationship between matter overdensity, $\delta \equiv \rho/\bar{\rho} - 1$, and peculiar velocities, $\boldsymbol{v}$, is given by

$$\boldsymbol{v}(\boldsymbol{r}) = \frac{Haf(\Omega_m)}{4\pi} \int \delta(\boldsymbol{r}') \frac{(\boldsymbol{r}' - \boldsymbol{r})}{|\boldsymbol{r}' - \boldsymbol{r}|^3} d^3\boldsymbol{r}'. \tag{4.1}$$

Formally, this is only true in the linear regime where density perturbations are small, i.e. $|\delta| \leq 1$.

However, the total density contrast δ cannot be measured empirically, as it is dominated by dark matter. Instead, an assumption must be made as to how the observed galaxies trace the underlying total matter. If one assumes linear biasing, the relation is $\delta_{\rm g} = b_{\rm g}\delta$, where $b_{\rm g}$ is the linear bias and $\delta_{\rm g}$ is the density fluctuation field of the *galaxies*. The same relation is then also true for the standard deviation of fluctuations in an 8 h^{-1}Mpc sphere: $\sigma_{8,g} = b_g \sigma_8$. Under this assumption, we can replace δ in eq. 4.1 with $\delta_{\rm g}/b_{\rm g}$ and move $b_{\rm g}$ to the denominator outside the integral. Comparing the predicted and observed peculiar velocities allows us to measure the degenerate combination $\beta \equiv f/b_{\rm g}$. If linear biasing holds, then by measuring $\sigma_{8,{\rm g}}$ directly from galaxy surveys, the galaxy bias can be eliminated and we are left with the degenerate cosmological parameter combination

$$f\sigma_8 = \beta\sigma_{8,g} \,. \tag{4.2}$$

Another motivation for understanding the accuracy and precision of predicted peculiar velocities arises from their use as corrections to the observed redshift and the impact of these on measurements of the Hubble parameter and other cosmological parameters measured from the Hubble diagram. In the case of the Hubble parameter, early work focused on the effect of Virgo infall peculiar velocities. For more recent supernova-based calibrations, Neill et al. (2007) showed that peculiar velocity corrections impacted the fit to the Hubble diagram and hence the measurements of the cosmological parameters. More recently, the peculiar velocity predictions of C15 have been absorbed into the redshifts of the supernova rung of the distance ladder when measuring H_0 (Riess et al., 2016, 2022; Peterson et al., 2022). Therefore, the uncertainties on these corrections make up part of the total error budget in H_0.

Velocity-velocity comparisons, while a valuable method to probe cosmological parameters, may be subject to several potential biases that need to be carefully considered in their interpretation. Redshift data from comprehensive compilations like 2M++ (Lavaux & Hudson, 2011) allow for the reconstruction of density and velocity fields to be performed more accurately than ever before. The previous chapter, investigated how the choice of density field tracer affected the recovered values of β and $f\sigma_8$. We measured the dependence of these quantities on the choice of tracer object used to create the density field: dark matter particles and haloes from N-body simulations, or galaxy observables, such as stellar mass and luminosity from the semi-analytic models (SAMs). That work did not explore in detail any biases that arise due to survey selection effects.

In this chapter, we explore the additional uncertainties that arise due to survey selection effects in the 2M++ survey compilation, and how these selection effects impact measurements of the cosmological parameters. We will focus on weighting the density field primarily by the 'observed' K-band luminosity in the presence of a flux-limited redshift survey as was done in Carrick et al. (2015, hereafter C15). Additionally, surveys lack redshift data close to the Galactic plane of the Milky Way, a region known as the Zone of Avoidance (hereafter ZoA). This region of the sky is difficult to observe due to the dense concentration of stars, gas, and due to dust in our galaxy's disk. This results in missing large-scale structures in our density maps, which in turn impacts the prediction of peculiar velocities and inferred parameters such as β.

We approach work in this chapter in the same vein as Chapter 3, where instead of simulating all the observational properties of the surveys simultaneously, our approach focuses on considering the different physical effects that can introduce bias or uncertainty into our results one-by-one. This work performed in this chapter is similar in spirit to that of Lilow & Nusser (2021), who studied similar biases and correction procedures for cosmological parameters based on the reconstructed 2MRS density field, which is slightly shallower than 2M++.

This chapter is organised as follows. We present the method used to generate our mock 2M++-like surveys in Section 4.2. Section 4.3 focuses on the effects generated solely due to flux limiting the data. In Section 4.4 we explore how the treatment of the Zone of Avoidance impacts measurements. Section 4.5 investigates how these two biases are impacted when dealing with a full mock realisation of 2M++. We present how these results impact our previous measurements in Section 4.7. Finally, we present our conclusions in Section 4.8.

4.2 Generating Mock 2M++ Surveys and Density Fields

In order to study peculiar velocities sourced by a density field on large scales (and since the integral in eq. 4.1 is over all space), one requires a galaxy catalogue to not only be as deep as possible, but also to cover a large fraction of the sky. One such catalogue that meets the latter criterion is the 2M++ galaxy redshift compilation (Lavaux & Hudson, 2011). The redshifts of 2M++ were obtained from three redshift surveys with different depths and sky coverage: the Two-Micron All-Sky Redshift Survey (2MRS; Huchra et al., 2012), the third data release Six-degree Field Galaxy Survey (6dFGS DR3; Jones et al., 2009), and the Sloan Digital Sky Survey Data Release 7 (SDSS DR7; Abazajian, 2009). The resulting catalogue is highly complete to a distance up to 200 h^{-1}Mpc (or equivalently K < 12.5) for regions covered by either 6dFGRS or SDSS, otherwise for the regions covered only by 2MRS is complete out to 125 h^{-1}Mpc (or K < 11.5).

4.2.1 Simulation Data

We used the MultiDark Planck 2 simulation (MDPL2), which is part of MultiDark project, a suite of cosmological hydrodynamical simulations (Klypin et al., 2016). The simulations all assume a flat ΛCDM cosmology with cosmological parameters: $\Omega_\Lambda = 0.692885$, $\Omega_M = 0.307115$, $h = 0.6777$, $\sigma_{8,\mathrm{linear}} = 0.8228$, and $n_s = 0.96$, such that they are consistent with Planck results (Planck Collaboration et al., 2020b). The (non-linear) $\sigma_{8,\mathrm{m}}$, measured from the particles, is 0.925. MDPL2 uses 3840^3 DM particles with masses equal to 1.51×10^9 $h^{-1}\mathrm{M}_\odot$. Rockstar and ConstistentTrees were used to identify more that 10^8 haloes (Behroozi et al., 2012), and generate halo merger trees (Behroozi et al., 2013). MDPL2 has a periodic box of length 1000 h^{-1} Mpc and is evolved from a redshift of 120 to 0, along with a varying physical force resolution level from 13-5 h^{-1} kpc and various implemented physics.

The SAG (Cora et al., 2018) and SAGE (Croton et al., 2016) SAMs were calibrated to generate galaxy catalogues using the MDPL2 simulation. These models include the most relevant physical processes in galaxy formation and evolution, including: galaxy mergers, radiative cooling, chemical enrichment, supernova feedback and winds, star formation, starbursts, and disc instabilities. A comprehensive review of the models can be found in Knebe et al. (2018).

This thesis uses the snapshots taken at $z = 0$. Both the halo and galaxy catalogues were obtained from the COSMOSIM database [2].

From the MDPL2 survey we generate 15 independent (non-overlapping) finite volume realisations of radius 200 h^{-1}Mpc to be consistent with the hard radius cuts applied in the analysis of C15. Any galaxy that exists outside of each mock local Universe is ignored. For each sphere, we take the Cartesian velocities and project them to a radial velocity.

4.2.2 Generating K-band Luminosities

The cosmological simulation and SAMs used in this thesis provide both galaxy halo and stellar masses. However, as we are interested in generating realistic 2M++ mock catalogues of the local Universe, we need the mock galaxy observables to be consistent with this survey, which in this case uses K-band luminosities. However, as this observable is not provided by the SAMs, in this thesis, K-band luminosities were generated using the abundance matching technique. This provides a simple and effective method which traditionally is used to associate galaxies with dark matter halos (Marinoni & Hudson, 2002; Kravtsov et al., 2004; Behroozi et al., 2010; Moster et al., 2010). As K-band luminosity is a good proxy for stellar mass, the inverse should also be true. A simple explanation of this technique is that given a stellar mass and a galaxy luminosity function, K-band luminosities are assigned such that the most massive galaxy (according to its stellar mass) is assigned the brightest K-band luminosity, the second most massive galaxy has the second brightest luminosity, and so on.

To replicate the K-band luminosity function of the 2M++ survey, we use the Schechter function (Schechter, 1976) parameters values associated with the survey to do the abundance matching:

$$\Phi(L) = \left(\frac{\phi_s}{L_*}\right)\left(\frac{L}{L_*}\right)^{\alpha} \exp\left(\frac{-L}{L_*}\right), \tag{4.3}$$

where ϕ_* is the density normalisation, L_* is the absolute magnitude break in the luminosity, and α is a power-law parameter to be determined. For 2M++, $\alpha = 0.73$, $L^* = -23.17 - 5\log_{10} h$ and $\phi^* = 1.11 \times 10^{-2} h^3$ Mpc^{-3} (Lavaux & Hudson, 2011). More generally, this approach likely complicated by scatter in the galaxy stellar mass-luminosity relation (Tasitsiomi et al., 2004; Behroozi et al., 2010), but for the purpose of this chapter we ignore this additional complication as there is already scatter present in the halo stellar-mass relation of MDPL2 (see Hollinger & Hudson, 2021, for more details).

---

[2] `www.cosmosim.org`

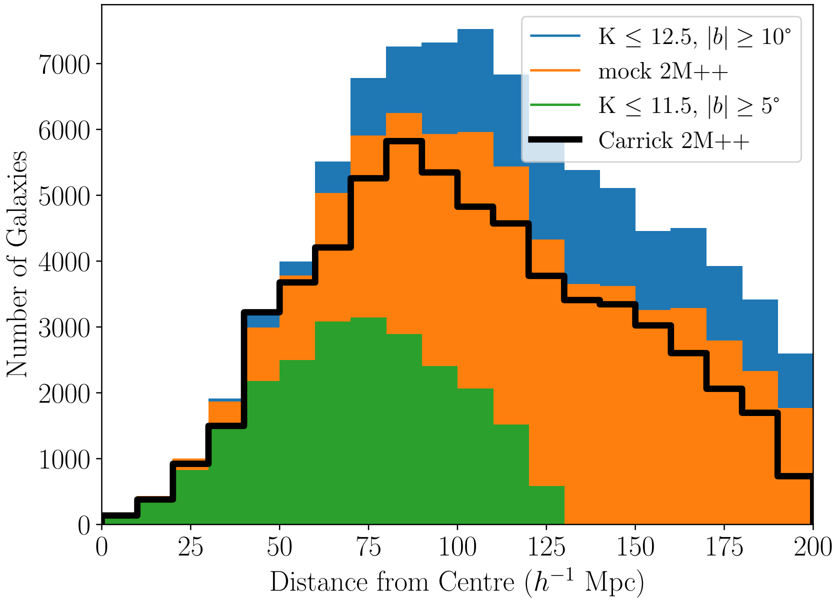

Figure 4.1: Histogram of SAG galaxies in a mock local Universe that could have been observed given the 2M++ survey magnitude limits, as a function of comoving distance. The black line represents the 2M++ galaxy data observed, taken from C15. The blue and green histograms represent the two K-band magnitude flux limits of 11.5 and 12.5. The former ignores data that is within ± 5° from the Galactic plane (matching the 2MRS survey) and the latter ± 10° (as in the 6dFGRS and SDSS redshift surveys). The orange histogram shows the mock Universe with the 2M++ survey mask and conditions applied.

Shown in Figure 4.1 are redshift histograms from one of the mock volumes used in this chapter. It demonstrates the count of galaxies as a function of distance after luminosity and distance cuts have been applied, see Section 4.3.3 in which these are described. Specifically, we show two flux-limited surveys (6dFGRS/SDSS and 2MRS assuming full celestial sphere coverage) and a mock that matches the variable depth of the 2M++ compilation. The latter is a good match to the observed redshift distribution in 2M++ (from C15).

4.2.3 Apparent Magnitude Limits and Weights

A complication of analyses performed with galaxy redshift surveys is that the data used to generate the density field are typically flux-limited. In this chapter, we are interested in replicating the 2M++ survey, as described in Lavaux & Hudson (2011), to understand the different biases associated with the survey. To be able to match the survey conditions, we must also apply the relevant flux limits to the mock data. As we are mainly interested in how the various effects individually and collectively impact our measurements of cosmological parameters, we apply the 11.5 and 12.5 apparent magnitude limits of the survey independently, to see how each impact the measurements. In order to do so, however, we need first to account for survey incompleteness by weighting the 'observed' objects, before constructing a density field, using the weighting schemes described in C15.

Here we summarise the method used to calculate the weights applied to galaxies that would be observed in our mock Universe catalogues. There are multiple ways to model the link between the galaxy and the dark matter density assuming that the relation between the two is linear. As we are unable to measure the mass density fluctuation field directly, we use either the number or luminosity density field in order to construct δ_g. We will consider both schemes in this chapter, but will, by default, use the luminosity-density field to compute the density fluctuations.

To determine whether a galaxy would be visible in our mock catalogues, we calculate the minimum luminosity each galaxy would have to be at their given distance from the centre of our local mock Universes, in order to be be visible for the given apparent magnitude limits of 2M++. Any galaxy whose luminosity falls beneath this minimum is excluded from the calculations of the density field.

For each mock, we generate appropriate weights to be applied to individual galaxies to account for survey incompleteness in the outer regions, using the luminosity function. There are multiple ways these weights can be generated, however our prescription to account for incompleteness is done by weighting galaxies using a method similar to Davis & Huchra (1982). Under the assumption that the relation between the galaxy and underlying dark matter density fields is linear, we can use both the galaxy number and luminosity density fields as a proxy. In this chapter we will explore both the number and luminosity weighted schemes, however our analysis will focus mainly on the latter, unless otherwise specified.

For the number-density field case, we weight our 'observed' galaxies by the number of galaxies at a given distance that are not observed due to survey magnitude limits. In this scheme galaxies are weighted by:

$$w^N(r) = \frac{N_{\text{average}}}{N_{\text{observed}}(r)} = \frac{\int_{L_{\min}}^{\infty} \Phi(L)dL}{\int_{4\pi r^2 f_{\min}}^{\infty} \Phi(L)dL}. \tag{4.4}$$

The K-band luminosity-density should be a good proxy for stellar-mass-weighted density field, which in turn may be a better proxy for the density of dark matter than simply weighting by galaxy number. For this luminosity-weighted case the weights are determined via:

$$w^L(r) = \frac{L_{\text{average}}}{L_{\text{observed}}(r)} = \frac{\int_{L_{\min}}^{\infty} L\Phi(L)dL}{\int_{4\pi r^2 f_{\min}}^{\infty} L\Phi(L)dL}. \tag{4.5}$$

4.3 Recovery of the Cosmological Parameters

Having calculated the density field according to some tracer population of galaxies (e.g., luminosity-weighted or number-weighted), we now turn to assess how well these density fields can be used to predict the N-body peculiar velocities and whether there is bias in cosmological parameters, such as $f\sigma_8$. In Section 4.3.1, we describe how the fits are performed, while Section 4.3.2 discusses the results for the simple case of a volume-limited sample, and Section 4.3.3 presents the results for the more realistic flux-limited case.

4.3.1 Comparison of Predicted and Actual Peculiar Velocities and Fitted Cosmological Parameters

The method used to estimate peculiar velocities from the mock catalogues, and compare these to the actual halo peculiar velocities in the simulations, is designed to follow as closely as possible what is done in comparisons between the reconstructed 2M++ predictions and observed peculiar velocity samples (C15, Boruah et al., 2020; Said et al., 2020).

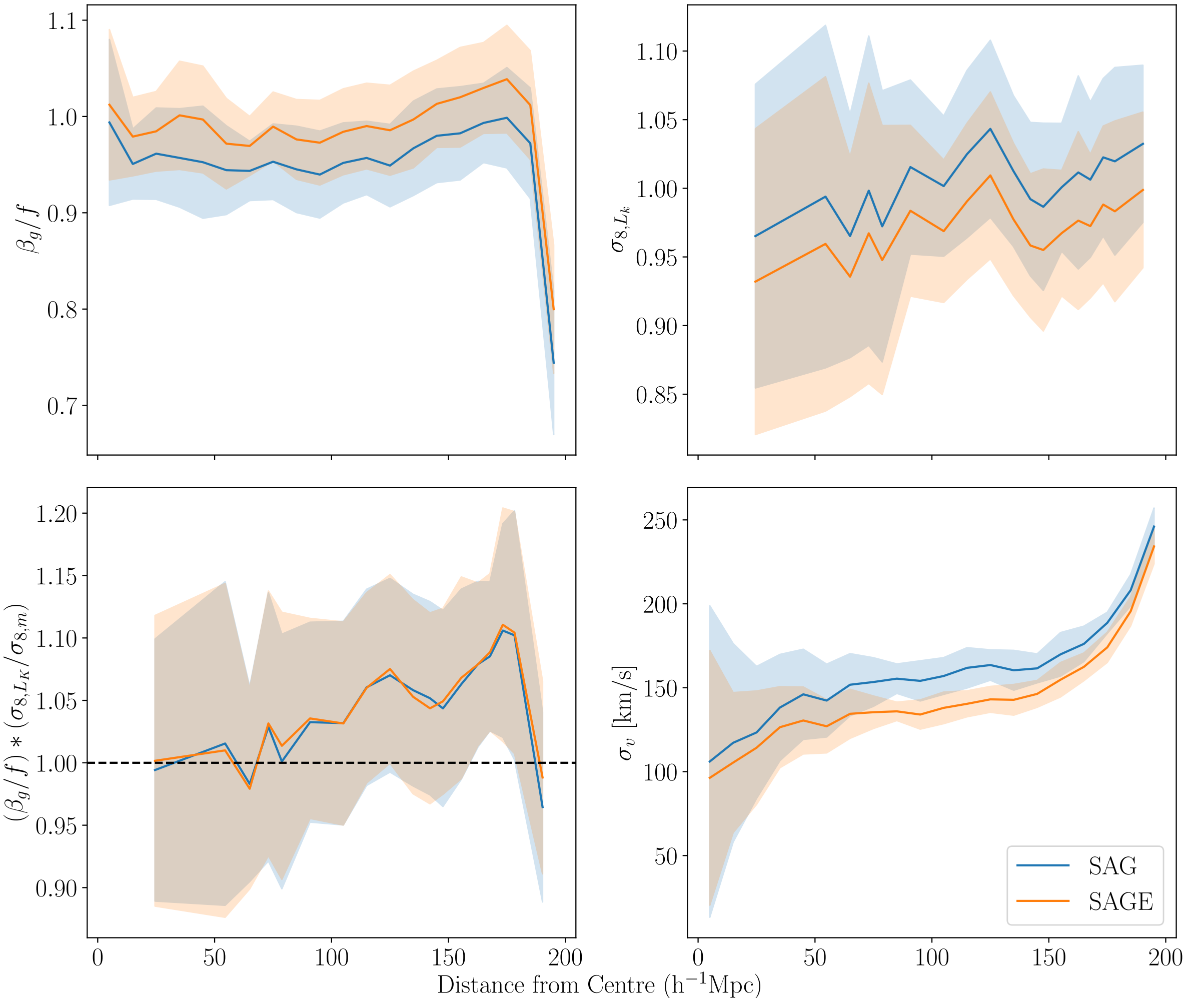

Figure 4.2: Velocity field parameters from the volume-limited luminosity-weighted mock density fields, obtained from using SAG (blue) or SAGE (orange) data. The solid lines represent the average parameter values while the lighter semi-transparent band represents the standard deviation (from mock to mock) as a function of radius from the centre of the mock local universes. Top Left: Measured value of β/f in shells of 10 h^{-1}Mpc. Top Right: σ_8 measured in equal volume bins. Bottom Left: Measured value of ζ^*. A value of $\zeta^*$of unity, shown by the black dash line, indicates where this velocity–density cross-correlation method is unbiased. Bottom Right: The scatter between the measured N-body and predicted peculiar velocity associated with each of the linear regression slopes, with the same binning as the top left panel. Note that the binning in the panels are inconsistent: there are a limited number of non-overlapping 8 h^{-1} Mpc spheres that can be fit, as a result the values that are dependent on σ_8 are binned such that the bins have approximately equal number of spheres.

The Density and Peculiar Velocity Fields

Our procedure for generating the density and predicted peculiar velocity fields can be summarised as follows:

1. The density field is obtained by taking the tracers (generically denoted with subscript t representing, galaxy luminosity, number or halo mass) and placing them onto a padded three-dimensional grid. In the flux-limited cases, this includes weighting the galaxies (see Section 4.2.3). The density field is composed of every object that could be observed given the relevant flux limits, so both objects classified as central and satellites are used.

   Then, based on the density of tracers, we calculate the density perturbation field, $\delta_{\mathrm{t}}(\boldsymbol{r})$, and smooth it in Fourier space using a Gaussian smoothing kernel of radius 4 h^{-1}Mpc. This smoothing scale is chosen based on Chapter 3.

2. The velocity field is obtained from the smoothed density perturbation field via the Fourier-transformed version of eq. 4.1,

   $$\boldsymbol{v}_{\boldsymbol{k}} = iHaf\frac{\boldsymbol{k}}{|\boldsymbol{k}|^2}\delta_k \,. \tag{4.6}$$

   This yields the predicted peculiar velocity field in Cartesian coordinates. Note that, in practice, the fields are on a three-dimensional grid in units of h^{-1} Mpc. Therefore, $\boldsymbol{k}$ is in units of h Mpc^{-1} and so writing $H_0 = 100h$ km s^{-1} Mpc^{-1}, one sees that all factors of h cancel and the predictions are independent of the assumed value of the Hubble parameter.

3. By projecting along the line of sight the Cartesian velocity fields are then used to generate a radial peculiar velocity field.

Cosmological Parameters From the Comparison of Observed and Predicted Peculiar Velocities

Having calculated a predicted peculiar velocity field, we now wish to compare these to the true N-body peculiar velocities of halos to assess any level of systematic bias in the recovered cosmological parameters. Observationally, these parameters are found by regressing, or fitting via maximum likelihood, the measured peculiar velocities against the predictions. Our procedure for fitting the cosmological parameters from the mocks is as follows (for a more in depth discussion of these steps refer to Chapter 3.1 - 3.5).

1. We first predict the peculiar velocities by integrating over the tracer density field as described above. To account for potential contributions from external sources outside the volume, we include an "external" bulk flow, $\boldsymbol{V}_{\rm ext}$, in our analysis. The presence or absence of this bulk flow provides further insights into cosmic structures beyond what is captured by local observations alone, as discussed in Section 4.7.2. In summary, we modify eq. 4.1 so that it reads:
$$\boldsymbol{v}_{\rm pred}(\boldsymbol{r}) = \frac{Haf(\Omega_m)}{4\pi} \int_{\rm survey} \delta_{\rm t}(\boldsymbol{r}') \frac{(\boldsymbol{r}' - \boldsymbol{r})}{|\boldsymbol{r}' - \boldsymbol{r}|^3} d^3\boldsymbol{r}' + \boldsymbol{V}_{\rm ext} \,. \tag{4.7}$$

2. The true N-body radial peculiar velocities are regressed on the predicted radial peculiar velocities. The slope of the fit then gives a measurement of $\beta_{\rm t}/f = 1/b_{\rm t}$, as well as $\boldsymbol{V}_{\rm ext}$.

3. There is small correction that needs to be made to the measured values of $\beta_{\rm t}/f$, to account for differences between what is done in this chapter versus what has been done with the real 2M++ density field in C15. The galaxies in the 2M++ survey have redshifts but do not have precise distances. However, the equations used in calculating the velocities require the latter. The process used in C15 of determining the distances from the redshifts is referred to as "reconstruction". They used an iterative procedure to accomplish the reconstruction based on Yahil et al. (1991) and the grouping method of Huchra & Geller (1982). This process results in the reconstructed field having a slightly higher β (a factor 1.03 at 4 h^{-1}Mpc smoothing) than if the true distances are used (see discussion in C15, Appendix A). As a result, all measurements of β in this chapter have been increased by this factor to simulate what would have been found had we reconstructed the mock density fields.

4. We calculate $\sigma_{8,\rm t}$ of the mock density field by placing non-overlapping spheres over the entirety of the grid and ignore any sphere that includes areas that either falls outside of the survey limits or is partially located within the ZoA.

5. We then multiply these two quantities together and divide by the known particle $\sigma_{8,\rm m}$ to obtain
$$\zeta^* \equiv \left(\frac{\beta}{f}\right)\left(\frac{\sigma_{8,\rm t}}{\sigma_{8,\rm m}}\right) \,. \tag{4.8}$$
If the method is an unbiased estimator of $f\sigma_8$, we expect $\zeta^* = 1$,but if there is a bias this allows us to calibrate it.

6. We also calculate the velocity scatter around the regression, σ_v. This is a measure of how well our mock 2M++ density fields can predict the peculiar velocities.

In observational studies of the distance scale and peculiar velocities, it has been standard practice to combine the measured distances and redshifts of individual galaxies that are in groups or clusters (e.g., Sandage & Tammann, 1975; de Vaucouleurs & Bollinger, 1979; Aaronson et al., 1979; Lynden-Bell et al., 1988; Tully et al., 2023). This is because the motions of individual satellite galaxies, with respect to the centre of mass of the galaxy group, are essentially random or "thermal" noise, and not described by eq. 4.1. Therefore, here we compare the predicted peculiar velocities with the peculiar velocities of the halo as a whole (or its proxy, the central galaxy) as measured in the N-body simulation.

4.3.2 Volume-Limited Samples

Before considering the more realistic case of flux-limited samples, it is interesting to consider volume-limited samples as these make the biases close to the survey edges clear. For the analysis performed in this section, the density field was populated with the K-band luminosities of all galaxies located within the survey limits of 200 h^{-1}Mpc. We note that regardless of what density tracer is used, only objects that could be observed given the flux limits of 2M++ are used as velocity tracers.

Figure 4.2 shows recovered parameters for a volume-limited mock galaxy sample: the mock luminosities generated from the either the SAG or SAGE models are used, with no apparent magnitude cuts applied, and with a minimal stellar mass lower limit of 10^9 $M_\odot$ applied to the input galaxy catalogue. As demonstrated in the top left panel, the recovered value of β/f (which should be proportional to the inverse of the galaxy bias) is strongly influenced by the effects of the survey edges. Within 20 h^{-1}Mpc of the survey edges, the recovered β is almost 30% smaller than at other radii. This makes sense if one considers a galaxy at the survey edge: the density field beyond the outer edge, for example, is set to $\delta_\mathrm{g} = 0$, so, for that galaxy, the contribution to the integral in eq. 4.1 is from approximately half of the sky. The predicted peculiar velocities there will therefore be noisier. Since we are regressing the N-body peculiar velocities on those predicted, this additional noise in the independent variable will flatten the fitted slope, leading to a lower value of β/f[3]. This increase in scatter in the predicted velocities, shown in the bottom right panel, is indeed highest near the survey edges where velocity fields are most heavily influenced by the lack of data beyond the edge. Measurements of σ_8 (top right panel) are unaffected by edge effects and remain fairly constant across radial shell measurements.

---

[3] This phenomenon is a result of regression dilution (attenuation), which is the caused due to of errors in the independent variable (i.e. the data being regressed upon). This results in the underestimation of a fitted slope's linear regression being biased towards zero, the greater the variance the closer the estimated slope will be to zero.

While the global values of β and σ_8 are respectively higher and lower in SAG compared to SAGE, we find that measurements of ζ^* for both are effectively identical with comparable uncertainties. We note, however, that the SAG model does consistently generate slightly more scatter (~ 20 km s^{-1}) in the measured σ_v. For remainder of this chapter, we shall focus on the K-band luminosities generated from the SAG SAM unless otherwise specified.

4.3.3 Effects of Magnitude Cuts and Weights

We now turn to the more realistic case, where the redshift survey is flux-limited. In Figure 4.3, we show how our flux-limited density fields (with appropriate weights) compare to the volume-limited case, as well as to the dark matter halo field directly. This is done for both the K-band magnitude limits in 2M++ (12.5 and 11.5) with hard distance limits of 200 and 125 h^{-1} Mpc, respectively. Each column represents a different density field tracer. From left to right these are: the flux-limited K-band luminosities, the flux-limited number of galaxies, the volume-limited K-band luminosities and the halo masses. The first row shows the fitted value of β/f as a function of distance. Regardless of tracer used in the density field, all are impacted by edge effects close to the survey edges. The fitted β/f decreases as a function of distance from the centre of the sphere for the flux limited cases, while remaining constant in the volume-limited cases as expected. This is likely due to a combination of two effects. First, at larger distances the galaxies are more luminous and hence have a higher bias, driving down β. Second, the field becomes noisier and so the fit will tend to flatten (lower) β. This same effect led to a drop in β near the survey edges, as discussed in the previous subsection. Similarly, the second row shows that σ_8 increases due to the increasing sparsity in the 'observed' number of galaxies as a function of distance and the increase in luminosity of those selected, hence an increase in bias. However, in all cases the cases the average recovered value of ζ^*, shown in the third row, remains fairly constant as a function of radius, and is close to unbiased. The number-weighted case performs less well than the luminosity-weighted case, as expected, since these weights are higher at large distances, which leads to noisier density and peculiar velocity fields. Both the volume-limited cases have consistent values of β and σ_8, this is reflected in the recovered value of ζ^*. However, the halo-mass-weighted case does show the most variation in its measurement, due to the higher level of fluctuation in the halo-mass-weighted σ_8. Finally, the fourth row shows the scatter in our velocity predictions. As before, the scatter increases rapidly for locations near the survey edges. We note this effect is strongest for the number weighted case. We find that the scatter in the inner regions (~ 150 km s^{-1}) is comparable to what was found in Chapter 3, which focused on volume-limited samples.

The global (excluding the outer 20 h^{-1}Mpc) measured values of ζ^* and σ_v for this

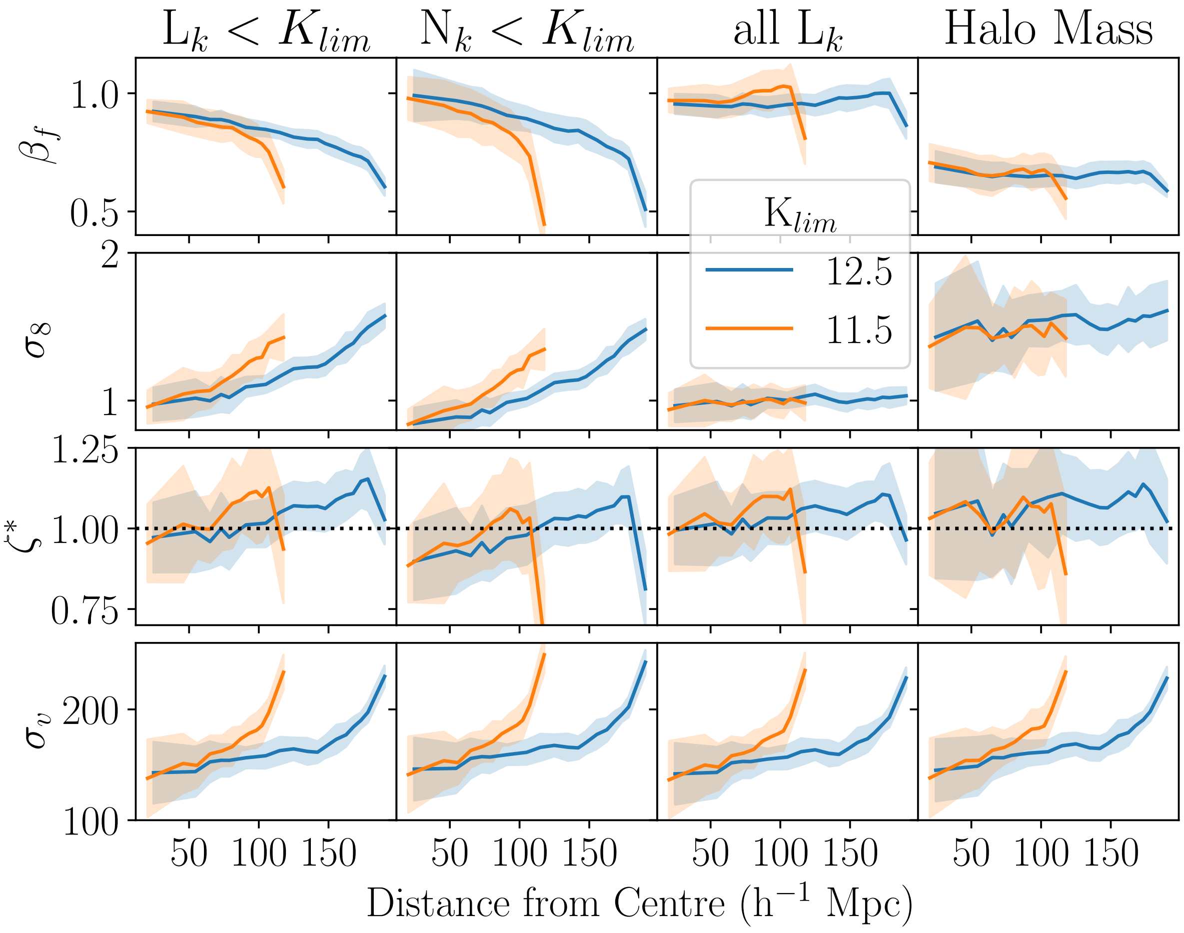

Figure 4.3: Comparison of differently-weighted density fields and the effect on recovered values. The blue and orange lines represent the two imposed survey limits for 2M++ corresponding to 200 and 125 h^{-1}Mpc, respectively, while the coloured bands have the same meaning as in Figure 4.2. The rows show the same measured quantities as in Figure 4.2, as a function of comoving distance from the centre. Each column represents the various tracers/methods used to weight the density weighted field and predict the peculiar velocities. The weightings of the density field are: (1,3) galaxies' K-band luminosities, (2) number of galaxies, and (4) halo mass. The data in the first two columns have flux limits and weights applied, corresponding to the K-band apparent magnitude limits of 12.5 and 11.5. The velocity tracers in all cases remain the same.

analysis can be found in Table 4.1. These are weighted by the number of velocity tracers at each distance in a 2M++-like flux-limited sample. As before, SAG produces slightly poorer predictions than those based on the SAGE catalogues. The SAGE velocity scatter is consistent with that assumed by C15 ($\approx 150 kms^{-1}$), while SAG's scatter is on the order of 20 km s^{-1} higher.

4.4 Complications Due to the Zone of Avoidance

Truly all-sky galaxy surveys are difficult to acquire due to the ZoA. In this region, dust extinction due to the dust in the disk of the Milky Way, as well as the high density of stars in this region, diminish our ability not only to identify galaxies but to accurately measure their properties. Therefore, at these low Galactic latitudes, our ability to generate an accurate map of the large-scale structure impedes our ability to predict the peculiar velocities of nearby galaxies and thus introduces an added level of difficulty when measuring cosmological parameters.

Recall that in 2M++ there are two Galactic latitude cuts applied to the survey data, corresponding to the surveys used in this survey compilation. As the location of the Galactic plane is arbitrary in our mocks, to each mock we consider three different Galactic plane orientations each one orthogonal to the other. In this section, we explore the effects of a simple Galactic latitude cut. We consider two cases ($|b| < 5^\circ$ and $|b| < 10^\circ$) corresponding to the two parts of 2M++. The results for the mock 2M++ catalogues can be found in the following section.

4.4.1 Treating the ZoA

There are two simple methods to compensate for the ZoA when generating velocity fields: 1) filling the region with a uniform value, or 2) mimicking the missing structure with observed galaxies outside of the ZoA. To emulate the former, we simply fill the ZoA region with the calculated mean density of the local Universe; this ensures that the value for this region is equivalent to the regions outside of our survey volume. In the latter case, in order to generate missing structure within the ZoA, we adopt a technique developed by Lynden-Bell et al. (1989): and "clone" the galaxies that are immediately located above and below the ZoA. To generate a clone galaxy at a latitude of b_c it is simply a matter of shifting the original latitude, b, using:

$$b_{\mathrm{c}} = \arcsin[\sin(b_{\mathrm{ZoA}}) - \sin(b)] \tag{4.9}$$

In order to fully understand the effects of the ZoA on the full 2M++ catalogue, we consider two Galactic latitudes to define the ZoA. In the full 2M++ catalogue, the SDSS and 6dFGRS surveys ($K_{2M++} \leq 12.5$) do not cover the region where $|b| < 10°$, whereas for the shallower 2MRS ($K_{2M++} \leq 11.5$) this region is $|b| < 5°$. As a result while 2M++ provides nearly full sky coverage, the survey conditions vary across the sky. In this section, however, we first consider near full-sky surveys with only simple latitude cuts. The realistic 2M++ scenario will be discussed in Section 4.5.1.

4.4.2 Effects of the ZoA

To demonstrate how our predictions are influenced by these Galactic latitude cuts, Figure 4.4 shows how the measurements of β/f change as a function of both Galactic latitude and distance from the centre of our mock Universes, for the flux-limited luminosity weighted samples.

We find that, on average, the cloning treatment tends to decrease the recovered value of β/f near the Galactic plane, whereas the uniform treatment increases our recovered values. As the ratio is with respect to the full-sky case, the areas that are fully within the ZoA are strongly biased, as expected, but outside the ZoA these biases reduce to less than 10% within $5-10°$, depending on the size of the ZoA. Recovered values are not drastically impacted in regions where the Galactic latitude is greater than twice the applied cut's latitude.

We find that the uniform treatment tends to cause significantly greater bias in the recovered measurements at nearby distances than the cloning treatment. For predictions in the nearby Universe (performed at distances within 50 h^{-1}Mpc), the uniform treatment is more biased by 5-15%, although in the opposite sense to the cloning case. Neither treatment is able to fully mitigate the increased inaccuracy in the velocity predictions due to the missing structures. One might naively assume that introducing structure with the cloning treatment would improve recovered values, however there is no guarantee that the cloned structure perfectly matches the "missing" structure that is hidden by the Galactic plane. This leads to a bias in the recovered β and an increase in the error in the predicted peculiar velocities, σ_{v}. We find no significant advantage to using one method over the other for predictions made *within* the ZoA: in both cases, the total scatter can reach around 250 km s^{-1}, approaching the cosmic r.m.s. velocity.

Both treatments for the ZoA result in comparable amounts of scatter being added as a function of latitude. Additionally, beyond twice the Galactic latitude cut, the amount of scatter added is small compared to the overall scatter in the predicted peculiar velocities.

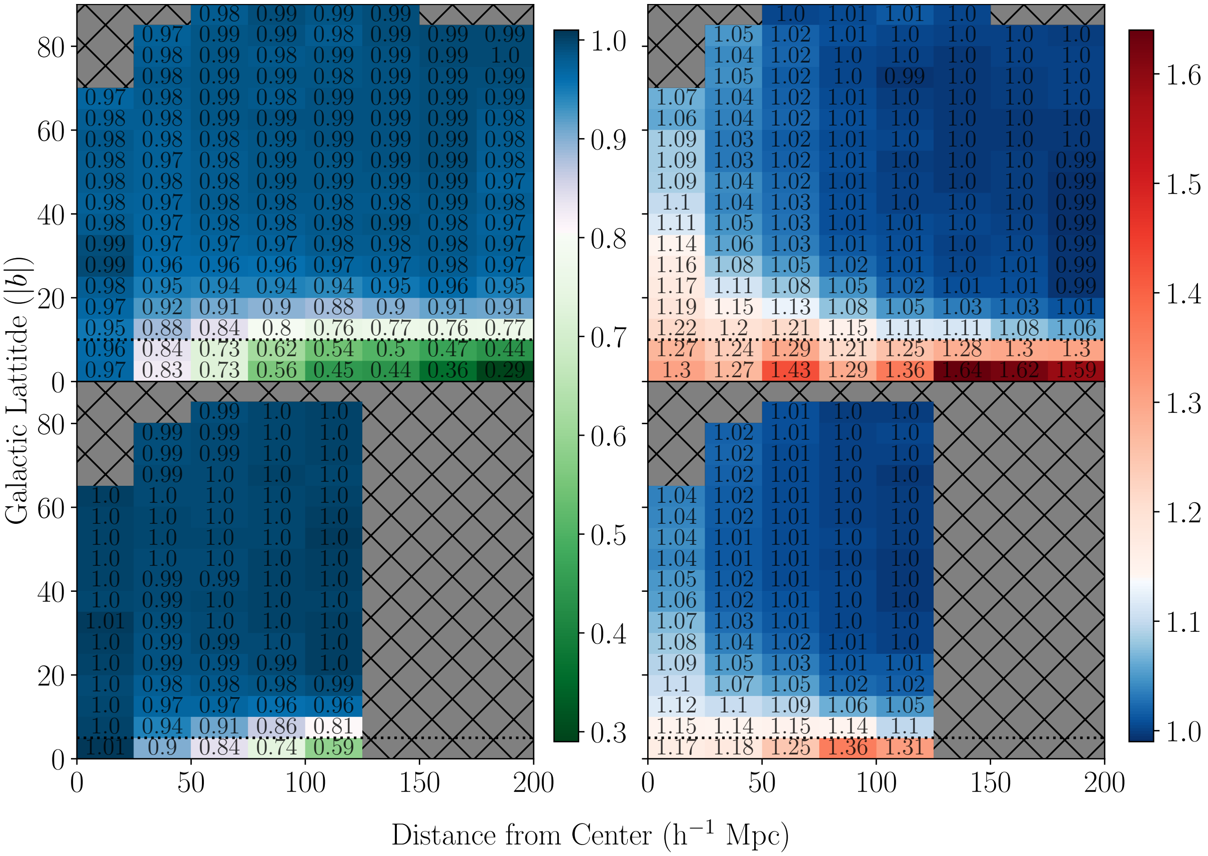

Figure 4.4: This plot demonstrates ratio of the fitted β/f measurements, when using either the cloning (left column) or uniform (right column) prescription for the ZoA, over the fitted β/f from the fiducial full-sky (no ZoA) case. The top (bottom) panels show the ratio for the $K < 12.5$ ($K < 11.5$) flux-limited case. In all cases, we measure β in radial bins of 25 h^{-1}Mpc and absolute Galactic latitude bins of 5°. We omit bins where any mock has less than 10 galaxies from this diagram. The results for the deeper (top row) and shallower (bottom row) surveys are both shown here, with the dotted line representing the galactic cut applied to each. The measurements performed below this line are calculated using velocity tracers that would have been observed in the absence of the Galactic plane. For clarity, we note the printed grey values overlaid in each bin are simply the numerical value of the bin's measurement, which in turn corresponds to the colour bar.

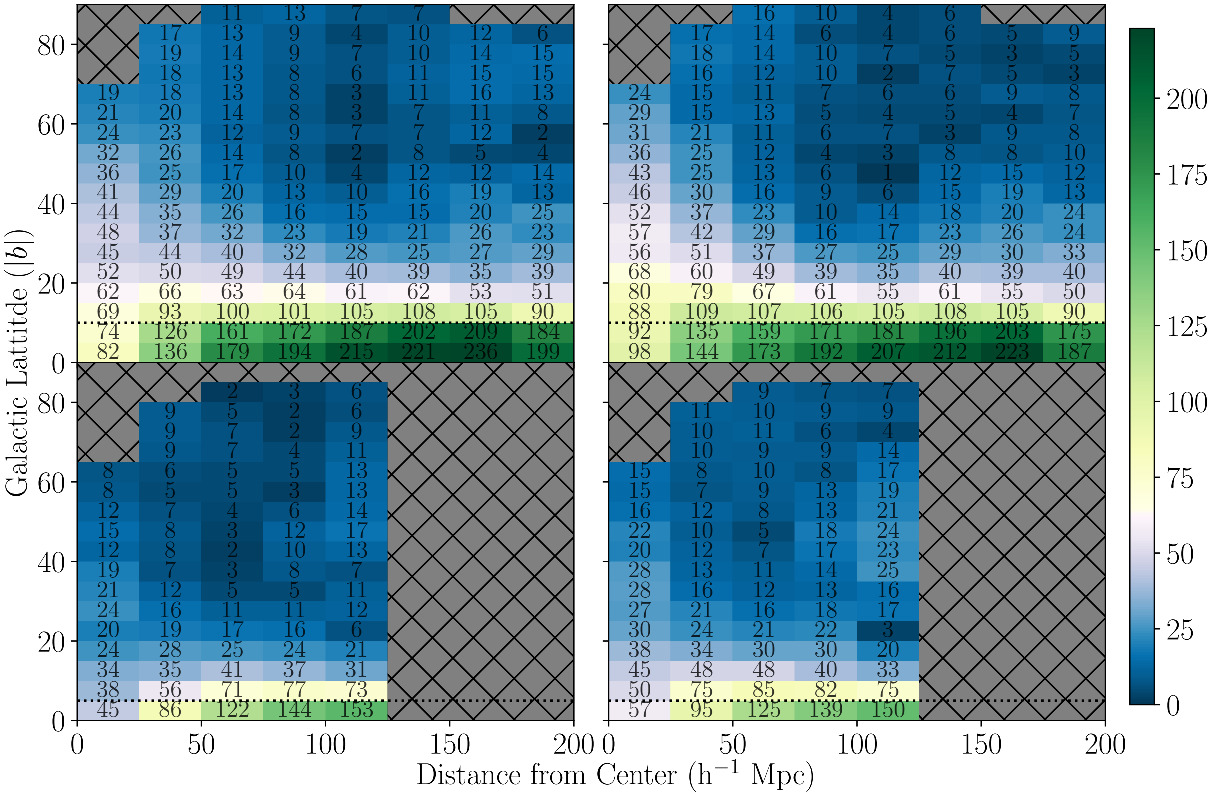

		11	13	7	7		
	17	13	9	4	10	12	6
	19	14	9	7	10	14	15
	18	13	8	6	11	15	15
19	18	13	8	3	11	16	13
21	20	14	8	3	7	11	8
24	23	12	9	7	7	12	2
32	26	14	8	2	8	5	4
36	25	17	10	4	12	12	14
41	29	20	13	10	16	19	13
44	35	26	16	15	15	20	25
48	37	32	23	19	21	26	23
45	44	40	32	28	25	27	29
52	50	49	44	40	39	35	39
62	66	63	64	61	62	53	51
69	93	100	101	105	108	105	90
74	126	161	172	187	202	209	184
82	136	179	194	215	221	236	199

		16	10	4	6		
	17	14	6	4	6	5	9
	18	14	10	7	5	3	5
	16	12	10	2	7	5	3
24	15	11	7	6	6	9	8
29	15	13	5	4	5	4	7
31	21	11	6	7	3	9	8
36	25	12	4	3	8	8	10
43	25	13	6	1	12	15	12
46	30	16	9	6	15	19	13
52	37	23	10	14	18	20	24
57	42	29	16	17	23	26	24
56	51	37	27	25	29	30	33
68	60	49	39	35	40	39	40
80	79	67	61	55	61	55	50
88	109	107	106	105	108	105	90
92	135	159	171	181	196	203	175
98	144	173	192	207	212	223	187

		2	3	6
	9	5	2	6
	9	7	2	9
	9	7	4	11
8	6	5	5	13
8	5	5	3	13
12	7	4	6	14
15	8	3	12	17
12	8	2	10	13
19	7	3	8	7
21	12	5	5	11
24	16	11	11	12
20	19	17	16	6
24	28	25	24	21
34	35	41	37	31
38	56	71	77	73
45	86	122	144	153

		9	7	7
	11	10	9	9
	10	11	6	4
	10	9	9	14
15	8	10	8	17
15	7	9	13	19
16	12	8	13	21
22	10	5	18	24
20	12	7	17	23
28	13	11	14	25
28	16	12	13	16
27	21	16	18	17
30	24	21	22	3
38	34	30	30	20
45	48	48	40	33
50	75	85	82	75
57	95	125	139	150

Figure 4.5: The binning and layout have the same meaning as in Figure 4.4, but here we show the additional velocity scatter that is generated due to treatment of the ZoA. Thus the total scatter, $\sigma_{\rm v}$, as a function of distance and Galactic latitude can be obtained by adding the values here in quadrature with the values from Figure4.3.

This can also be seen in the velocity scatter shown in Figure 4.5. This diagram has the same binning as in Figure 4.4, and shows the additional scatter in velocity that is introduced solely as a result of the ZoA treatment used. It is clear that the extra scatter in predicted peculiar velocities as a result of the ZoA is comparable for both treatment methods. As expected, the scatter increases in the same regions where the predictions are most heavily impacted by the ZoA, as was discussed previously. We note that the additional scatter introduced is still less than the predicted variations from linear theory alone. Even in the regions located directly above the ZoA, we expect the total scatter in our predictions to be only ~ 30 km s^{-1} larger than for those that are far from the ZoA. For the regions within the ZoA, i.e., $b < b_{\mathrm{ZoA}}$, as discussed previously, the scatter is on average higher for cloning than the uniform treatment by ~ 15 km s^{-1}.

4.5 Analysing the fully-realised 2M++ mocks

There are two main differences between the analysis of the full 2M++ in C15 and what we have discussed so far: the treatment of the ZoA, which is discussed in Section 4.5.1, and the way in which density fluctuations are normalised, in Section 4.5.2 below.

4.5.1 Treatment of the ZoA in 2M++

In the previous sections, our measurements for each of the K-band limited cases had a constant Galactic latitude cut for the ZoA and single maximum distance. The full 2M++ case is more complicated: the ZoA is defined as $|b| < b_{\mathrm{ZoA}}$ where

$$b_{\mathrm{ZoA}} = \begin{cases} 5^\circ & \text{if } 30^\circ < l < 330^\circ \\ 10^\circ & \text{if } l < 30^\circ \text{ or } l > 330^\circ\,, \end{cases} \tag{4.10}$$

with the additional complication that C15 only performs the cloning procedure out to a distance of 125 h^{-1}Mpc for galactic longitudes $30^\circ < l < 330^\circ$. At the longitudes close to the Galactic centre and in the distance range $125h^{-1}\mathrm{Mpc} < r < 200h^{-1}\mathrm{Mpc}$, the uniform ZoA procedure is used.

One of the goals in this work is to provide a more comprehensive uncertainty estimate of galaxies peculiar velocities as a function of their galactic coordinates and depth rather the uniform 150 km s^{-1} proposed in C15. For this section, we will continue to use the same convention as in C15, to understand potential uncertainties that need to be accounted for in the 2M++ analysis. We find that, as expected, the recovered value of ζ^* calculated using the convention described above produces a value of 1.03 ± 0.05, for a hypothetical peculiar velocity sample with the same redshift distribution as the 2M++ galaxies themselves. This value is in between that measured for the globally applied ZoA of 10° for the 200 h^{-1} Mpc mocks, as described in 4.4.2, which found values of ζ^* of 0.97 ± 0.04 for the cloned and 1.05 ± 0.04 for the uniform treatments. It is unsurprising that for this case the global 2M++ measurement of ζ^* tends to align more with the latter case due to the geometry of 2M++ discussed previously. This remains true for the number-weighted 2M++ measurement of 0.97 ± 0.06, which has a recovered cloned-ZoA and uniform-ZoA values of 0.93 ± 0.05 and 1.0 ± 0.04, respectively. In either case the recovered value is comparable to the full-sky measurement for which ${\zeta^*}_{L_K} = 1.03 \pm 0.03$ and ${\zeta^*}_N = 0.99 \pm 0.05$

4.5.2 Normalising the Density Field and the Resulting Fits of β and $f\sigma_8$

For 2M++-like surveys which are magnitude limited, the mean luminosity of the galaxies observed increases with depth. This means that on average galaxies at higher redshifts are more biased than those which are nearby, as galaxy bias increases with luminosity. In C15, this was performed by re-scaling the density field to the same effective bias using the bias model of Westover (2007), where bias changes with luminosity. That work found that $b(L)/b^* = (0.73 \pm 0.07) + (0.24 \pm 0.04)L/L^*$, where b^* is the bias of an L^* galaxy, and was determined using the correlation function of 2MASS. Since different distance ranges sample different luminosities, there is an effective bias at each distance which can calculated from the above. Figure 4.6 shows the functional form of $b_{\text{eff}}(r)/b^*$ from Westover (2007) as calculated in C15. This was then used to normalise δ_{g} so that the $\sigma_{8,\text{g}}$ at all radii corresponds to that of an L_* galaxy.

In this section, however, we use a slightly different method to normalise the density field. We directly re-scale the density field as follows. For each mock, we first calculate σ_8 in equal volume shells as a function of depth, and fit a parametric form to it, denoted $F(r)$, these are shown as the lighter bands in Figure 4.6. We divide the density field with this normalisation: $\delta_{\text{norm}}(r) = \delta_{\text{g}}(r)/F(r)$. The regressions performed using δ_{norm} thus gives a value of β_{norm}/f and, in analogy to β^*, we define the bias in this method as

$$\zeta^\dagger \equiv \frac{\beta_{\text{norm}}}{f\sigma_{8,\text{m}}} \, . \tag{4.11}$$

This normalisation procedure was applied to the 2M++ mocks. A summary of the

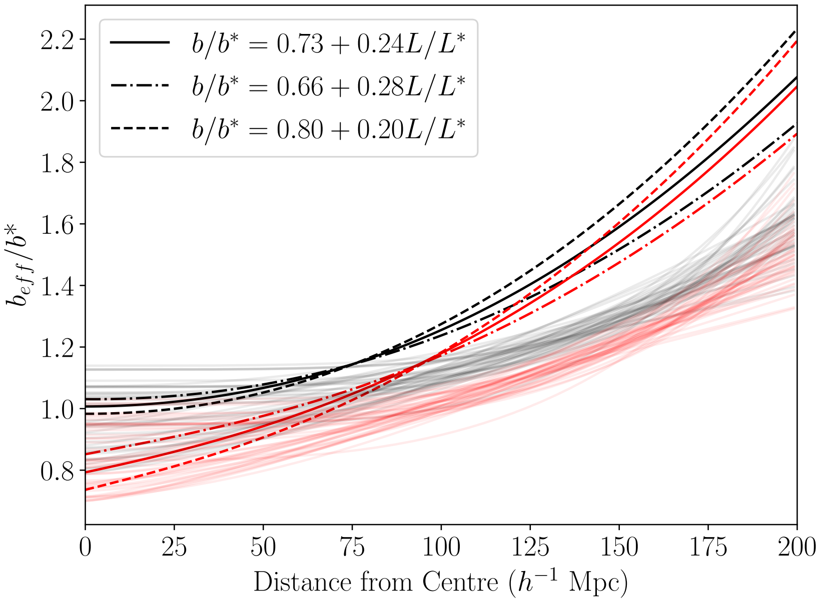

Figure 4.6: Number-weighted (red) and luminosity-weighted (black) effective bias as a function of distance for the most significant 1σ deviation of parameters from the scaling relation $b/b_* = (0.73 \pm 0.07) + (0.24 \pm 0.04)L/L_*$ from C15. The thin transparent lines are the parametric fits F(r) of σ_8 as a function of distance from the centre of the sphere for each mock Universe.

global measurements produced using this method, again excluding survey edges, can be found in Table 4.2.

As can be seen, the bias-normalisation correction in C15 is greater in the outer regions of the survey than our fitted measurements of σ_8 indicate. This is likely due to the fact that the SAMs applied to MDPL2 do not quite reproduce the same level of clustering as the real universe, as has also been found in previous works (Knebe et al., 2018; Lilow & Nusser, 2021). We also find that SAGE shows significantly less clustering than SAG. This indicates that the mocks underestimate the σ_8 of the real Universe. Should the simulations better reflect the clustering of the Universe, we should get the same correction as in Westover (2007). While the Westover correction function would significantly over-correct our mocks generated by SAG and SAGE, it not obvious that this would over-correct the real Universe.

In Figure 4.7, we show our measurement of $\zeta^\dagger$ for the realistic luminosity- and number-weighted 2M++ mocks. Overall our corrections, applied to both the luminosity and number weighted fields, result in a $\zeta^\dagger$ which is in good agreement with unity across radial shell measurements. We note however, that while the overall external bulk flow and global $\zeta^\dagger$ calculated excludes the outer survey edge, the same is not true here. Hence as expected, there are two distances where the recovered $\zeta^\dagger$ is affected by the survey edges, corresponding to 125 and 200 h^{-1}Mpc.

Figure 4.8 presents a visual summary of the key calculations performed in this chapter. The red points represent our measurements on the fully realised luminosity-weighted 2M++ mocks. For these we find that our treatments are comparable to the full-sky case (A). The realistic cloning treatment (M) for the ZoA is a marginally better treatment than the fully uniform case (N), returning a more comparable value to the our predictions for the full-sky case (A). However both treatments are in agreement with the fiducial value. Contrarily, on average for the number weighted case the uniform treatment gives a more accurate reconstruction to the fiducial, though again both are well within the uncertainty margins. We find that for values measured using the partial 2M++ cloning treatment, the values of ζ^*(M) and $\zeta^\dagger$ (Q) are almost equivalent, however the latter tends to produce a slightly higher measurement. The same is true for the fully uniform treatment, shown by points (N) and (R).

Figure 4.9 demonstrates how the scatter in our predictions changes as a function of distance from the origin and Galactic latitude. Shown are slices in the Supergalactic coordinate frame at SGZ =0, +70 and -100 h^{-1}Mpc for the realistic 2M++ treatment of luminosity weighted field. These slices demonstrate how predictions are impacted by both the shallower 2MRS regions (at positive SGX), and the deeper regions covered by SDSS and 6dFGRS. We add the average velocity scatter and the excess scatter due to the

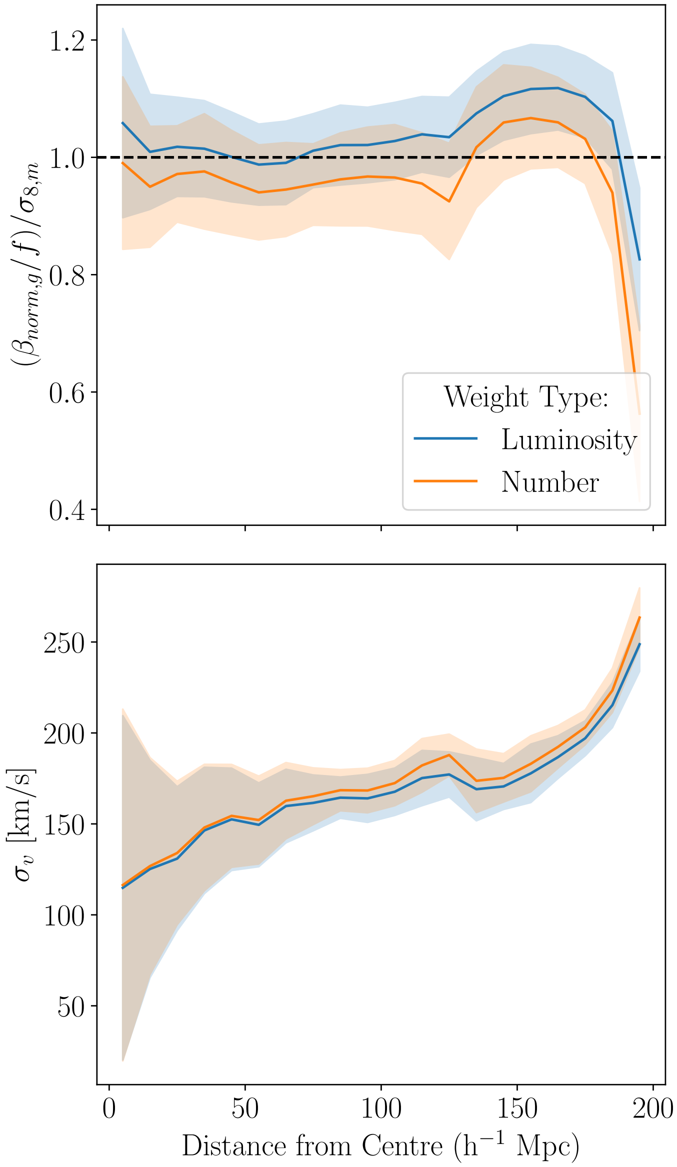

Figure 4.7: The bias in the normalised fits, $\zeta^{\dagger} = \beta_{\rm norm}/f/\sigma_{8,\rm m}$, for the mock 2M++ realisations. The density field is corrected first by the individual galaxy weights, then normalised by the fitted σ_8 curves shown in Figure 4.6.

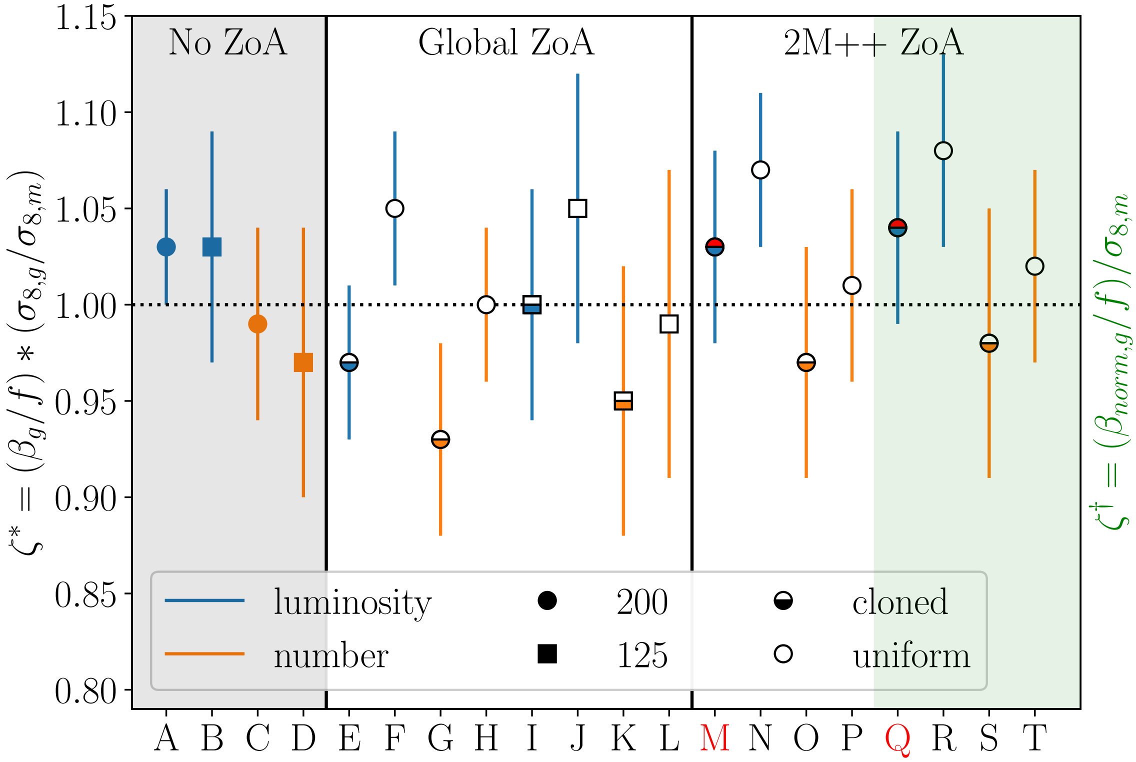

Figure 4.8: Visual summary of the more important values presented in Tables 4.1 and 4.2. The letters A-P correspond to the values of ζ^* in 4.1. A-D represent the flux and volume limited full-sky measurements, while E-L are the values calculated assuming a single global latitude cut corresponding to the two survey depths used in 2M++. Values for M-P are calculated using the fully realised 2M++ mocks. Finally Q-T are the $\zeta^\dagger$ values described in Table 4.2 of the 2M++ mocks. The blue and orange lines represent the density weighting used in calculation, while the symbol shapes are the maximum survey distance cut allowed, and the fill choice of the markers represent the method used to treat the ZoA; full: no ZoA applied, half filled: cloning the structure above and below the ZoA, empty: uniform value applied to the ZoA. The scatter in the values is the cosmic variance between the different realisations.

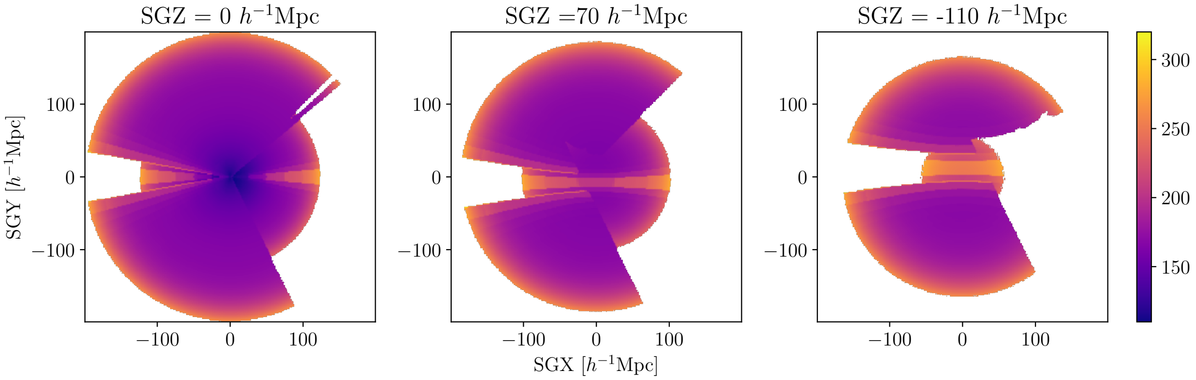

Figure 4.9: The total error, $\sigma_{\rm v}$, in the predicted peculiar velocities from the 2M++ luminosity-weighted galaxy density contrast field, using the cloning treatment of C15, for various slices in the SuperGalactic plane ($SGZ = 0$), and parallel to it. The latter are a select sample of those depicted in C15. The 2M++ density field is shallower at positive SGX as this region is covered by the 2MRS survey, whereas the remainder of the sky is covered by the deeper 6dFGRS and SDSS.

ZoA treatment in quadrature, separately for these regions as predictions are most heavily influenced by their depth (see Figure 4.3) and Galactic latitude above the ZoA (as shown in Figure 4.4). As expected the scatter in predictions are highest in regions obscured by the Galactic plane where the no structure data is known at $\sim$ 240 km s^{-1}. In the regions above and below the Galactic plane, the scatter ranges between 120-260 km s^{-1} with galaxies on average having a scatter of $\sim$ 170 km s^{-1}. This is larger than the value adopted by C15 of 150 km s^{-1} but not as extreme as the 250 km s^{-1} used in recent SN analyses (such as in Riess et al., 2018; Scolnic et al., 2018; Kenworthy et al., 2022; Riess et al., 2022). Again, we note that these estimates are only valid for central galaxies, as linear perturbation theory does not accurately predict the additional virialized velocities of satellite galaxies with respect to the group/cluster's centre of mass.

4.6 Measurements of $\zeta^*$and $\zeta^\dagger$

Here we present the full results for the measurements of ζ^*(Table 4.1) and $\zeta^\dagger$ (Table 4.2) for a wide range of different flux limits, weighting schemes and treatments of the ZoA.

Table 4.1: Measured values of ζ^* and σ_v for various tracers of our mock 2M++ catalogues. The row sections are categorised as follows: The first corresponds to the full-sky, the second to the globally applied ZoA cuts, and third the realistic 2M++ geometry. While the columns are:
1: The value corresponding to Fig 4.8.
2: The maximum sphere radius applied.
3: The tracers (t) with which the underlying density field was generated, in all cases the velocity tracers are only central galaxies which made the flux limit cut (L_k-luminosity, N-number, m_h-halo).
4: Whether or not the density field tracers were limited to the flux limited cases, if the additional weighting for luminosity or number respectively was applied.
5: The region the ZoA was applied, in general 200 and 125 correspond to 10 and 5, 2M++ corresponds to the 2M++ realistic ZoA application.
6: The method used to treat the ZoA.
7: The measured value of $\zeta^* = (\beta_\mathrm{t}/f)(\sigma_8/\sigma_{8,\mathrm{m}})$ and the standard deviation from mock to mock for the SAG catalogues.
8: The velocity scatter σ_v in our predictions for the SAG catalogues.
9: Same as 7 but for the SAGE catalogues
10: Same as 8 but for the SAGE catalogues

	R$_{max}$	t	flux lim	Applied ZoA	Treatment	SAG ζ^*	SAG σ_v	SAGE ζ^*	SAGE σ_v
	200	m_h	False	–	n/a	1.07±0.05	164.0±6.4	1.09±0.05	146.9±4.8
	200	L_K	False	–	n/a	1.04±0.04	159.0±5.9	1.04±0.04	141.3±4.2
A	200	L_K	True	–	n/a	1.03±0.03	160.5±6.2	1.04±0.03	145.9±4.1
C	200	N	True	–	n/a	0.99±0.05	163.9±6.3	0.99±0.06	147.5±4.6
	125	m_h	False	–	n/a	1.04±0.06	162.4±14.3	1.06±0.07	146.4±10.9
	125	L_K	False	–	n/a	1.04±0.05	157.7±12.9	1.04±0.05	141.5±8.9
B	125	L_K	True	–	n/a	1.03±0.06	159.7±12.4	1.04±0.05	145.2±8.9
D	125	N	True	–	n/a	0.97±0.07	163.2±11.9	0.99±0.06	146.8±8.3
	200	m_h	False	10°	cloned	1.0±0.05	170.5±7.1	1.02±0.05	154.0±5.8

	R$_{max}$	t	flux lim	Applied ZoA	Treatment	SAG ζ^*	SAG σ_v	SAGE ζ^*	SAGE σ_v
	200	L_K	False	10°	cloned	0.98±0.04	166.0±6.7	0.98±0.04	148.9±5.3
E	200	L_K	True	10°	cloned	0.97±0.04	167.7±7.1	0.98±0.04	153.4±5.2
G	200	N	True	10°	cloned	0.93±0.05	170.8±7.2	0.93±0.06	154.8±5.8
	200	m_h	False	10°	uniform	1.08±0.05	170.8±7.4	1.1±0.06	154.4±6.0
	200	L_K	False	10°	uniform	1.06±0.04	165.7±6.6	1.06±0.04	148.7±5.0
F	200	L_K	True	10°	uniform	1.05±0.04	167.3±6.9	1.06±0.04	153.2±4.9
H	200	N	True	10°	uniform	1.0±0.04	171.5±7.0	1.01±0.05	155.7±5.3
	125	m_h	False	5°	cloned	0.99±0.07	165.9±14.4	1.01±0.07	150.0±11.1
	125	L_K	False	5°	cloned	1.01±0.05	160.5±13.0	1.02±0.05	144.3±8.9
I	125	L_K	True	5°	cloned	1.0±0.06	162.6±12.6	1.01±0.05	148.2±8.7
K	125	N	True	5°	cloned	0.95±0.07	165.9±12.0	0.97±0.07	149.7±8.1
	125	m_h	False	5°	uniform	1.05±0.07	166.6±14.8	1.07±0.08	150.7±11.3
	125	L_K	False	5°	uniform	1.07±0.06	161.6±13.3	1.07±0.06	145.5±9.2
J	125	L_K	True	5°	uniform	1.05±0.07	163.8±13.2	1.07±0.06	149.3±9.3
L	125	N	True	5°	uniform	0.99±0.08	168.6±13.2	1.01±0.07	152.6±9.6
	200	m_h	False	2M++	cloned	1.05±0.06	170.8±8.1	1.06±0.06	153.9±6.7
	200	L_K	False	2M++	cloned	1.03±0.05	165.2±7.8	1.03±0.05	148.4±6.2
M	**200**	L_K	**True**	**2M++**	**cloned**	**1.03±0.05**	**166.9±7.7**	**1.04±0.05**	**152.8±5.7**
O	200	N	True	2M++	cloned	0.97±0.06	171.6±7.6	0.98±0.06	155.7±5.7
	200	m_h	False	2M++	uniform	1.08±0.06	171.0±8.3	1.1±0.06	154.1±6.8
	200	L_K	False	2M++	uniform	1.06±0.04	165.6±7.7	1.06±0.04	148.8±6.0
N	200	L_K	True	2M++	uniform	1.07±0.04	167.0±7.7	1.07±0.05	153.1±5.6
P	200	N	True	2M++	uniform	1.01±0.05	172.0±7.8	1.01±0.05	156.3±5.9

Table 4.2: Column and row separations have the same meaning as in Table 4.1, except here we show our measurements of $\zeta^\dagger = \beta_{\mathrm{norm,t}}/f/\sigma_{8,\mathrm{m}}$ for the flux limited density tracers only.

	R$_{max}$ t	flux lim	Applied ZoA	Treatment	SAG ζ^*	SAG σ_v	SAGE ζ^*	SAGE σ_v
	200 L_k	True	–	n/a	1.05±0.03	161.1±6.0	1.05±0.03	146.7±4.2
	200 N	True	–	n/a	1.0±0.06	164.4±6.5	1.0±0.06	148.3±4.8
	125 L_k	True	–	n/a	1.06±0.06	159.6±12.7	1.06±0.05	145.4±8.8
	125 N	True	–	n/a	1.0±0.09	163.0±12.4	1.02±0.07	146.9±8.7
	200 L_k	True	10°	cloned	0.99±0.04	167.9±7.0	0.99±0.04	153.9±5.3
	200 N	True	10°	cloned	0.94±0.06	171.0±7.4	0.94±0.07	155.4±5.9
	200 L_k	True	10°	uniform	1.08±0.04	167.6±6.9	1.08±0.04	153.7±5.0
	200 N	True	10°	uniform	1.03±0.05	171.6±7.2	1.03±0.05	156.0±5.4
	125 L_k	True	5°	cloned	1.03±0.06	162.7±12.7	1.03±0.05	148.5±8.6
	125 N	True	5°	cloned	0.98±0.09	165.9±12.5	0.99±0.08	150.0±8.3
	125 L_k	True	5°	uniform	1.08±0.07	163.6±13.1	1.09±0.06	149.4±9.0
	125 N	True	5°	uniform	1.03±0.09	168.1±13.3	1.04±0.08	152.3±9.4
Q	**200 L_k**	**True**	**2M++**	**cloned**	**1.04±0.05**	**167.6±7.7**	**1.04±0.05**	**153.6±5.9**
S	200 N	True	2M++	cloned	.98±0.07	172.3±8.0	0.98±0.07	156.4±6.0
R	200 L_k	True	2M++	uniform	1.08±0.05	167.4±7.7	1.08±0.05	153.5±5.7
T	200 N	True	2M++	uniform	1.02±0.05	172.1±8.0	1.02±0.05	156.5±6.1

4.7 Impacts on Previous Results

4.7.1 Corrected Measurements of β and $f\sigma_8$

Having carefully calibrated the bias $\zeta^\dagger$ as a function distance, and its cosmic variance, we can use this to re-calibrate previous results that have used 2M++ to estimate

$$f\sigma_8 = \beta_{\mathrm{norm}}/\zeta^\dagger \,. \tag{4.12}$$

We focus on two of the most recent of such studies, namely Boruah et al. (2020) and Said et al. (2020). We divide the peculiar velocity data used Boruah et al. (2020) into four subsamples: one of Type Ia supernovae (labelled "A2" in that paper), and three Tully-Fisher-based subsamples (SFI Field galaxies, SFI group galaxies and 2MTF galaxies). Likewise, we divide that in Said et al. (2020) into two Fundamental Plane (FP) samples (labelled 6dF and SDSS). The mean corrections for each of these six subsamples are small: when weighting these samples in the same way as is done when fitting the peculiar velocity data, we find weighted-average values of $\zeta^{\dagger} = 1.01, 1.01, 1.01, 1.01, 1.04, 1.04$ for the six subsamples respectively. After making these corrections, we can re-derive new, bias-corrected values of β for each sample.

To combine these to yield $f\sigma_8$ is more difficult, because in general they are not completely independent. The peculiar velocity measurement errors on the individual β values are independent, but when placed into the cosmic context and converted to values of $f\sigma_8$ it becomes more complicated. As discussed in Chapter 3, the uncertainty in the value of $f\sigma_8$ is driven primarily by the finite volume of 2M++ and cosmic variance. In particular, the density fluctuations are normalised within the 2M++ volume (effectively a sphere of 150 Mpc/h). If, for example, the 2M++ volume happened to be under-dense compared to the true mean density, then the local value of $\bar{\rho}$ would be too low, resulting in derived (locally-normalised) values of δ that are too high, leading to a fitted β that is too low for our "local" sphere. Moreover, because of sample variance, the local σ_8 may also differ from the global one. The 2M++ mocks are embedded in a 1 h^{-1}Gpc simulation box, so the variations in local mean density and σ_8 will be captured in the mocks, as will the effects of shot noise and ZoA cuts. Table 4.2 shows that for both SAMs, the standard deviation from mock-to-mock is 5%. In C15, this was estimated at 4% from the scatter in different shells, in reasonable agreement. This is the dominant source of error in $f\sigma_8$. But in addition, because the individual peculiar velocities sample different parts of the local sphere there is additional sample variance. For example, the Boruah et al. (2020) samples cover the sky outside the ZoA but are relatively shallow, with characteristic depths ranging from 22 to 40 h^{-1}Mpc. On the other hand the FP samples in Said et al. (2020) are deeper (typically 100 h^{-1}Mpc) but cover different parts of the sky (the southern hemisphere in the case of 6dF, and a smaller 1 steradian cap in the North for SDSS). When we compare these we find variations in β that are larger than just the measurement errors. We attribute this to sample variance effects.

We consider three different methods for combining these measurements. The first method is to include an additional error in quadrature so that the χ^2 of the weighted mean β of the six samples is equal to the number of degrees of freedom (5). This method yields $\beta = 0.390 \pm 0.024$. A separate method is to "jackknife" over the six surveys, which yields $\beta = 0.402 \pm 0.022$. Finally, we estimate the covariance of the individual β measurements using the mocks. This yields 0.402 ± 0.023. These three methods are in good agreement with each other in terms of their mean values and uncertainties. We adopt a best estimate of $f\sigma_8 = 0.398 \pm 0.025$.

The above result is the non-linear value of σ_8. To compare with cosmological models, it is better to have the linear value of σ_8. In previous work, we used the prescription of Juszkiewicz et al. (2010), which is based on 2nd-order perturbation theory, to correct from the non-linear σ_8 to the appropriate linear value. Here instead we use `halofit` (Smith et al., 2003; Takahashi et al., 2012) which better matches the measured particle σ_8 in MDPL2 (see Section 4.2.1). With `halofit`, we obtain a larger correction and hence a lower $f\sigma_8^{\mathrm{lin}} = 0.362 \pm 0.023$.

Our value of $f\sigma_8^{\mathrm{lin}}$ is in good agreement with that of Lilow & Nusser (2021), who found $f\sigma_8^{\mathrm{lin}} = 0.367 \pm 0.060$ using the density field from the slightly shallower 2MRS survey (Huchra et al., 2012), the Cosmic-Flows 4 peculiar velocity compilation (Tully et al., 2023) and which uses a different method for comparing the fields.

Assuming ΛCDM, our result translates to $S_8 \equiv (\Omega_{\mathrm{m}}/0.3)^{0.5}\sigma_8^{\mathrm{lin}} = 0.702 \pm 0.044$. which deviates from the Planck Collaboration et al. (2020b) result at the 2.8σ significance level, but is in agreement with the lower measurements from weak gravitational lensing (Heymans et al., 2013, 2021; Abbott et al., 2022).

Alternatively, if we assume that the growth index γ differs from ΛCDM but that Planck Collaboration et al. (2020b) measurements are correct for high redshifts, and our values are accurate at low redshifts, then our fits require $\gamma = 0.699 \pm 0.057$, a 2.6σ deviation from the ΛCDM expectation, $\gamma = 0.55$.

4.7.2 External Bulk Flows

It is expected that, as peculiar velocity surveys extend to larger and larger scales, the bulk flow of the surveyed volume, with respect to the rest frame defined by the CMB, will approach zero. The degree to which it converges as a function of volume, however, is a measure of the power spectrum on large scales. Over the last 15 years, there have been a number of studies of the bulk flow: some of these have found bulk flows higher than expected in ΛCDM, while others have not found any statistically significant discrepancy. These studies simply take a weighted average of the measured peculiar velocities.

The quantity measured in this work, however, is the residual or external bulk flow, $\boldsymbol{V}_{\mathrm{ext}}$ (see Eqn. 4.7). In principle, this can also be used to assess the power spectrum on scales larger than the survey limit, but the interpretation is more complicated than for a simple bulk flow. If the density field had had a simple geometry, such as a sphere, and no noise, it would have been straightforward to calculate the cosmological expectation the external bulk flow. For example, for a 200 h^{-1}Mpc sphere, and for a ΛCDM model scaled to $\sigma_8 = 0.8$, Hudson et al. (2001) found ~ 40 km s^{-1} in each Cartesian component. In the presence of an unusual geometry and noise, however, we must use the mocks to assess a range of external bulk flows that are expected.

In Figure 4.10, we show the measured external bulk flow from our mock catalogues, again excluding the outer 20 h^{-1}Mpc edges where predictions are heavily influenced by the lack of structure outside of survey limits. The black line shows the external bulk flow calculated in C15. The blue histogram shows the absolute magnitude of the external bulk flow, calculated from our $\zeta^{\dagger}$ values, while the orange histograms show the measured Cartesian components. For comparison the hatched values show the measurements of ζ^{*}. The standard deviations of the Galactic Cartesian components external velocity flows using the $\zeta^{\dagger}$ method are respectively 60, 56 and 54 for the X, Y and Z components. As expected, since the missing structure is in the Galactic plane, the standard deviation of the Z component is smaller than that of the X and Y components which are of the same order due to symmetry.

It is interesting to check whether the observed external bulk flow found by C15 is consistent with the expectation from ΛCDM. In ΛCDM, we expect the ensemble of such spheres to have a mean of zero, but with a standard deviation that we can calculate from the mocks as discussed above. Combining the individual Cartesian components' observational error from C15 (their Table 3) and adding the observational uncertainties in quadrature with the cosmic standard deviation, we obtain a $\chi^2 = 6.4$, which, when compared with the distribution with 3 degrees of freedom (for the 3 Cartesian components), yields a p-value of 0.094. This is below the threshold of what might be considered marginally significant. Repeating this exercise for the external bulk flows found by Boruah et al. (2020), and for the 6dF and SDSS subsamples in Said et al. (2020), we find p-values of 0.06, 0.08 and 0.03, respectively. Of course, the external bulk flows from each of these samples are, to first order, responding to the same large-scale structures beyond the 2M++ volume and so are not independent, but are highly correlated. Overall, there is therefore no conflict between the external bulk flows measured by these surveys and the expectations of ΛCDM.

4.8 Summary and Discussion

Using the MDPL2 N-Body simulation and SAM stellar masses, we generated 15 independent K-band mock catalogues, from both SAG and SAGE. Then from each of these mocks, we generate catalogues with orthogonal rotations which mimic the selection and geometry of 2M++. We constructed galaxy density fields of within 200 h^{-1}Mpc and, under the assumption of linear perturbation theory, predicted the peculiar velocities, which we then compared to the true known velocities from the simulation. The key results are as follows:

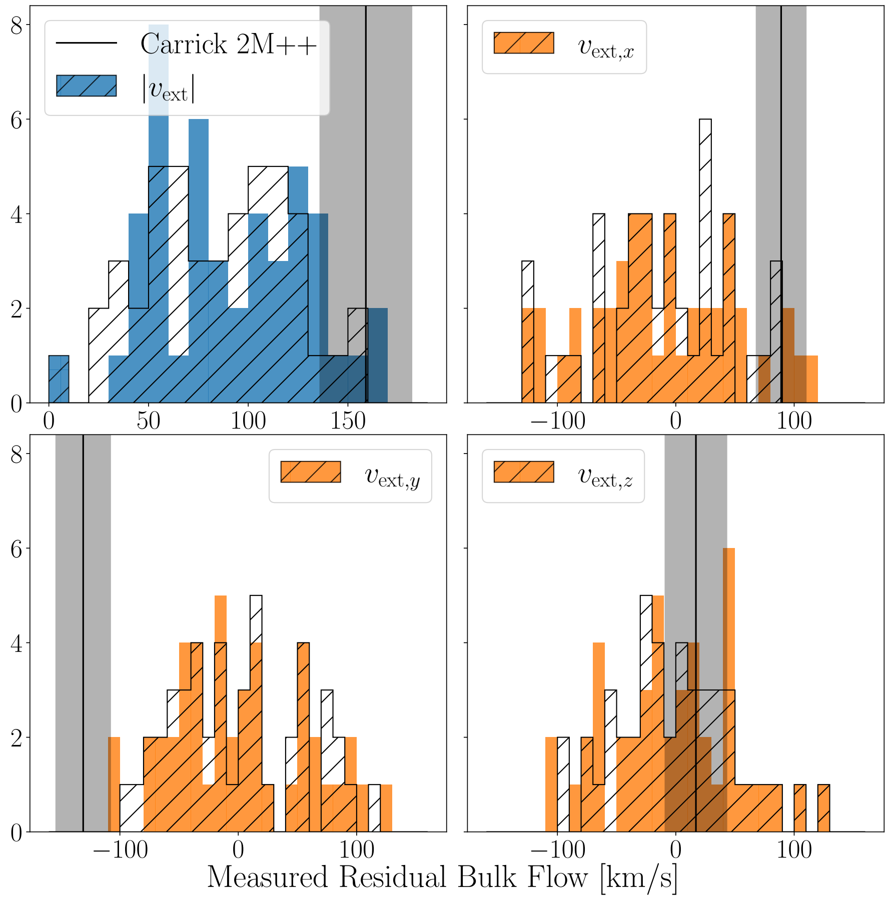

Figure 4.10: Top left: Shown in blue is a histogram of the magnitude of the measured $\zeta^\dagger$ residual bulk flow of the for the mock catalogues with the full 2M++ conditions imposed, the hatched histogram overlaid shows the same calculation performed instead by ζ^*. The black vertical bar with grey error bands serves as a comparison to the measured 2M++ value from C15. The orange histograms show the individual Cartesian components of the external flow. The Z-component demonstrates slightly less variance because it is less affected by the cloning of the ZoA.

- We find that the predicted peculiar velocities for galaxies located within 20 h^{-1}Mpc of survey edges are less accurate (the velocity scatter in this region increases by ~ 75 km s^{-1}), impacting measurements of β and reducing it by $20-30\%$. Away from the survey edges, however, the predictions work well.

- Overall, we find that both the cloned and uniform treatments for the ZoA affect the recovered measurements of β. However the globally the cloning treatment performs marginally better. We find that original predicted values are effectively recovered to within 5% for Galactic latitudes beyond twice the size of the applied ZoA.

- The results for $\zeta^*$and $\zeta^\dagger$ calculated using the same flux limited tracers for the velocity field, are summarised in Tables 4.1 and 4.2. Measurements of $\zeta^*$and $\zeta^\dagger$ remain fairly constant across radial shell measurements, with the exception of the measurements made within $\leq 20h^{-1}$ Mpc of the survey edges.

- The systematic bias in β for the ensemble of our 2M++-like mocks has been calibrated to a 1% uncertainty. However, due to cosmic variance, the uncertainty for any single mock and for the real 2M++ is 5%.

- We find that the velocity scatter, $\sigma_{\rm v}$, of 150 km s^{-1} adopted in C15 is slightly lower than the global measured scatter of 167 ± 8 km s^{-1} for 2M++, but the predicted scatter is heavily influenced by both the distance to survey edge and proximity to the ZoA.

- In Chapter 3 we predicted that cosmic variance would impact measurements of $f\sigma_8$ for a survey of 2M++'s size at the level of 5%. Here we find consistent results. This can be mitigated with future deeper redshift surveys which probe larger volumes. The larger volumes have two advantages. First, their local mean density will have smaller fluctuations with respect to the global mean density. Second, the larger volumes will allow a better calibration of the local value of $\sigma_{8,\rm g}$.

- The measured external bulk flow for C15 is consistent if slightly on the higher end of the measurements made solely due to cosmic variance. We note that the presence of the non-negligible external bulk flows are a result of the depth of 2M++.

- Having calibrated the small bias of this method, we find $f\sigma_8^{\rm lin} = 0.362 \pm 0.023$, or equivalently $S_8 = 0.702 \pm 0.044$, combining previous measurements based on 2M++ predicted peculiar velocities. This is lower than the predictions from Planck but in agreement with other peculiar velocity work and other techniques such as weak gravitational lensing.

Chapter 5

The Impact of Accurate Peculiar Velocity Corrections on H_0

This chapter investigates the impact of supernovae peculiar velocities on the inferred measurement of the local Universe's expansion rate. Supernovae redshifts used to calculate recent measurements of the Hubble constant (H_0) are dependent on predicted peculiar velocities derived from the 2M++ density field to correct observed redshifts. However to date, there has been no analysis preformed which quantifies how well we are able to reconstruct the true redshifts from the 2M++ survey nor the extent to which this impacts measurements of H_0. Using our mock 2M++ galaxy catalogues (described in Chapter 4), we are able to directly quantify the uncertainty in local H_0 measurements caused as a result of reconstruction errors and cosmic variance.

5.1 Introduction

The Hubble Constant, H_0, provides a measure of the local Universe's expansion rate. Significant effort has been dedicated to measuring H_0 over the past century. Modern measurements primarily rely on two main techniques. The first technique involves "local" measurements, which use nearby distance measures and extend up to redshifts of around $z \sim 0.40$ to estimate H_0. Assuming a standard cosmological model, the second technique involves "global" measurements, where H_0 is determined alongside other cosmological parameters by fitting large-scale features of the Universe such as the cosmic microwave background (CMB) (Planck Collaboration et al., 2020b) or baryon acoustic oscillations (BAO)

(Pogosian et al., 2020). Since the groundbreaking study by Riess et al. (2016) (hereafter R16), which achieved a local determination of the Hubble parameter with an uncertainty of 2.4%, there has been a growing tension between this value and the Planck value based on ΛCDM. This tension, known as the "H_0 tension", initially started at a difference of 3.4σ (R16) but has steadily increased to now reach a statistical significance of 5.0σ (Riess et al. (2022), hereafter R22).

Comparing measurements at opposite ends of the observable expansion history of the Universe provides a rigorous test for evaluating the standard cosmological model. Local measurements involve techniques such as the distance ladder, which extends to Type Ia Supernovae (SNe Ia) calibrated through geometric distances and Cepheid variables. Other local measurement methods include using the tip of the red giant branch (TRGB) (e.g., Freedman, 2021; Scolnic et al., 2023) or using gravitational waves as standard siren measurements (e.g., Abbott et al., 2021). While global measurements include observations of large-scale structure, using standard ruler methods (i.e. BAO or CMB) and lensing (e.g., Alam et al., 2021; Planck Collaboration et al., 2020b; DES Collaboration et al., 2023).

A significant discrepancy would indicate evidence for fundamental physics beyond what is predicted by the standard model. This could include phenomena such as time-dependent or early dark energy, gravitational effects that go beyond General Relativity, additional relativistic particles in existence, or non-zero curvature (see Abdalla et al., 2022, for a comprehensive review). Currently, none of these possibilities have been definitively ruled out based on more compelling evidence than theoretical preferences favouring simplicity over complexity. Despite this discrepancy, it is worth noting that 'local' measurements of H_0 from diverse experiments, conducted at various redshifts, remarkably agree with each other. This agreement is particularly noteworthy considering that ΛCDM, which assumes our Universe can be described by a cosmological constant and cold dark matter, has enjoyed immense success. Nevertheless, these developments bring us closer to questioning whether slight adjustments may be necessary in our standard model of cosmology in order to address this tension effectively.

5.1.1 Peculiar Velocities and H_0

One of the factors that impacts local measurements of H_0 is that of peculiar velocities, as they perturb cosmological redshifts, introducing uncertainty in determining the Hubble constant from low-redshift distance indicators. To remove this distortion, a correction is applied based on a modelled peculiar velocity field (Willick & Batra, 2001; Boruah et al., 2021). Hence accurate reconstructions of this peculiar velocity field from observed large-scale structures are essential for reliable inference of H_0. In the linear regime it is possible to relate the peculiar velocity field to the underlying density field via Eqn. 2.15. There are three caveats to this equation:

1. Galaxy surveys are unable to directly measure the total matter density. As a result it is typically assumed that there is a linear relation between the observed galaxy density field and the total matter density field, such that $\delta_g = b\delta$. This linear biasing term (b) is dependent on a number of factors, such as observable type, and hence must with be marginalised over or directly measured.
2. The integral presented in Eqn. 2.15 is over all space, however galaxy surveys are finite due to instrument limitations. As such, our reconstructed density fields are insufficient to fully encapsulate the motions of galaxies, this is typically addressed through the estimation of external velocity flows. This value accounts for structure beyond survey limits and theoretically, with a large enough survey, decays to zero.
3. The density fluctuations are normalised within a finite volume, which impacts the predictions of peculiar velocities.

Density field reconstruction combined with observations allows for the determination of the scale parameter β and residual mean velocity $\mathbf{V}_{\rm ext}$. The reconstruction process generates a *normalised* peculiar velocity field, $\mathbf{v}_{\rm pred,c}(\mathbf{r})$, which reveals information about directions and magnitudes of peculiar velocities at different positions. These predictions are compared to galaxies with their own estimated peculiar velocities using distance measures like the Tully-Fisher or Fundamental Plane relations. Adjustments are made to align this calibrated peculiar velocity field accurately with observed galaxy velocities for improved accuracy.

5.1.2 Reconstructing Cosmological Redshifts

At low redshifts ($z < 0.1$) the uncertainties in $z_{\rm cosmo}$ are primarily attributed to two sources: uncertainties in measurements and peculiar velocities. This is because an object's cosmological redshift ($z_{\rm cosmo}$) cannot be measured directly, rather it must be inferred from the observed redshift after it has been corrected to be in the CMB rest-frame ($z_{\rm CMB}$), using the peculiar redshift approximated by $z_{\rm pec} = v_{\rm pec}/c$ (the non-relativistic doppler-shift approximation as $v_{\rm pec} \ll c$). The two quantities can then be related using

$$z_{\rm cosmo} = \frac{1 + z_{\rm CMB}}{1 + z_{\rm pec}} - 1\,. \tag{5.1}$$

We define our reconstructed cosmological redshifts ($z_{\rm rec}$) as

$$z_{\rm rec} = \frac{(1+z_{\rm cosmo})(1+z_{\rm pec})}{(1+z_{\rm pred,c})} - 1\,, \tag{5.2}$$

where

$$z_{\rm pred,c} \approx \frac{v_{\rm pred,c}}{c} = \frac{\beta v_{\rm pred} + \mathbf{V}_{\rm ext}\cdot\hat{\mathbf{r}}}{c}\,. \tag{5.3}$$

Recent cosmological analyses using SNe Ia data have incorporated peculiar velocity predictions from reconstructed density fields.However, errors in these reconstructions can introduce both statistical uncertainties and systematic biases to measurements related to cosmic growth and expansion. Various efforts have gone into trying to understand the influence of systematic uncertainties in peculiar velocity measurements and are considered in analyses measuring w with SNe.

R16 examined the impact of peculiar velocity corrections on H_0 measurements by comparing a minimal redshift cut of $z = 0.01$ against that of $z = 0.023$ for their sample. They found that using the latter cut reduced sensitivity to peculiar velocities, finding a difference in the recovered value of H_0 of 0.3 km s^{-1} Mpc^{-1}. Scolnic et al. (2018) varied β by 10% and found an uncertainty of 0.003 in w due to coherent flow corrections, and the omission of peculiar velocity corrections led to a shift in w by 0.009. Brout et al. (2019) found that uncertainties in redshifts due to coherent flow corrections resulted in contributing a systematic uncertainty of 0.007 to w. Peterson et al. (2022) investigated the impact of large-scale coherent motion and small-scale virial motion of galaxies within groups, correcting for the peculiar motion of both, impacted their measure of H_0 by 0.06-0.11 km s^{-1} Mpc^{-1}. However to date, the impact of peculiar velocity reconstruction and its application to the SNe in the Riess papers has not been quantified.

Understanding the errors inherent in reconstructing the peculiar velocity field is vital as it affects our ability to make precise cosmological predictions based on observed large-scale structures. In this chapter, we propose a novel model for characterising these error distributions and conduct an initial analysis of their impact on associated measurements of the expansion rate. Here we determine the impact of how well we are able to correct for peculiar velocities in our determination of the recovered cosmological redshift, and the extent up which this impacts the uncertainty on the overall measurement of H_0.

Effects of an Underdense Local Universe

There have been several observations, performed at multiple wavelengths, which find supporting evidence that there is a large local under-density around the Local Group. Initially it was observed in optical samples as a deficiency in the galaxy luminosity density (Maddox et al., 1990), which estimated that the local under-density spanned a region out to a distance of $\sim 140\ h^{-1}$Mpc, using ESO Slice Project galaxy survey data taken in the b_j-band (Zucca et al., 1997). X-ray galaxy cluster surveys such as REFLEX II (Böhringer et al., 2015) and CLASSIX (Böhringer et al., 2020) also find an apparent local Universe under-density. The latter (former) found an average underdensity of 20–30% (30–40%) under-density within a radius of $\sim$ 140 Mpc (170 Mpc) in the matter distribution. Additionally multiple studies focusing on data from near-infrared surveys have found that the under-density extends to even larger radii measuring it to scales of 200-300 h^{-1}Mpc (Frith et al., 2003; Busswell et al., 2004; Frith et al., 2006; Keenan et al., 2013; Whitbourn & Shanks, 2014; Hoscheit & Barger, 2018; Haslbauer et al., 2020; Wong et al., 2022). However, whether or not we exist within a local under-density is still controversial. Jasche & Lavaux (2019), using the 2M++ Catalogue, studied the distribution of galaxies and found that local structures could be explained within the ΛCDM framework and found no evidence for an under-density on the proposed scales.

Regardless of its existence, a perturbation in our local matter density field, to first order, would generate a change in the local expansion rate as follows:

$$\frac{\Delta H_0}{H_0} = -\frac{1}{3} f(\Omega_m)\delta \tag{5.4}$$

(Turner et al., 1992). Here ΔH_0 represents a local shift in H_0, and δ is the *local* density contrast. From this it is clear that a local under-density, $\delta < 0$ would result in local expansion rate which is higher $\Delta H_0/H_0 > 0$. However, as we consider increasingly larger scales, these perturbations become smaller and their amplitude, which is constrained by observations of measurements of the power spectrum of matter density fluctuations, decreases. This results in a decrease in the density contrast which then tends to the homogeneous FLRW limit. It has been suggested that this cosmic variance on H_0 results in a systematic uncertainty of about $\sim$ 1% when analysing observations within the redshift range of $0.023 < z < 0.15$ (for more details see Camarena & Marra, 2018; Odderskov et al., 2017, and references therein). Despite this uncertainty, it falls short of explaining why there is a significant difference of around 8% between early-time and late-time H_0 constraints, which is impossible in ΛCDM.

Additionally Wu & Huterer (2017) investigated if sample variance in the local Universe could alleviate the Hubble tension. This was done using N-body simulations to model local measurements and quantified the variance as a result of these local Universe density fluctuations and sample selection. While they directly matched the cosmological redshifts of the Pan-STARRS SNe in their model, they did not account for host galaxies peculiar velocities. They estimated the local uncertainty of H_0 due to sample variance to be 0.31 km s^{-1} Mpc^{-1}. Kenworthy et al. (2019) find a consistent result with predicted cosmic variance of Wu & Huterer (2017). They used a SNe sample consisting of data from Pantheon, Foundation, and the Carnegie Supernova Project, and searched for evidence of a local void via the presence of large-scale outflows. They found no evidence to suggest the existence of a local large-scale underdensity within $0.023 < z < 0.15$ with a high confidence of $\sim 4 - 5\sigma$. The R16 and R22 papers explicitly correct for each SN's peculiar velocity using the reconstruction of the local 2M++ density field from (Carrick et al., 2015). This correction is normalised within the survey volume of 2M++. As a result if the entire region 2M++ region is under-dense, there would be a net change in the peculiar velocities, that is indistinguishable from a change in the Hubble constant, but this would not included in the 2M++ predictions. Additionally, the reconstruction of the density field is subject to wide range of systematic errors (see Chapter 4 for more details), hence still might require a partial correction for the sample variance.

In this chapter, we use our mock 2M++ redshift compilation catalogues (see Chapter 4.2 and 4.5 for details of the mock catalogues) which match the geometry and magnitude limits of the density field that was used to correct for the SNe peculiar velocities in R16 and R22. We do not use the actual 2M++ catalogue in this analysis as we are trying to determine the extent to which our predicted peculiar velocity methodology is able to reconstruct the true redshift. This is not possible without knowing the true peculiar velocity of the SNe, by using simulation data which matches surveys selection we are able to determine the extent to which the reconstruction impacts measurements of H_0 for the first time. Hence we are able to more fully understand the impacts these corrections take on the measurement of H_0.

5.2 Pantheon+ Catalogue

The Pantheon+ catalogue is the successor to the original Pantheon SN sample, and its analysis was a joint effort with the SH0ES team. Pantheon+ consists of 1701 measurements of 1550 SNe between $0.001 < z < 2.26$. Here we briefly review how the Hubble constant was measured in R22. The R22 measurement of the local H_0 uses distance anchors which have geometric measurements and hence precise distances. These anchors include independent calibration of Cepheids in NGC 4258 (a megamaser host), the Milky Way (from abundant parallax data), and the Large Magellanic Cloud (using detached eclipsing binaries). By using these anchors to calibrate μ^0 of host SNe galaxies. The distance ladder's second rung is composed of a set of 42 calibrators containing Cepheids and SNe; with the anchors setting the Cepheids' absolute distance. Within the distance ladder's third rung of Pantheon+, there is a subset of 277 SNe (located within the Hubble flow at $0.023 < z < 0.15$ limited to but not inclusive of all SNe within this redshift range) which we will refer to in this chapter as the SH0ES HF sample. The global fit of all these rungs, is the set of standard candles that are used to determine a measurement of H_0.

5.3 Constructing a Hubble Diagram

Standard candles, i.e. astrophysical objects which have a known luminosity, are often used to probe the Universe's expansion rate. Historically this is done using the redshifts and apparent luminosities of SNe Ia, which can be used to establish an empirical redshift-distance relation. The R22 measurement of the Hubble parameter is measured with a 3-rung distance ladder which employs a simultaneous singular fit between: 1) Cepheids which have been standardised via geometric measurements, 2) SNe Ia hosted by nearby galaxies with standardised Cepheids and 3) Hubble-flow SNe Ia. However, to estimate distances to SNe Ia one must assume that an object's absolute luminosity is the same as its local counterpart measurements, after applying corrections, the comparison of these values provides a measure of the distance modulus:

$$\mu_x^0 = m_x^0 - M_x^0 = 5\log_{10}\left(\frac{D_L(z)}{1\mathrm{Mpc}}\right) + 25\,. \tag{5.5}$$

where x denotes the wavelength band and the superscript 0 denotes a magnitude corrected for (or free of) any intervening absorption due to interstellar dust. One can also compute the luminosity distance D_L of a light source with redshift z in the context of General Relativity. Assuming a flat FLRW metric, one finds

$$D_L(z) = (1+z)c\int_0^z \frac{dz}{H(z)}\,, \tag{5.6}$$

where c is the speed of light and $H(z)$ is the Hubble function.

The Hubble function at relatively low redshifts ($z \ll 1$), can be usefully expressed as a series expansion approximation in redshift, resulting in

$$D_L(z) \approx \frac{cz}{H_0}\left[1 + \frac{z}{2}(1-q_0) - \frac{z^2}{6}(1 - q_0 - 3q_0^2 + j_0) + \mathcal{O}(z^3)\right] = \frac{cz}{H_0}\hat{d_L}(z)\,, \tag{5.7}$$

where $q_0 = -0.55$ and $j_0 = 1$ are the present deceleration and jerk parameters, and $\hat{d_L}(z)$ defines a function that approaches unity as z tends to 0.

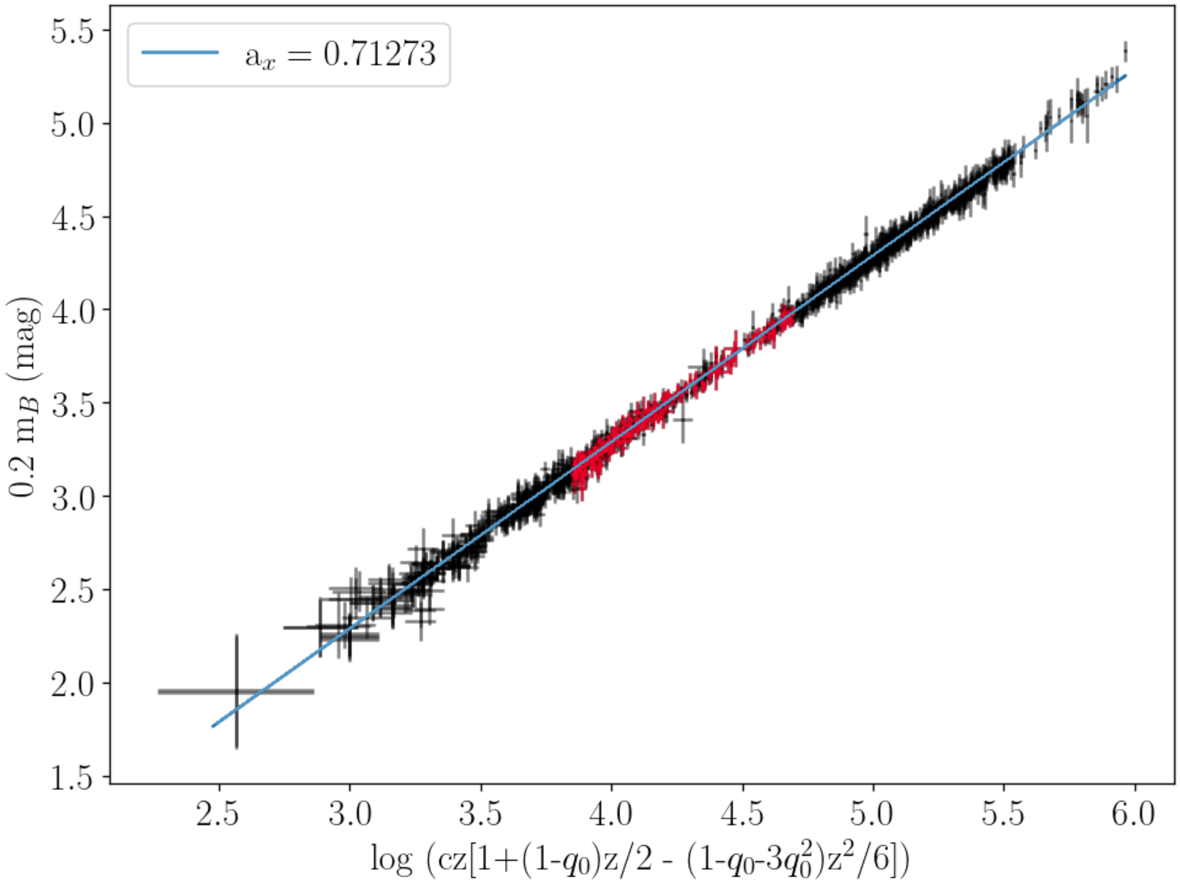

Figure 5.1: The full magnitude redshift Hubble diagram from the 1701 SNe in the Pantheon+ Catalogue. Shown in red are the 277 SNe Ia, used in the SH0ES Hubble Flow analysis ($0.0233 < z < 0.15$). The uncertainties shown for m_B are the standardised magnitude uncertainty derived from the covariance matrix diagonal. These data are used to determine the intercept of Eqn. 5.8, a_x, the global measurement from R22 is shown in blue.

Equating equations 5.5 and 5.7 and introducing a constant a_x defined to be the intercept of the magnitude-redshift relation:

$$a_x = \log cz\hat{d}_L(z) - \frac{m_x^0}{5}\,, \tag{5.8}$$

we can obtain an estimate of the Hubble constant that is solely reliant on two fitted parameters:

$$\log H_0 = \frac{M_x^0 + 5a_x + 25}{5}\,. \tag{5.9}$$

R22 used the B-band Hubble diagram for 277 of the SH0ES HF sample, performing a simultaneous fit to measure the intercept $a_B = 0.714479$ and $M_B = -19.246$. The measurements in R16 performed these fits independently and using the Hubble diagram for 217 SNe Ia in same the redshift range, R16 found $a_B = 0.71273 \pm 0.00176$.

It is obvious from Eqns. 5.7-5.9 that the overall uncertainty in H_0 is dependent on (1) the absolute calibration M_x^0, (2) uncertainties in SNe magnitudes and (3) the SNe's cosmological redshifts. The intercept a_x is determined from a Hubble diagram of SNe Ia where the individual measurements of m_x^0 are determined with a light curve fitter (Scolnic et al., 2022). While contributions in the overall uncertainty due to corrections performed (1) and (2) on the SNe's magnitudes have been explored in works (e.g., Carr et al., 2022; Peterson et al., 2022), we limit our focus in this chapter to the effects of (3).

5.3.1 Redshift Reconstruction

The Pantheon+ data of R22 provides a measure of objects' Hubble-diagram redshift, which is the peculiar velocity corrected CMB frame redshift. To avoid confusion we will refer to our mock galaxy catalogue redshifts as follows: $z_{\rm cosmo}$, the true cosmological redshift based on the comoving coordinates of our mock catalogues; $z_{\rm CMB}$, the "observed" CMB-frame redshifts after correcting $z_{\rm cosmo}$ by the true peculiar velocities; and $z_{\rm recon}$ the reconstruction of the cosmological redshifts from $z_{\rm CMB}$ after correcting for the predicted peculiar velocities' measured bulk flow and β.

As we are working with mock 2M++ catalogues, the physical location of the galaxies in the Pantheon+ catalogues do not have precise matches in the mocks. Our procedure for generating our reconstructed redshifts can be summarised as follows:

1. Each Pantheon+ SNe located within the volume of the 2M++ catalogue is matched to the nearest proxy central galaxy from our Chapter 4 catalogues. Any galaxy

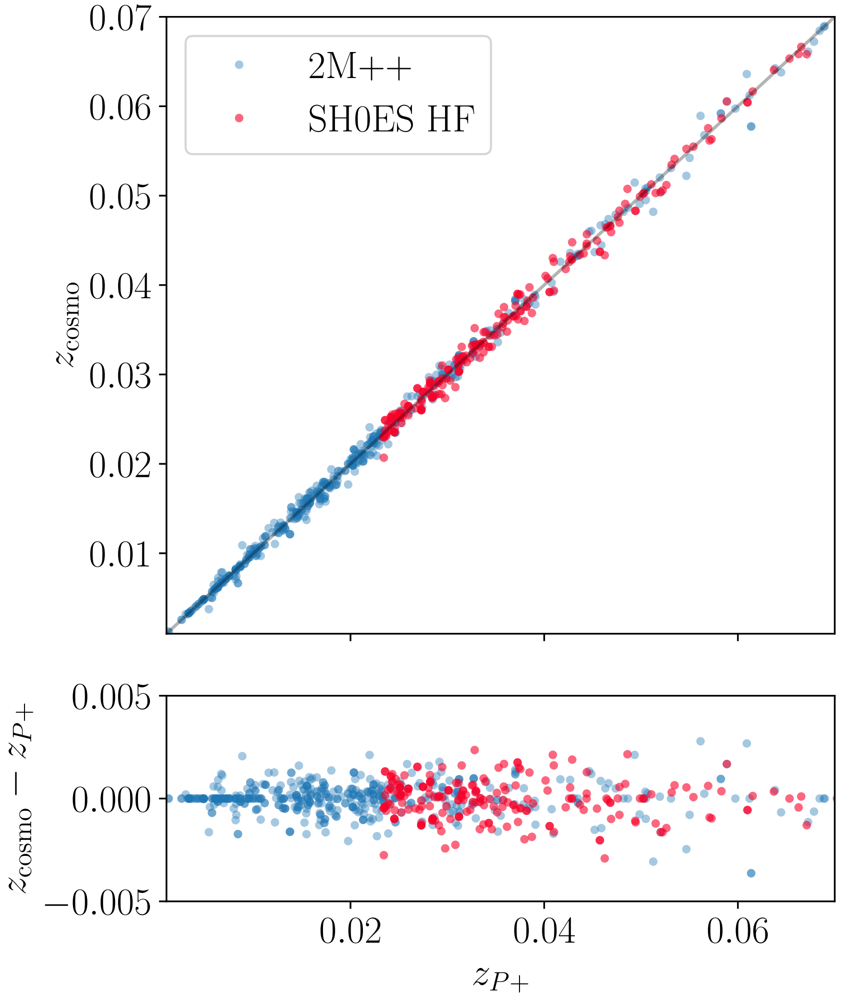

Figure 5.2: Difference between the Pantheon+ SNe (z_{P+}) cosmological redshifts against those derived from matching to their nearest galaxy counterparts from one of our mock 2M++ catalogues shown by the coloured markers. Here the markers show SNe Ia within 2M++ (blue), and the SH0ES HF SNe sample which are located in the redshift range $0.0233 < z < 0.15$ (red).

located outside the confines remains at its given Hubble Diagram redshift, we refer to these updated redshifts as z_{cosmo}. This results in a change in z for 203 galaxies in the SH0ES HF sample.

2. We correct each z_{cosmo} by the true radial peculiar velocity calculated from the N-Body simulations to obtain the redshift that would be observed from the centre of the survey volume, these are our CMB-frame redshifts, z_{CMB}.

3. We use the predicted peculiar velocities generated in Chapter 4 to correct z_{CMB} after fitting each mock for β and V_{ext}. For our purposes, we use the $\zeta^{\dagger}$ as was calculated for our mock catalogues. This reconstruction procedure gives z_{rec}.

As in the case of the true 2M++ density field, the peculiar velocity corrections are not perfect. The goal of this work is to determine how much uncertainty gets propagated due errors in the reconstruction of the peculiar velocities and uncertainties in the bulk flow. We keep consistent weighting throughout the entirety of this work using the covariance matrix presented in R22, because the choice of weights would also impact the final recovered value of the intercept a_x. We are interested in the difference in a_x measured from z_{cosmo} and that obtained using z_{rec}, and its scatter from mock-to-mock.

Figure 5.2, shows the difference between the redshifts from one of our mocks to the true cosmological redshifts of R22. We do not perform any changes to redshifts located outside of the 2M++ survey volume, nor to any objects treated as calibrators. This results in an average displacement of $\Delta z_{\mathrm{cosmo}} = 0.0011$ (320 km/s) from the R22 value.

Figure 5.3 shows the difference between z_{CMB} (left) and z_{recon} (right) against z_{cosmo}. This figure demonstrate the impact of peculiar velocities on the z_{cosmo} and how well we are able to reconstruct the cosmological redshift. The scatter generated solely due to peculiar velocities is on average $z \sim 0.00092$ (275 km s^{-1}), while, for the reconstruction, this is reduced to 0.00044 (132 km s^{-1}). The latter scatter is slightly less than $\sigma_v \sim 170$ km/s found in Chapter 4. The gray band shown on the bottom right panel of this figure is the 250 km s^{-1} uncertainty that is assumed for the R22 corrections. For visualisation purposes only, we show the predicted uncertainties from our results in Chapter 4.

5.3.2 Calculating Changes to a_x

Having generated z_{rec} we can now investigate the impact this has on the recovered value of a_x and hence H_0. For each mock catalogue we perform a weighted fit for a_x using the statistical and systematic covariance matrix provided by R22. We begin by reducing the

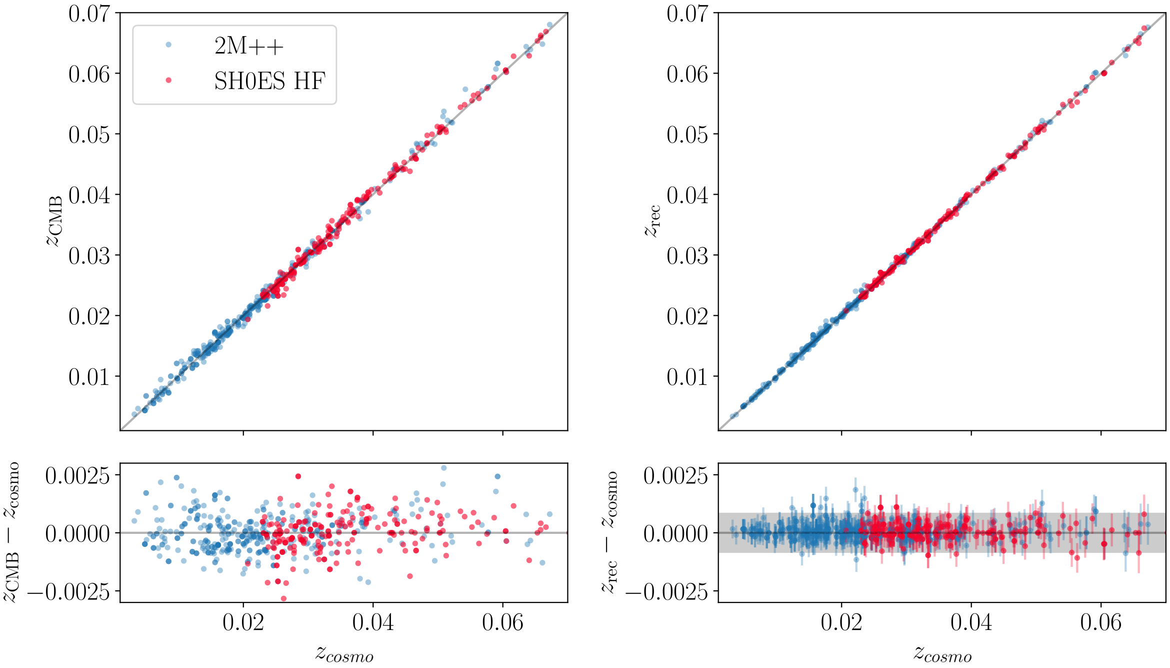

Figure 5.3: Top Left panel: Comparison between the 'observed' CMB frame redshift against $z_{\rm cosmo}$. Bottom Left panel: Shows the difference between $z_{\rm CMB}$ and $z_{\rm cosmo}$. Right Panel: Shows our reconstructed redshifts after accounting for external flows, peculiar velocities and β. Bottom Right Panel: shows the difference between $z_{\rm rec}$ and $z_{\rm cosmo}$. For comparison the 250 km $\rm s^{-1}$ assumed in R22 is show in the grey band while the uncertainty for our SNe mocks using our mocks is shown by the errorbars. We use the same mock here as in Figure 5.2.

full covariance matrix into one that only includes the SNe in the redshift range that we are investigating. We then perform a simple χ^2 minimisation procedure to determine the best value of a_x:

$$\chi^2(a_x) = \mathbf{\Delta}^T C^{-1} \mathbf{\Delta} \,, \tag{5.10}$$

where Δ is a vector of residuals of Eqn. 5.8. We perform this calculation for each of our redshift catalogues and compare the difference between the recovered a_x as determined from our $z_{\rm rec}$ and $z_{\rm CMB}$ against our $z_{\rm cosmo}$ values.

5.4 Results

Figure 5.3 shows a histogram of the differences between recovered a_x measurements of the 'observed' CMB frame redshifts (left) and the reconstructed redshift measurements (right) from the mocks' true cosmological redshift measurements of a_x. As demonstrated here for the SH0ES HF sample, the reconstruction reduces the uncertainty in the measurement of a_x such that $\sigma_{a_x}(z_{rec}) = 0.00121$, which is a factor of 2 reduction when compared to the case where $z_{\rm CMB}$ is used. We note that this standard deviation is being slightly ($\sim 10\%$) driven by one of our mocks which consistently under-predicts the peculiar velocities. We find that the reconstruction uncertainty for this sample would propagate into a measurement uncertainty of H_0 of 0.21 km s^{-1} Mpc^{-1}.

Of course this sample consists of a very limited number of SNe, with a not insignificant number lying beyond the survey limits of 2M++. As the measurement detailed above includes objects which for our purposes have no error this reduces the variance exhibited by a_x. If we remove these non-varying SNe from our calculations we find, as expected that the variance in a_x increases, however this increase is quite minimal and produces a value of $\sigma_{H_0}(z_{\rm rec}) \sim 0.31$ km s^{-1} Mpc^{-1}.

In Table 5.1 we show our a_x variance measurements for several redshift ranges that have been considered in the literature. We find that regardless of imposed minimum redshift cuts all measurements of $\sigma_{a_x}(z_{\rm rec})$ are very similar. The top portion of this table shows our measurements which include the non-varying redshifts of objects that lie outside of 2M++. While the bottom portion of the table explores the same minimum redshift cuts, but here we limit or sample to SNe lying within 2M++. Here we find, unsurprisingly, that a_x based on the CMB redshifts are more heavily impacted at lower redshifts due to the (uncorrected) peculiar velocities. We additionally find that using no corrections causes significant variation in the recovered a_x so that $\sigma_{H_0}(z_{CMB}) \sim 0.6 - 3$km s^{-1} Mpc^{-1}. However, we find that the reconstructions perform comparably well for all explored redshifts

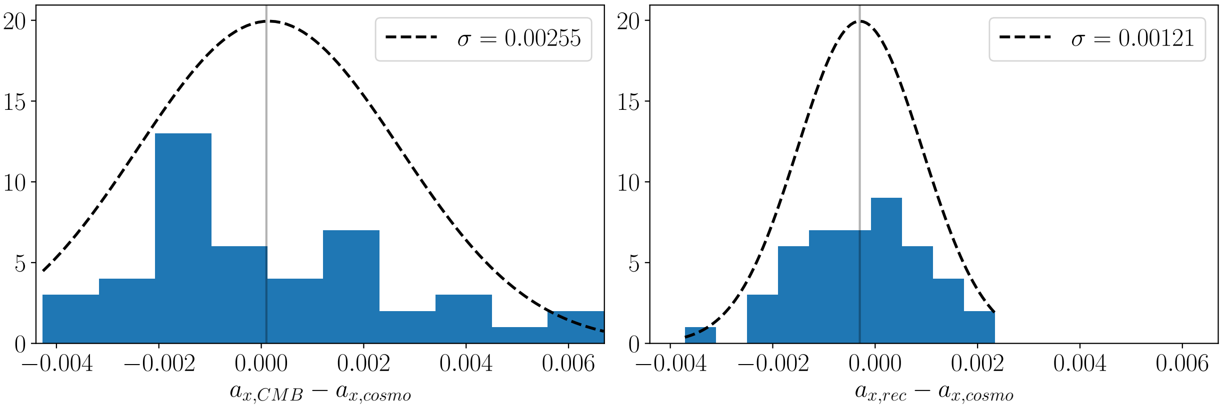

Figure 5.4: Histogram of the difference between a_x calculated directly from the cosmological redshifts and a_x calculated from the: (left) 'observed' CMB frame redshifts, and (right) reconstructed redshifts corrected by the predicted peculiar velocities for the SH0ES HF sample.

samples. In all cases we find that the reconstruction only slightly impact our recovered value of H_0 by ~ 0.30 km s^{-1} Mpc^{-1}.

5.5 Discussion and Conclusion

By using mock 2M++ density fields which mimic the selection effects of the reconstructed density field used in recent H_0 SNe analyses, we are able to directly measure the uncertainty introduced in measurements of the Hubble constant solely due to reconstruction errors. However, in this chapter we did not model any of scatter in cosmological redshift beyond the survey limits of 2M++. We assumed that objects that lie outside of the 2M++ volume had perfect measurements in their measured cosmological redshifts. This means that we are underestimating the uncertainty in our measurements of a_x. Therefore the uncertainty in H_0 of 0.3 km s^{-1} Mpc^{-1}that we present in this thesis should be considered a lower limit of the total uncertainty due to peculiar velocities.

Extending the SN sample to redshift 0, we find no discernible difference in the standard deviation of the recovered H_0 measurements. It should therefore be possible to include these objects with appropriate weights, as the scatter in the recovered a_x is only minimally affected by these low-redshift data. This is left for future work.

As the density field is normalised within the survey volume of 2M++, the peculiar ve-

Table 5.1: Comparison of the standard deviation in a_x with and without reconstructed peculiar velocity corrections. Shown here are the deviations in (1) a_x when using CMB redshifts (2) a_x from the reconstructed cosmological redshifts (3) the uncertainty in H_0 propagated from the variation in measurements of $\sigma_{a_x}(z_{\rm rec})$.

redshift range	N	$\sigma_{a_x}(z_{\rm CMB})$	$\sigma_{a_x}(z_{\rm rec})$	σ_{H_0} [km s^{-1} Mpc^{-1}]
SH0ES HF all	277	0.00255	0.00121	0.20
$0.0233 < z < 0.15$	490	0.00229	0.00105	0.18
$0.01 < z < 0.15$	715	0.00319	0.00115	0.19
SH0ES HF in 2M++	203	0.00338	0.00182	0.31
$0.023 < z$ and in 2M++	335	0.00377	.00174	0.29
$0.01 < z$ and in 2M++	558	0.0047	0.00179	0.30
$z < 0.068$ and in 2M++	601	0.0175	0.00177	0.30

locity predictions generated using this field would not account for any local under-densities on the scale of 200 h^{-1}Mpc or larger. Any such large-scale local density fluctuation would manifest as a systematic error in the predicted velocities compared to the true velocities. Thus our mock catalogues are only able to capture this effect on 2M++ scales, and effects due to large-scales are unaccounted for. While we do not explore the how large-scale local density fluctuations impacts measurements, this has been done by Wu & Huterer (2017). Their method is capable of capturing these large-scale effects but, since it does not include reconstruction with 200 h^{-1}Mpc, overestimates the uncertainty. They claim an upper limit on the uncertainty due to sample variances to be 0.31 km s^{-1} Mpc^{-1}. This value is almost identical to the lower limit we estimate for the reconstruction uncertainties. Therefore we expect that the 0.3 km s^{-1} Mpc^{-1}to be an adequate representation of the uncertainty contributed due to peculiar velocities of SNe Ia within 2M++ and beyond.

We find that the uncertainty in H_0 arising from peculiar velocities is estimated to be $\sim$ 0.3 km s^{-1} Mpc^{-1}, hence can only account for a small part in the overall uncertainty and cannot appreciably alleviate the H_0 tension.

Chapter 6

Conclusions and Future Directions

6.1 Conclusions

Peculiar velocities are crucial cosmological probes, as their measurements provide unique insights into the distribution of matter in our universe, particularly at low redshifts where other observational techniques are limited or less accurate. By studying these deviations from the overall cosmic expansion, we can gain valuable information about large-scale structures and test different cosmological models. This thesis explored the systematics and biases introduced in the recovery of cosmological parameters when performing velocity-velocity comparisons. We used N-Body simulations and semi-analytic models of galaxies to test a variety of factors.

In Chapter 3 we investigated several technical aspects that could affect the accuracy and reliability of this method. One aspect examined is determining the optimal smoothing length applied to the density field. We find that assuming linear theory the velocities of haloes are well predicted on scales of 4 h^{-1}Mpc, in agreement with other works and on the same order as the cross-correlation function between the density and velocity fields. We investigated potential sources of error such as noise in halo mass estimates and uncertainties in relating stellar-to-halo mass ratios, we found this impacted measurements on the level of 0.5% and 5%, respectively. We also demonstrated the extent to which finite survey volumes impact measurements, as limited data sets introduce cosmic variance - statistical fluctuations due to sampling effects - which would impact a survey with the volume of 2M++ at 5.2%.

In Chapter 4 we expanded upon these results by analysing the systematics introduced due to the various conditions imposed within the framework of the 2M++ survey compilation. This was done by creating 15 independent K-band mock catalogues using both the SAG and SAGE SAMs. From each of these, we generated two additional catalogues with orthogonal rotations that replicate the selection criteria and geometry of the 2M++ survey. We examined the additional uncertainties that arise from survey selection effects, such as flux-limitations and obscuration due to the Galactic plane, and investigated how these impact measurements of cosmological parameters. We primarily focused on weighting the density based on the "observed" K-band luminosity of our mock catalogues to determine the effect on inferred parameters such as β.

We determined that edge effects impact the recovered value of β by $20-30\%$, for galaxies located within 20 h^{-1}Mpc of survey limits and generate an additional velocity scatter of ~ 75 km s^{-1}). We found that the cloning treatment applied to the ZoA performs marginally better globally than the uniform case. Additionally, we determined how the recovered β measurements are impacted as a function of Galactic latitude and found that the original values of β are effectively recovered to within 5% at Galactic latitudes beyond twice the size of the applied ZoA. We confirm our Chapter 3 predictions that the cosmic variance experienced by a 2M++-like survey is at the level of 5%. The systematic bias in $f\sigma_8$ for the ensemble of our 2M++-like mocks has been calibrated to a 1% uncertainty. We found that the velocity scatter of 150 km s^{-1}used in Carrick et al. (2015) is lower than the globally measured value of 167 km s^{-1}. This is heavily dependent of the distance to the survey limit and from the Galactic plane, however. After calibrating the slight bias of this method, we obtain a value of $f\sigma_8^{\text{lin}} = 0.362 \pm 0.023$, derived by combining previous measurements that rely on predicted peculiar velocities from the 2M++ survey data set. Our results are lower than what is predicted by Planck but align with other studies involving peculiar velocity analysis and alternative techniques like weak gravitational lensing.

Finally, in Chapter 5 we used our mock 2M++ catalogues to determine the uncertainty associated with the reconstruction of cosmological redshifts using peculiar velocity predictions. We find that the uncertainty propagates into a lower limit uncertainty for the local Hubble parameter of 0.30 km s^{-1} Mpc^{-1}, which is comparable to the upper limits calculated in previous work. We also find that the scatter generated in these predictions does not increase even if we extend the SN sample to lower redshifts than those used by SH0ES. Our analysis reveals that the uncertainty in H_0 resulting from peculiar velocities, represents only a small portion of the total uncertainty and unable to significantly alleviate the H_0 tension.

6.1.1 Future Directions

In Chapters 3-4 we predicted and then confirmed that cosmic variance impacts measurements of $f\sigma_8$ for a survey of 2M++'s size at the level of 5%. This issue can be addressed in future redshift surveys that delve deeper and cover larger volumes. The use of larger volumes offers two key benefits. Firstly, the local mean density within these volumes will exhibit reduced fluctuations in comparison to the global mean density. Secondly, the expanded survey area enables a more accurate calibration of the local value of $\sigma_{8,\mathrm{g}}$. Additionally when working with galaxy redshift surveys, it is necessary to correct for RSD. These are an observational effect in cosmology wherein the spatial distribution of galaxies appears to be compressed when comparing their positions in real space to those in redshift space. It is a consequence of the galaxies peculiar motions. Survey data generates galaxies with 2D coordinates, and a redshift value that measures its approximate distance from us via a radial velocity measurement. Velocities that are not along our line of sight cannot be measured. The work performed in this thesis is inherently based on knowing the true 3D position of objects. We note that this effect has been addressed in the previous work with 2M++ performed by Carrick et al. (2015). We did not account for this potential systematic biases this effect introduces into this thesis, but rather relied on previous tests conducted with N-body simulations to inform our analysis. Hence investigating how RSD impact our recovered measurements of our mock 2M++ and how to correct can provide valuable insights for studies who rely on these reconstructions to estimate cosmological parameters.

Furthermore, the estimators used to measure peculiar velocities of galaxies do not accurately capture the non-linear motion. In our work, any non-linear velocity gets fully absorbed into σ_8. In order to improve our understanding of peculiar velocities and reduce measurement errors, it may be necessary to develop new estimators that take into account more detailed non-linear information. These improved estimators will require fitting techniques that can handle non-Gaussian errors.

This involves accurately separating out the linear and non-linear contributions of the velocity field which can be done using methods, such as Second Order Lagrangian Perturbation Theory. Put simply, the velocity field can be constructed with a linear combinations of potentials, calculated from density fluctuations. The velocity predictions described in this thesis assumed that the divergence of the second order (non-linear) part of the gravitational potential was negligible. Consequently, the calculated velocities are a result solely of the divergence of the first order (linear) potential. To reduce the scatter generated in predictions, it is necessary to remove the error that is produced due to this oversimplification.

6.2 Future Surveys

Direct peculiar velocity measurements for tens of thousands of galaxies are already available through various surveys such as the 6-degree Field Galaxy Survey (Springob et al., 2014), the Sloan Digital Sky Survey (Saulder et al., 2023; Howlett et al., 2022), and the Cosmicflow catalogues (Tully et al., 2013, 2016, 2023). The availability of peculiar velocity samples has drastically increased in recent years. Notably, *Cosmicflows-IV* now encompasses more than 55,000 distances. While the SDSS Peculiar Velocity Catalogue contains approximately 34,000 distances (Howlett et al., 2022).

Furthermore, upcoming surveys conducted with advanced instruments such as DESI (DESI Collaboration et al., 2016) and 4MOST (de Jong et al., 2019), are expected to possess even greater capabilities. These surveys are anticipated to provide peculiar velocity measurements for over one million galaxies in total. Another notable survey is the "Wide-field ASKAP L-band Legacy All-sky Blind Survey" (WALLABY; Koribalski et al. (2020)), which focuses on HI (cold atomic Hydrogen) observations and will cover three-fourths of the sky. By using TF relations, this survey expects to obtain distance measurements for around 40,000 galaxies according to Howlett et al. (2017b). For comparison purposes, currently available TF catalogues like SFI++ contain approximately 4,500 galaxies.

With such a wealth of velocity data available, it will become possible to measure the growth rate (f) with an accuracy of around two percent - comparable to measurements of expansion - as demonstrated by studies such as Koda et al. (2014) and Howlett et al. (2017b). They have projected that combining data with the WALLABY peculiar velocity studies could lead to constraints on $f\sigma_8$ at the level of about 3%.

Furthermore, the number of low-redshift Type Ia supernovae suitable for peculiar velocity investigations is also expected to increase significantly. The use of SNe Ia for growth-rate measurements has been limited thus far. This is primarily due to the fact that most surveys have only cover small regions of the sky or are compilations from multiple telescopes, resulting in an uneven coverage across the sky (e.g, Betoule et al., 2014; Scolnic et al., 2022). However, photometric surveys with extensive sky coverage and high cadence, such as the Zwicky Transient Facility (ZTF; Graham et al. (2019)) and the Rubin Observatory Legacy Survey of Space and Time (Rubin-LSST; LSST Science Collaboration et al. (2009)), offer promising prospects.

Recently, the ZTF has started data collection, discovering ~ 3000 SNe Ia in the first 2.5 years of operation (Dhawan et al., 2022). The current spectroscopically classified SNe from DR1 have an average $z \sim 0.057$. This project is expected to observe 4,500 SNe with measurable distances within the first 5 years of operation and is expected to greatly enhance our knowledge of SNe properties in the local Universe (Dhawan et al., 2022). Additionally, in the near future, the LSST (Ivezić et al., 2019) will commence its data collection. It will obtain photometric redshifts of SNe Ia and measure their light curves in multiple bands. Allowing for cosmological distance measurements to the events. Forecasts have estimated that the LSST with 5 years of observations will be able to measure σ_8 with an uncertainty of 0.17 (Garcia et al., 2020). However, other estimates using methodology closer to what was used in this thesis predict uncertainties in $f\sigma_8$ on the order of 2-3% Howlett et al. (2017c), the caveat being that this method requires spectroscopic follow up of the SNe hosts to obtain their redshifts.

These upcoming surveys will provide a large and uniform sample of SNe Ia suitable for peculiar velocity studies (Howlett et al., 2017b). With comprehensive data collection capabilities over vast areas of the sky, these surveys hold great potential for advancing our understanding through more robust growth-rate measurements using SNe Ia observations. For instance the Pantheon+ collection, which was used in this thesis, currently contains a sample of $\sim$ 600 nearby SNe Ia, while the complete Foundation supernova sample is anticipated to include upwards of 800 supernovae at redshifts below $z = 0.1$ as indicated by Foley et al. (2018) and Jones et al. (2019).

Collectively, these peculiar velocity surveys hold the potential to provide us with unprecedented insights into the growth rate within our local Universe.

References

Aaronson M., Huchra J., Mould J., 1979, ApJ, 229, 1

Abazajian K., 2009, ApJS, 182, 543

Abbott B. P., et al., 2021, ApJ, 909, 218

Abbott T., et al., 2022, PRD, 105, 023520

Abdalla E., et al., 2022, JHEAP, 34, 49

Adams C., Blake C., 2017, MNRAS, 471, 839

Adams C., Blake C., 2020, MNRAS, 494, 3275

Alam S., et al., 2021, PRD, 103, 083533

Albrecht A., Steinhardt P. J., 1982, Phys. Rev. Lett., 48, 1220

Alpher R. A., Bethe H., Gamow G., 1948, Physical Review, 73, 803

Amanullah R., et al., 2010, ApJ, 716, 712

Asgari M., et al., 2020, A&A, 634, A127

Asgari M., et al., 2021, A&A, 645, A104

Baker T., Ferreira P. G., Leonard C. D., Motta M., 2014, PRD, 90, 124030

Basilakos S., Plionis M., 2001, ApJ, 550, 522

Beenakker W., Venhoek D., 2021, arXiv e-prints, p. arXiv:2101.01372

Behroozi P. S., Conroy C., Wechsler R. H., 2010, ApJ, 717, 379

Behroozi P. S., Wechsler R. H., Wu H.-Y., 2012, ApJ, 762, 109

Behroozi P. S., Wechsler R. H., Wu H.-Y., Busha M. T., Klypin A. A., Primack J. R., 2013, ApJ, 763, 18

Berlind A. A., Narayanan V. K., Weinberg D. H., 2000, ApJ, 537, 537

Bertschinger E., Dekel A., 1989, ApJ, 336, L5

Betoule M., et al., 2014, A&A, 568, A22

Bistolas V., Hoffman Y., 1998, ApJ, 492, 439

Boruah S. S., Hudson M. J., Lavaux G., 2020, MNRAS, 498, 2703

Boruah S. S., Hudson M. J., Lavaux G., 2021, MNRAS, 507, 2697

Bosma A., 1978, PhD Thesis, University of Groningen, Netherlands

Branchini E., et al., 1999, MNRAS, 308, 1

Branchini E., et al., 2001, MNRAS, 326, 1191

Brout D., et al., 2019, ApJ, 874, 150

Brout D., et al., 2022, ApJ, 938, 110

Brown P. J., et al., 2010, ApJ, 721, 1608

Busswell G. S., Shanks T., Frith W. J., Outram P. J., Metcalfe N., Fong R., 2004, MNRAS, 354, 991

Böhringer H., Chon G., Bristow M., Collins C. A., 2015, A&A, 574, A26

Böhringer H., Chon G., Collins C. A., 2020, A&A, 633, A19

Camarena D., Marra V., 2018, Phys. Rev. D, 98, 023537

Carr A., Davis T. M., Scolnic D., Said K., Brout D., Peterson E. R., Kessler R., 2022, Publ. Astron. Soc. Australia, 39, e046

Carrick J., Turnbull S. J., Lavaux G., Hudson M. J., 2015, MNRAS, 450, 317

Carroll S. M., Press W. H., Turner E. L., 1992, ARA&A, 30, 499

Chapman M. J., Zhai Z., Percival W. J., 2023, MNRAS, 525, 2135

Conley A., et al., 2011, ApJS, 192, 1

Cora S. A., et al., 2018, MNRAS, 479, 2

Courteau S., Dutton A. A., van den Bosch F. C., MacArthur L. A., Dekel A., McIntosh D. H., Dale D. A., 2007, ApJ, 671, 203

Courtois H. M., Hoffman Y., Tully R. B., Gottlöber S., 2012, ApJ, 744, 43

Croton D. J., et al., 2016, ApJS, 222, 22

DES Collaboration et al., 2023, arXiv e-prints, p. arXiv:2305.17173

DESI Collaboration et al., 2016, arXiv e-prints, p. arXiv:1611.00036

D'Onofrio M., Chiosi C., 2022, A&A, 661, A150

Davis M., Huchra J., 1982, ApJ, 254, 437

Davis M., Nusser A., Willick J. A., 1996, ApJ, 473, 22

Davis M., Nusser A., Masters K. L., Springob C., Huchra J. P., Lemson G., 2011, MNRAS, 413, 2906

Dawson K. S., et al., 2016, AJ, 151, 44

Dekel A., 1994, ARA&A, 32, 371

Dhawan S., et al., 2022, MNRAS, 510, 2228

Di Valentino E., et al., 2021, Astroparticle Physics, 131, 102604

Djorgovski S., Davis M., 1987, ApJ, 313, 59

Dressler A., Faber S. M., 1990, ApJ, 354, L45

Dressler A., Lynden-Bell D., Burstein D., Davies R. L., Faber S. M., Terlevich R., Wegner G., 1987, ApJ, 313, 42

Dupuy A., Courtois H. M., Kubik B., 2019, MNRAS, 486, 440

Eddington A. S., 1914, Stellar movements and the structure of the universe

Einstein A., 1916, Annalen der Physik, 354, 769

Einstein A., 1918, Annalen der Physik, 360, 241

Erdogdu P., et al., 2006, MNRAS, 373, 45

Faber S. M., Jackson R. E., 1976, ApJ, 204, 668

Feast M. W., Catchpole R. M., 1997, MNRAS, 286, L1

Feng J. L., 2010, ARA&A, 48, 495

Fisher J. R., Tully R. B., 1977, Comments on Astrophysics, 7, 85

Fisher K. B., Lahav O., Hoffman Y., Lynden-Bell D., Zaroubi S., 1995, MNRAS, 272, 885

Foley R. J., et al., 2018, MNRAS, 475, 193

Freedman W. L., 2021, ApJ, 919, 16

Freeman K. C., 1999, in Davies J. I., Impey C., Phillipps S., eds, Astronomical Society of the Pacific Conference Series Vol. 170, The Low Surface Brightness Universe. p. 3

Freudling W., da Costa L. N., Wegner G., Giovanelli R., Haynes M. P., Salzer J. J., 1995, AJ, 110, 920

Freudling W., et al., 1999, ApJ, 523, 1

Friedmann A., 1922, Zeitschrift fur Physik, 10, 377

Friedmann A., 1924, Zeitschrift fur Physik, 21, 326

Frieman J. A., 1996, Comments on Astrophysics, 18, 323

Frith W. J., Busswell G. S., Fong R., Metcalfe N., Shanks T., 2003, MNRAS, 345, 1049

Frith W. J., Metcalfe N., Shanks T., 2006, MNRAS, 371, 1601

Gaia Collaboration et al., 2023, A&A, 674, A1

Garcia K., Quartin M., Siffert B. B., 2020, Phys. Dark Universe, 29, 100519

Gil-Marín H., Percival W. J., Verde L., Brownstein J. R., Chuang C.-H., Kitaura F.-S., Rodríguez-Torres S. A., Olmstead M. D., 2016, MNRAS, 465, 1757

Gorski K. M., Davis M., Strauss M. A., White S. D. M., Yahil A., 1989, ApJ, 344, 1

Graham M. J., et al., 2019, PASP, 131, 078001

Graziani R., Courtois H. M., Lavaux G., Hoffman Y., Tully R. B., Copin Y., Pomarède D., 2019, MNRAS, 488, 5438

Guth A. H., 1981, Phys. Rev. D, 23, 347

Hamilton A. J. S., 2001, MNRAS, 322, 419

Haslbauer M., Banik I., Kroupa P., 2020, MNRAS, 499, 2845

Heymans C., et al., 2013, MNRAS, 432, 2433

Heymans C., et al., 2021, A&A, 646, A140

Hicken M., Wood-Vasey W. M., Blondin S., Challis P., Jha S., Kelly P. L., Rest A., Kirshner R. P., 2009, ApJ, 700, 1097

Hollinger A. M., Hudson M. J., 2021, MNRAS, 502, 3723

Hong T., et al., 2019, MNRAS, 487, 2061

Hoscheit B. L., Barger A. J., 2018, ApJ, 854, 46

Howlett C., 2019, MNRAS, 487, 5209

Howlett C., Staveley-Smith L., Blake C., 2017a, MNRAS, 464, 2517

Howlett C., et al., 2017b, MNRAS, 471, 3135

Howlett C., Robotham A. S. G., Lagos C. D. P., Kim A. G., 2017c, ApJ, 847, 128

Howlett C., Said K., Lucey J. R., Colless M., Qin F., Lai Y., Tully R. B., Davis T. M., 2022, MNRAS, 515, 953

Hu Y., Li M., Li N., Wang S., 2016, A&A, 592, A101

Hubble E., 1929, PNAS, 15, 168

Huchra J. P., Geller M. J., 1982, ApJ, 257, 423

Huchra J. P., et al., 2012, ApJS, 199, 26

Hudson M. J., 1994, MNRAS, 266, 475

Hudson M. J., Turnbull S. J., 2012, ApJL, 751, L30

Hudson M. J., Lucey J. R., Smith R. J., Schlegel D. J., Davies R. L., 2001, MNRAS, 327, 265

Huterer D., Shafer D. L., Scolnic D. M., Schmidt F., 2017, JCAP, 2017, 015

Ivezić , et al., 2019, ApJ, 873, 111

Jasche J., Lavaux G., 2019, A&A, 625, A64

Jasche J., Wandelt B. D., 2013, MNRAS, 432, 894

Jasche J., Kitaura F. S., Li C., Enßlin T. A., 2010, MNRAS, 409, 355

Johnson A., et al., 2014, MNRAS, 444, 3926

Johnson A., Blake C., Dossett J., Koda J., Parkinson D., Joudaki S., 2016, MNRAS, 458, 2725

Jones D. H., et al., 2009, MNRAS, 399, 683

Jones D. O., et al., 2019, ApJ, 881, 19

Juszkiewicz R., Feldman H. A., Fry J., Jaffe A. H., 2010, JCAP, 2010, 021

Kaiser N., 1984, ApJ, 284, L9

Kaiser N., 1987, MNRAS, 227, 1

Kaiser N., Efstathiou G., Saunders W., Ellis R., Frenk C., Lawrence A., Rowan-Robinson M., 1991, MNRAS, 252, 1

Keenan R. C., Barger A. J., Cowie L. L., 2013, ApJ, 775, 62

Kelly P. L., Hicken M., Burke D. L., Mandel K. S., Kirshner R. P., 2010, ApJ, 715, 743

Kenworthy W. D., Scolnic D., Riess A., 2019, ApJ, 875, 145

Kenworthy W. D., et al., 2022, ApJ, 935, 83

Kessler R., et al., 2009, ApJS, 185, 32

Kitaura F. S., 2013, MNRAS, 429, L84

Kitaura F.-S., Jasche J., Metcalf R. B., 2010, MNRAS, 403, 589

Kitaura F.-S., Ata M., Rodríguez-Torres S. A., Hernández-Sánchez M., Balaguera-Antolínez A., Yepes G., 2021, MNRAS, 502, 3456

Klypin A. A., Trujillo-Gomez S., Primack J., 2011, ApJ, 740, 102

Klypin A., Yepes G., Gottlöber S., Prada F., Heß S., 2016, MNRAS, 457, 4340

Knebe A., et al., 2018, MNRAS, 474, 5206

Knox L., Millea M., 2020, Phys. Rev. D, 101, 043533

Koda J., et al., 2014, MNRAS, 445, 4267

Koribalski B. S., et al., 2020, Ap&SS, 365, 118

Kourkchi E., Tully R. B., Courtois H. M., Dupuy A., Guinet D., 2022, MNRAS, 511, 6160

Kowalski M., et al., 2008, ApJ, 686, 749

Kravtsov A. V., Klypin A. A., Khokhlov A. M., 1997, ApJS, 111, 73

Kravtsov A. V., Berlind A. A., Wechsler R. H., Klypin A. A., Gottlöber S., Allgood B., Primack J. R., 2004, ApJ, 609, 35

LSST Science Collaboration et al., 2009, arXiv e-prints, p. arXiv:0912.0201

Lahav O., Lilje P. B., Primack J. R., Rees M. J., 1991, MNRAS, 251, 128

Lampeitl H., et al., 2010, ApJ, 722, 566

Lavaux G., 2016, MNRAS, 457, 172

Lavaux G., Hudson M. J., 2011, MNRAS, 416, 2840

Leavitt H. S., 1908, Annals of Harvard College Observatory, 60, 87

Leavitt H. S., Pickering E. C., 1912, Harvard College Observatory Circular, 173, 1

Lemaître G., 1931, Nature, 127, 706

Li M., Li N., Wang S., Zhou L., 2016, MNRAS, 460, 2586

Li S.-S., et al., 2023, KiDS-1000: Cosmology with improved cosmic shear measurements, `http://arxiv.org/abs/2306.11124`

Lightman A. P., Schechter P. L., 1990, ApJS, 74, 831

Lilow R., Nusser A., 2021, MNRAS, 507, 1557

Linde A. D., 1982, Physics Letters B, 108, 389

Linder E. V., 2005, PRD, 72, 043529

Lynden-Bell D., Faber S. M., Burstein D., Davies R. L., Dressler A., Terlevich R. J., Wegner G., 1988, ApJ, 326, 19

Lynden-Bell D., Lahav O., Burstein D., 1989, MNRAS, 241, 325

Ma Y.-Z., Branchini E., Scott D., 2012, MNRAS, 425, 2880

Maddox S. J., Sutherland W. J., Efstathiou G., Loveday J., Peterson B. A., 1990, MNRAS, 247, 1P

Malmquist K. G., 1920, Meddelanden fran Lunds Astronomiska Observatorium Serie I, 96, 1

Malmquist K. G., 1924, Meddelanden fran Lunds Astronomiska Observatorium Serie II, 32, 3

Marinoni C., Hudson M. J., 2002, ApJ, 569, 101

Masters K. L., Springob C. M., Haynes M. P., Giovanelli R., 2006, ApJ, 653, 861

Masters K. L., Springob C. M., Huchra J. P., 2008, AJ, 135, 1738

McGaugh S. S., 2012, AJ, 143, 40

McGaugh S. S., Schombert J. M., Bothun G. D., de Blok W. J. G., 2000, ApJ, 533, L99

Mo H., van den Bosch F. C., White S., 2010, Galaxy Formation and Evolution

Mohlabeng G. M., Ralston J. P., 2014, MNRAS, 439, L16

Moster B. P., Somerville R. S., Maulbetsch C., Bosch F. C. v. d., Macciò A. V., Naab T., Oser L., 2010, ApJ, 710, 903

Mould J., 2020, Front. Astron. Space Sci., 7, 21

Mörtsell E., Goobar A., Johansson J., Dhawan S., 2022, ApJ, 933, 212

Neill J. D., Hudson M. J., Conley A., 2007, ApJ, 661, L123

Newton I., 1687, Philosophiae Naturalis Principia Mathematica., doi:10.3931/e-rara-440.

Nusser A., 2017, MNRAS, 470, 445

Nusser A., Davis M., 1994, ApJ, 421, L1

Nusser A., Davis M., Branchini E., 2014, ApJ, 788, 157

Nusser A., Yepes G., Branchini E., 2020, ApJ, 905, 47

Odderskov I., Hannestad S., Brandbyge J., 2017, JCAP, 2017, 022

Park C., 2000, MNRAS, 319, 573

Park C.-G., Park C., 2006, ApJ, 637, 1

Peebles P. J. E., 1980, The large-scale structure of the universe

Peebles P. J. E., 1984, ApJ, 284, 439

Peebles P. J. E., 1993, Principles of physical cosmology. Princeton University Press

Penzias A. A., Wilson R. W., 1965, ApJ, 142, 419

Perlmutter S., et al., 1997, ApJ, 483, 565

Perlmutter S., et al., 1998, Nature, 391, 51

Peterson E. R., et al., 2022, ApJ, 938, 112

Pike R., Hudson M. J., 2005, ApJ, 635, 11

Planck Collaboration et al., 2020a, A&A, 641, A1

Planck Collaboration et al., 2020b, A&A, 641, A6

Pogosian L., Zhao G.-B., Jedamzik K., 2020, ApJL, 904, L17

Qin F., Howlett C., Staveley-Smith L., 2019, MNRAS, 487, 5235

Qin F., Parkinson D., Hong S. E., Sabiu C. G., 2023, JCAP, 2023, 062

Riess A. G., et al., 1998, AJ, 116, 1009

Riess A. G., et al., 2016, ApJ, 826, 56

Riess A. G., et al., 2018, ApJ, 855, 136

Riess A. G., et al., 2022, ApJ, 934, L7

Ripepi V., et al., 2020, A&A, 642, A230

Rubin V. C., 1983, Science, 220, 1339

Rubin V. C., Ford W. Kent J., 1970, ApJ, 159, 379

Rubin V. C., Ford W. K. J., Thonnard N., 1978, ApJL, 225, L107

Rubin V. C., Ford W. K. J., Thonnard N., 1980, ApJ, 238, 471

Rubin V. C., Burstein D., Ford W. K. J., Thonnard N., 1985, ApJ, 289, 81

Said K., Colless M., Magoulas C., Lucey J. R., Hudson M. J., 2020, MNRAS, 497, 1275

Sandage A., Tammann G. A., 1975, ApJ, 196, 313

Saulder C., et al., 2023, Target Selection for the DESI Peculiar Velocity Survey, `http://arxiv.org/abs/2302.13760`

Schechter P., 1976, ApJ, 203, 297

Scolnic D., et al., 2014, ApJ, 795, 45

Scolnic D. M., et al., 2018, ApJ, 859, 101

Scolnic D., et al., 2022, ApJ, 938, 113

Scolnic D., et al., 2023, ApJL, 954, L31

Scott D., 2006, Can. J. Phys., 84, 419

Secco L. F., et al., 2022, Phys. Rev. D, 105, 023515

Slipher V. M., 1915, Popular Astronomy, 23, 21

Smith R. E., et al., 2003, MNRAS, 341, 1311

Springob C. M., Masters K. L., Haynes M. P., Giovanelli R., Marinoni C., 2007, ApJS, 172, 599

Springob C. M., et al., 2014, MNRAS, 445, 2677

Strauss M. A., Willick J. A., 1995, Phys. Rep., 261, 271

Sullivan M., et al., 2010, MNRAS, 406, 782

Suzuki N., et al., 2012, ApJ, 746, 85

Takahashi R., Sato M., Nishimichi T., Taruya A., Oguri M., 2012, ApJ, 761, 152

Tasitsiomi A., Kravtsov A. V., Wechsler R. H., Primack J. R., 2004, ApJ, 614, 533

Tonry J. L., et al., 2012, ApJ, 750, 99

Tully R. B., Pierce M. J., 2000, ApJ, 533, 744

Tully R. B., Pierce M. J., Huang J.-S., Saunders W., Verheijen M. A. W., Witchalls P. L., 1998, AJ, 115, 2264

Tully R. B., et al., 2013, AJ, 146, 86

Tully R. B., Courtois H. M., Sorce J. G., 2016, AJ, 152, 50

Tully R. B., et al., 2023, ApJ, 944, 94

Turnbull S. J., Hudson M. J., Feldman H. A., Hicken M., Kirshner R. P., Watkins R., 2012, MNRAS, 420, 447

Turner E. L., Cen R., Ostriker J. P., 1992, AJ, 103, 1427

Turner R. J., Blake C., Ruggeri R., 2021, MNRAS, 502, 2087

Turner R. J., Blake C., Ruggeri R., 2023, MNRAS, 518, 2436

Wang Y., 1999, ApJ, 525, 651

Wang L., Steinhardt P. J., 1998, ApJ, 508, 483

Wang S., Wang Y., 2013, Phys. Rev. D, 88, 043511

Wang L., Goldhaber G., Aldering G., Perlmutter S., 2003, ApJ, 590, 944

Wang H., Mo H. J., Yang X., van den Bosch F. C., 2013, ApJ, 772, 63

Wang S., Wang Y.-Z., Zhang X., 2014a, Commun. Theor. Phys., 62, 927

Wang S., Wang Y.-Z., Geng J.-J., Zhang X., 2014b, European Physical Journal C, 74, 3148

Wang S., Li Y.-H., Zhang X., 2014c, Phys. Rev. D, 89, 063524

Weinberg S., 1989, Reviews of Modern Physics, 61, 1

Weinberg D. H., Mortonson M. J., Eisenstein D. J., Hirata C., Riess A. G., Rozo E., 2013, Phys. Rep., 530, 87

Westover M., 2007, PhD thesis, `https://ui.adsabs.harvard.edu/abs/2007PhDT.........3W`

Whitbourn J. R., Shanks T., 2014, MNRAS, 437, 2146

Willick J. A., Batra P., 2001, ApJ, 548, 564

Willick J. A., Courteau S., Faber S., Burstein D., Dekel A., Strauss M. A., 1997, ApJS, 109, 333

Wong J. H. W., Shanks T., Metcalfe N., Whitbourn J. R., 2022, MNRAS, 511, 5742

Wu H.-Y., Huterer D., 2017, MNRAS, 471, 4946

Yahil A., Strauss M. A., Davis M., Huchra J. P., 1991, ApJ, 372, 380

Yoo J., Watanabe Y., 2012, Int. J. Mod. Phys. D, 21, 1230002

York D. G., et al., 2000, AJ, 120, 1579

Yuan S., Garrison L. H., Eisenstein D. J., Wechsler R. H., 2022, MNRAS, 515, 871

Zaroubi S., Hoffman Y., Dekel A., 1999, ApJ, 520, 413

Zheng Y., Zhang P., Jing Y., Lin W., Pan J., 2013, PRD, 88

Zhu H.-M., White M., Ferraro S., Schaan E., 2020, MNRAS, 494, 4244

Zucca E., et al., 1997, A&A, 326, 477

Zwicky F., 1933, Helvetica Physica Acta, 6, 110

da Costa L. N., Freudling W., Wegner G., Giovanelli R., Haynes M. P., Salzer J. J., 1996, ApJ, 468, L5

de Jong R. S., et al., 2019, The Messenger, 175, 3

de Vaucouleurs G., Bollinger G., 1979, ApJ, 233, 433